Systems of Charged Grains in Plasmas

（プラズマ中の荷電微小粒子系）

浜口智志

Systems of Charged Grains in Plasmas

Satoshi Hamaguchi

Abstract

Dynamical and thermodynamical properties of systems of charged grains ("dust" particles) immersed in plasmas are discussed. In a uniform plasma with nonuniform background neutral gases, the transport of each charged grain is determined by the collisional forces (e.g., drag forces), electrostatic forces and gravitational forces. In a nonuniform plasma, polarized Debye sheaths exert an addition force (polarization force) on charged grains. This sheath-polarization force is derived in the presence of an external electric field, plasma density gradients, and finite plasma flows. It is shown that the polarization force is always in the direction of decreasing Debye length, regardless of the sign of the particulate charge. The magnitude of the polarization force is also estimated under typical glow discharge conditions. If the interparticle potential energy sufficiently exceeds the thermal energy, the system of charged particles can form Coulomb crystals. The thermodynamical properties of such strongly-coupled systems are also studied, using molecular-dynamics (MD) simulations. If the background plasma is in thermal equilibrium, the interparticle potential is given by the screened Coulomb potential (Yukawa potential). Such systems (Yukawa systems) becomes the well-known one-component plasma (OCP) in the limit of infinite Debye length. The phase diagram of Yukawa systems is obtained that covers from the OCP limit to the strongly-screened regime.

Acknowledgments

It is a pleasure to record my gratitude to many people who have helped me to write this thesis. In particular, to Professor Hiroshi Toyama, I owe my introduction to plasma physics, many valuable comments and suggestions on the subject treated in this thesis and many acts of kind encouragement; to Professor Kenro Miyamoto, my initiation into experimental research of plasma physics and continuous encouragement. I am also grateful to Professor Taijiro Uchida and Professor Nobuyuki Inoue for having guided me in my experimental work while I was a graduate student at the Department of Physics of the University of Tokyo.

I would also like to offer my special thanks to my former colleague Professor R. T. Farouki for many valuable comments and helpful discussions on dusty plasmas and molecular dynamics simulation. I also acknowledge useful discussions on strongly-coupled systems with Professor E. E. Salpeter, Dr. H. E. DeWitt, and Dr. Y. Rosenfeld. I also thank Dr. G. S. Selwyn for kindly providing the picture of a dusty plasma (Fig. 1.1) and Professor D. H. E. Dubin for sharing the lattice-dynamics-calculation data of the harmonic entropy constants (Table 5.2) before its publication.

Contents

Chapter 1

Introduction

1.1. Dust particles in plasmas

Small charged dust grains or "particulates" are observed in a wide variety of plasma environments, ranging from the interstellar medium to low-pressure discharges used in industrial applications. Such particles are typically "mesoscopic" — small on the macroscopic scale but significantly larger than molecular sizes.

The presence of dust particles in the interstellar medium, which appear as "dark nebulae" in space, puzzled many astronomers from the late 18th century to early 20th century. It was not known then whether such dark patches were opaque clouds in from of bright stars or just the absence of bright stars.[1] Dust particles are indeed rather ubiquitous in space, from interplanetary to intergalactic media. Some of such particles are immersed in cold molecular gases and others in "hot" plasmas. Dust particles in plasmas often carry large electric charges and the background plasma serves as a charge neutralizing medium, ensuring the overall charge neutrality of the system.

In the solar system, dust particles are commonly observed in the tails of comets and also form rings in the magnetosphere of some planets.[2,3] In interstellar plasmas, heated dust grains emit a large infrared continuum at wavelengths in the range of 3–3000μm. Together with the radio continuum (3mm–1m) emission due to bremsstrahlung from the plasma ions,

these continua are often the only information about HII regions (i.e., parts of space occupied by hydrogen plasmas) in many cases since many of HII regions are not visible at optical wavelengths.[4]

More recently dust particles in terrestrial plasmas have started to attract significant attention of engineers and scientists. As plasmas have been increasingly used in industrial materials processing, charged dust grains in process plasmas have been recognized as a major source of contamination..[5–10] For example, the presence of such particulates poses serious problems for product yield and reliability in semiconductor chip manufacturing. Since the in-situ control of generation and transport of dust particles in processing systems is difficult, various cleaning techniques have been employed to reduce such contaminants from the wafer surfaces after the processes.[11]

The study of plasma–dust systems is thus motivated by a desire to understand the fundamental mechanisms that governs those systems under such diverse conditions. As a matter of theoretical interest, we also note some of the theories relevant to plasma–dust systems are also applicable to other systems such as colloidal suspensions[12,13] and charged aerosols.[14] Similarly to dust grains in plasmas, colloidal particles in electrolyte solutions are electrically charged due to the ion attachment. Colloidal solutions and aerosols have also been extensively studied on account of its wide-ranging technological uses.

Small grains in neutral gas environments are subject to drag and thermophoretic forces, as is well known in the study of aerosol particles. Immersed in plasmas, small grains typically acquire negative charges due to the high mobility of electrons, as we shall discuss in Sec. 1.3. Interactions of charged particles with the ambient plasmas and neutral gases determine the particle transport. For instance, in a weakly ionized plasma used for typical semiconductor etch and deposition processes, dust grains are transported by ion and neutral drag forces toward the plasma edge region and trapped there by strong electric fields. (See Fig. 1.1.)

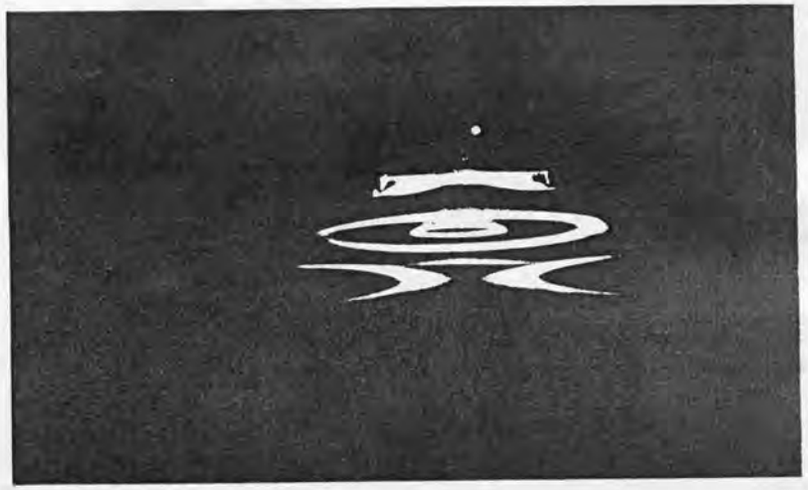

Figure 1.1: Dust clouds in a parallel plate discharge plasma. Three wafers are placed in the chamber although they are invisible in this picture. White rings are dust clouds above the wafers. Inside each white ring a dome-shaped cloud is formed right above the wafer center. The dust clouds are illuminated by the laser beam scattering. The small white dot on the upper side of the picture is the laser source and a roughly rectangular white patch is the observation window illuminated by the scattered laser light. (Courtesy of G. S. Selwyn).

Also of importance are particle–particle interactions in plasmas. If the particulate number density is sufficiently high, the interparticle potential energies may substantially exceed their thermal kinetic energies,[15] and the particulate system then exhibits behavior similar to a liquid[16] or the classical one-component plasma.[17–21] Especially if the particle kinetic energy is sufficiently reduced, it is known that the particles form crystal structures (i.e., Coulomb crystals).[15,16,22–26]

In this chapter, we summarize some known results on the charging mechanism and exerted forces for small grains immersed in plasmas. The knowledge of such forces serves the starting point from which we construct a more detailed theory for particle–plasma interactions in the presence of steep density gradients. The remaining chapters are organized as follows. In Chap. 2, we employ a fluid description for the plasma to derive the force exerted on a particle due to a deformed Debye sheath around it. The deformation (i.e., polarization) of the sheath may be caused by a large density gradient of the plasma, which often exists near the plasma edge region. The contribution of the polarization to the transport of an isolated gain is also discussed. In the presence of strong ion currents, the sheath polarization by the plasma density gradient is further affected, which is discussed in detail in Chap. 3. In Chaps. 4 and 5, we focus on the interparticle interaction among grains. First the interparticle potential will be derived in Chap. 4 based on the free-energy calculations. The obtained interparticle potential is then used in the molecular dynamic simulations and the phase diagram of charged grain systems will be obtained in Chap. 5. Chapter 6 contains the summary of the entire work.

1.2. Debye shielding

Let us consider a uniform unmagnetized plasma, in which the ion and electron densities are given by n_{i0} and n_{e0} and the plasma potential is given by Ψ_0. (Since Ψ_0 is assumed to spatially dependent in Chap. 2, we treat Ψ_0 is as a non-zero constant in this Chapter.)

The charge neutrality condition in the absence of charged grains requires $qn_{i0} = en_{e0}$, where the ion and electron charges are denoted by q and $-e$ (we assume ions of single species; the extension to multiple species is straightforward).

We now place a small particulate with radius a at position $\mathbf{r} = \mathbf{0}$ in the plasma. As we shall discuss in the next section, it will acquire a negative charge, $-Q$, due to attachment of high-mobility plasma electrons. The charged particulate perturbs the local electric field and plasma density, forming a Debye sheath around it. The resultant electric field potential $\Psi(\mathbf{r})$ satisfies Poisson's equation:

$$\Delta\Psi(\mathbf{r}) = -\frac{\rho(\mathbf{r})}{\varepsilon_0}, \tag{1.1}$$

where $\rho(\mathbf{r})$ denotes the total charge density given by

$$\rho(\mathbf{r}) = -Q\delta(\mathbf{r}) + qn_i(\mathbf{r}) - en_e(\mathbf{r}),$$

and $n_i(\mathbf{r})$ and $n_e(\mathbf{r})$ are ion and electron densities after the perturbation. Evidently these densities $n_i(\mathbf{r})$ and $n_e(\mathbf{r})$ approach their original values n_{i0} and n_{e0} sufficiently away from the particulate position, i.e., $|\mathbf{r}| \to \infty$.

The boundary conditions for Eq. (1.1) is given by

$$\Psi(\mathbf{r}) \to \Psi_0 \quad \text{as} \quad r \to \infty \tag{1.2}$$

$$\Psi(\mathbf{r}) = \Psi_0 + V_s \quad \text{at} \quad r = a. \tag{1.3}$$

In Eq. (1.3), V_s denotes the surface potential of the particulate, which we assume be constant for simplicity as is the case for a metal particulate. The surface potential V_s is a function of the total charge $-Q$ residing on the surface, given by

$$Q = \varepsilon_0 \oint_{r=a} \frac{\partial\Psi}{\partial r}\, dS \tag{1.4}$$

the integration being over the particulate surface (note that the quantity $-\varepsilon_0 \partial\Psi/\partial r|_{r=a}$ represents the surface charge density).

The dependence of the ion and electron densities on the electrostatic field is determined by the microscopic plasma characteristics. If collisions are sufficiently frequent, it may be assumed that the plasma is in thermal equilibrium and the local ion and electron densities are given by the Boltzmann distributions[27]:

$$n_i(\mathbf{r}) = n_{i0} \exp\left[-\frac{q\varphi(\mathbf{r})}{k_B T_i}\right], \tag{1.5}$$

$$n_e(\mathbf{r}) = n_{e0} \exp\left[\frac{e\varphi(\mathbf{r})}{k_B T_e}\right], \tag{1.6}$$

where

$$\varphi(\mathbf{r}) = \Psi(\mathbf{r}) - \Psi_0$$

is the perturbation in the potential, and T_i and T_e are the ion and electron temperatures.

If the potential perturbation is sufficiently small (i.e., $|\varphi| \ll k_B T_i, k_B T_e$), the ion and electron densities given in Eqs. (1.5) and (1.6) may be linearized with respect to φ (the so-called Debye-Hückel approximation). Substituting the resulting expressions for $n_i(\mathbf{r})$ and $n_e(\mathbf{r})$ into Eq. (1.1), we obtain

$$\Delta\varphi(\mathbf{r}) = \frac{Q}{\varepsilon_0}\delta(\mathbf{r}) + k_D^2\varphi(\mathbf{r}), \tag{1.7}$$

with

$$k_D^2 = \frac{q^2 n_{i0}}{\varepsilon_0 k_B T_i} + \frac{e^2 n_{e0}}{\varepsilon_0 k_B T_e}. \tag{1.8}$$

The boundary condition for Eq. (1.7) is then given by

$$\varphi(\mathbf{r}) \to 0 \quad \text{as} \quad |\mathbf{r}| \to \infty.$$

From Eq. (1.8), the characteristic Debye length $\lambda_D(\mathbf{r})$, defined by $\lambda_D = k_D^{-1}$, is related to the ion and electron Debye lengths

$$\lambda_i = \left[\frac{\varepsilon_0 k_B T_i}{q^2 n_{i0}}\right]^{\frac{1}{2}} \quad \text{and} \quad \lambda_e = \left[\frac{\varepsilon_0 k_B T_e}{e^2 n_{e0}}\right]^{\frac{1}{2}}$$

through

$$\lambda_D = \left[\frac{1}{\lambda_i^2} + \frac{1}{\lambda_e^2}\right]^{-\frac{1}{2}} \tag{1.9}$$

Note, in particular, that $\lambda_D \simeq \lambda_i$ if $T_e \gg T_i$.

The solution to Eq. (1.7) is readily obtained as

$$\varphi(\mathbf{r}) = \frac{V_s a \exp[-k_D(r-a)]}{r}.$$

To relate the potential V_s to the particle charge $-Q$, we now substitute $\Psi = \Psi_0 + \varphi$ into Eq. (1.4) to obtain $V_s = -Q/4\pi\varepsilon_0(1 + k_D a)a$, or

$$\varphi(\mathbf{r}) = -\frac{Q \exp[-k_D(r-a)]}{4\pi\varepsilon_0(1 + k_D a)r}. \tag{1.10}$$

In the limit of small particle size $a \to 0$, Eq. (1.10) becomes the well-known screened Coulomb (Yukawa) potential

$$\varphi(\mathbf{r}) = -\frac{Q}{4\pi\varepsilon_0}\frac{\exp(-k_D r)}{r}, \tag{1.11}$$

where $r = |\mathbf{r}|$.

The assumption of the Boltzmann distribution for ions given in Eq. (1.5), and its linearization employed to derive Eq. (1.7) — i.e., the Debye–Hückel approximation — need further explanation. In typical laboratory or space plasmas, where the ion Debye length is significantly smaller than the ion mean free path, the ion Boltzmann distribution inside the sheath of a particulate is rather unrealistic. Also, for a particulate in a relatively cold plasma (e.g., $T_i < 1$eV), the electrostatic potential at the surface of the particulate is larger than the ion kinetic energy, i.e., $\varphi(a) \gtrsim k_B T_i$, which violates the condition for linearization. Therefore, rigorously speaking, the model we have adopted does not apply to systems of dust grains in laboratory plasmas.

However, a simple physical argument suggests that, despite the apparent invalidity of the model, the properties of the system that we are concerned with in this system are relatively

insensitive to the exact form of the ion distribution in the sheath. This insensitivity explain why the Debye–Hückel approximation has been successfully applied to various systems, ranging from colloidal particles[12,13] to dust in space plasmas,[27,28] in earlier studies.

The important physical aspect of a particulate sheath is that, toward the particulate surface, the ion density increases monotonically whereas the electron density decreases monotonically (for collisionless plasmas, see Ref. 29). This behavior is retained by the linearized ion distribution $n_i(\mathbf{r}) = n_{i0}[1 - q\varphi(\mathbf{r})/k_B T_i]$, noting that the asymptotic behavior of the potential, $\varphi \to -\infty$ monotonically as $|\mathbf{r}| \to 0$, is self-consistently derived from the linearized Boltzmann distributions. The thicknesses of the ion-excess layer (i.e., ion sheath) and electron-deficient layer (i.e., electron sheath) — which overlap each other — are typically given by the ion and electron Debye lengths. The exact value of the ion-sheath thickness, of course, depends on a specific model of the ion density distributions. See Appendix A for further discussion of this point.

Furthermore, when the mean (i.e., flow) ion velocity exceeds the thermal velocity $v_{th} = (k_B T_i/m_i)^{\frac{1}{2}}$, as is often the case in laboratory plasmas, the ion sheath may be either strongly distorted or unable to form at all around the particulate. In this case, the sheath is made up only of a deficiency of electrons and its thickness is given approximately by the *electron* Debye length, λ_e. Note that, in typical process plasmas, the plasma flow velocity may reach the ion sound velocity $c_s = (k_B T_e/m_i)^{\frac{1}{2}}$ but seldom exceeds the electron thermal velocity $v_{e,th} = (k_B T_e/m_e)^{\frac{1}{2}}$. Under such conditions, the ion density distribution is given neither by the Boltzmann distribution, Eq. (1.5), nor the collisionless distribution derived by Bernstein and Rabinowitz[29]: it is almost uniform in the sheath. Again, the exact form of the ion density distribution does not influence the qualitative form of the potential profile and the plasma pressure near the particulate. We shall discuss the effects of a finite ion flow further in Chap. 3.

Since the final results are likely insensitive to the exact functional form assumed for the

ion density distribution, the advantage of using the linearized Boltzmann form is obvious: the system is solvable analytically and thus yields clear insight into its physical behavior. The 0th order solution that we employ in the following is the spherically-symmetric solution to the Debye-Hückel approximation of Poisson's equation, which has been studied extensively and is well understood. Of course, studying the system numerically with more realistic ion density distributions is important and more simulation studies are needed. Our analytical model serves as a reference system and point of departure for the subsequent construction of models under more realistic conditions.

1.3. Grain charges in a plasma

In the previous section, we calculated the electric field around a particulate with an arbitrary charge $-Q$ in a plasma. In this section, we shall discuss the mechanism by which particulates gain such charges in a plasma.

In a typical plasma, electrons have higher thermal velocity than that of ions and therefore are more likely to be captured by the macroscopic material, such as a dust grain. Once the materials is sufficiently negatively charged due to the electron attachment, they it attracts positive ions and neutralizes excessive electrons on its surface. Eventually balance between the electron and ion fluxes creates an equilibrium state where the material surfaces have their own potentials lower than the plasma potential.

The ions and electrons currents driven by the sheath electric field determine the grain surface charge in typical low-temperature laboratory plasmas. Under different conditions, such as those of planetary magnetospheres or interstellar plasmas, however, currents caused by different mechanisms may play more important roles to determine the surface charge.

For example, if a dust particle is subject to high-energy electron bombardment, it may lose more electrons from its surface due to the secondary electron emission than it gains.[30]

The secondary electron coefficient (or yield) $\delta(E)$ — the number of electrons ejected per incident electron — depends on the incident energy and attains its maximum value δ_m at finite energy E_m. For most materials δ_m range from 0.5 to 30 at E_m between 0.1 and 2 keV.[31]

In a strong radiation field, photoemission — the ejection of electrons (i.e., photoelectrons) due to photon bombardment — can also reduces the number of electrons from grain surfaces and thus constitutes a positive charging current.[1] The photoelectron yield γ_p — the number of electrons ejected per incident photon — is negligible at visible wavelengths but generally increases in the far ultraviolet. For many materials, $\gamma_p \simeq 0.1$ near the wavelength $\lambda \simeq 1000\mathring{A}$.[32]

In space plasmas, therefore, it is not unusual that dust grains are positively charged due to electron-induced secondary electron emission and/or photoemission. Secondary electron emission can be also caused by ion bombardment, neutral bombardment[31] and strong surface electric fields (field emission)[2] although the yields due to these mechanisms are typically negligible in most cases even in the space plasma environments.

As we discussed earlier, the charge on each particle (dust grain) in low-temperature laboratory plasmas is essentially determined by the ion and electron currents due to the sheath field. Assuming the Maxwellian velocity distributions for ions and electrons with temperature T_i and T_e, the currents to the grain surface may be obtained by integration over the Maxwellian distributions in the usual way. For a spherical grain of radius a whose surface potential is more negative than the ambient plasma potential, the ion and electron currents to the grain surface are given[27,28] by

$$I_i = q n_{i0} \sqrt{\frac{k_B T_i}{m_i}} \left[1 - \frac{q\phi(a)}{k_B T_i} \right] \pi a^2 \tag{1.12}$$

and

$$I_e = -e n_{e0} \sqrt{\frac{k_B T_e}{m_e}} \exp\left[\frac{e\phi(a)}{k_B T_e} \right] \pi a^2 \tag{1.13}$$

The equilibrium condition $I_i + I_e = 0$ determines the surface potential $\phi(a)$ as a function of the background plasma parameters:

$$1 - q\beta_i\phi(a) = \frac{en_{e0}}{qn_{i0}}\sqrt{\frac{m_i\beta_i}{m_e\beta_e}}\exp[e\beta_e\phi(a)], \tag{1.14}$$

where $\beta_{i(e)} = 1/k_BT_{i(e)}$. For an isolated grain in a hydrogen plasma ($q = e$) with $n_{i0} = n_{e0}$ and $T_i = T_e = T$, one obtains the solution $\phi(a) = -2.5k_BT/e$, which is known as Spitzer result.[33] If the dust number density n_d is sufficiently high, then the surface potential $\phi(a)$ depends on n_d through the charge neutrality condition with charged dust grains

$$qn_{i0} - en_{e0} - Qn_d = 0. \tag{1.15}$$

The numerical solutions to Eqs. (1.14) and (1.15) obtained for $T_i = T_e = T$, together with experimental data,[34] are shown in Fig. 1.2. It is shown that, as the grain number density increases, electrons in the plasma are depleted and thus the grain surface potential becomes closer to the plasma potential.

If particles are sufficiently isolated (i.e., interparticle distances are much larger the Debye length λ_D) — as is assumed for Fig. 1.2 —, it follows from Eq. (1.10) that the surface potential $\phi(a)$ is proportional to the particle's charge $\mathcal{Q} = -Q$

$$\mathcal{Q} = -Q(\infty) = 4\pi\varepsilon_0 a(1 + k_D a)\phi(a). \tag{1.16}$$

(Here ∞ denotes the infinite particle separation.) However, if the interparticle distances are comparable with or smaller than the Debye length, the grain charge $\mathcal{Q}$ is also influenced by the presence of other charged particles in its vicinity. This effect is in addition to the global electron depletion effect shown in Fig. 1.2. The ith grain has charge $\mathcal{Q}_i = -Q_i$ and the distance between the ith and jth grains is denoted by R_{ij}. If the grain radius a is sufficiently smaller than the Debye length and interparticle distances, (i.e., $a \ll \lambda_D$, R_{ij}), then we obtain the relation

$$\frac{1}{4\pi\varepsilon_0}\left[\frac{\mathcal{Q}_i}{a} + \sum_{j\neq i}\frac{\mathcal{Q}_j\exp(-R_{ij}/\lambda_D)}{R_{ij}}\right] = \phi(a)$$

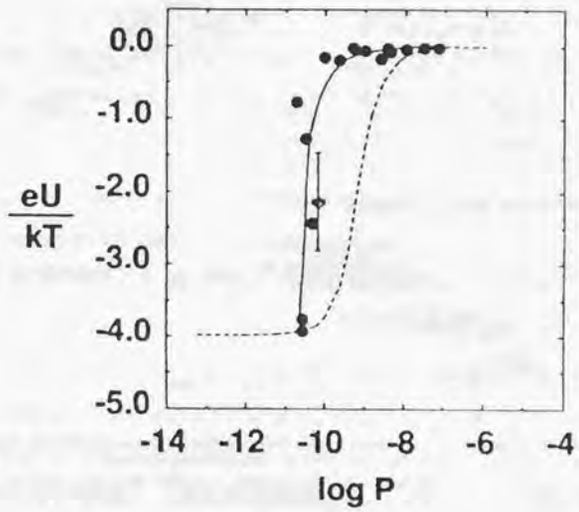

Figure 1.2: The variation of the grain surface potential U (which is denoted as $\varphi(a)$ in the text) in terms of k_BT/e as a function of $P = n_d a k_B T/\epsilon n_{i0}$ in units of mV. Note that $U = \varphi(a)$ is proportional to the grain charge $\mathcal{Q}$ as shown in Eq. (1.16). The experiment is done in a potassium plasma, where $n_d = 5\times10^4\text{cm}^{-3}$, $a = 5\mu\text{m}$ and $k_BT = 0.2\text{eV}$. The dashed line is the theoretical result obtained from Eqs. (1.14) and (1.15). (From Ref. 34).

for all i. This set of linear equations determines $\mathcal{Q}_i$ as a function of the known potential value $\phi(a)$, which is separately determined from Eqs. (1.14) and (1.15). In particular, if $N = 2$ and $R/\lambda_D \ll 1$, we obtain from the above equation[35,36]

$$Q(R) = \frac{Q(\infty)}{1 + a/R}. \tag{1.17}$$

If the charging frequency ν_c (i.e., the inverse of the time that a particle takes to acquire its equilibrium charge Q) is sufficiently higher than the typical frequency of particle motion (e.g., the plasma frequency of the particle $\omega_{pd} = \sqrt{Q^2 n_d/\varepsilon_0 M}$) with M being the grain mass, we may consider that charging takes place instantaneously in the time scale of particle motion and the particle charge is given by $Q(R)$ at each instant in time.

1.4. Grain transport in a plasma

We now consider the transport of an isolated grain in a plasma. The equation of motion of a grain with charge $\mathcal{Q} = -Q$ may be given by

$$M\frac{d\mathbf{V}}{dt} = \mathcal{Q}(\mathbf{E} + \mathbf{V}\times\mathbf{B}) + \mathbf{F}_G + \mathbf{F}_c + \mathbf{F}_{\rm other}, \tag{1.18}$$

just as the equation for any charged particles in a plasma. Unlike ions and electrons, however, the charge $\mathcal{Q}$ may vary as a function of time. In the equation above, $\mathbf{V}$ is the velocity of the grain, $\mathbf{E}$ and $\mathbf{B}$ are the ambient electric and magnetic fields, $\mathbf{F}_G$ is the gravitational force, and $\mathbf{F}_c$ is the sum of collisional forces between the particle and the background plasma, neutral gases and radiation fields. The other forces are represented by $\mathbf{F}_{\rm other}$, which includes the polarization force, as we shall discuss it in Chaps. 2 and 3.

In laboratory plasmas with weak or no magnetic fields, the transport of charged gains are usually determined by the balance between electrostatic force $\mathcal{Q}\mathbf{E}$ and collisional force $\mathbf{F}_c$. In space plasmas, where strong magnetic and gravitational fields are not uncommon, the Lorentz force $\mathcal{Q}\mathbf{V}\times\mathbf{B}$ and gravitational force $\mathbf{F}_G$ may be as dominant as other forces. For

example, in planetary magnetospheres, the plasma typically corotates with the planet (except for the distant magnetosphere where the solar wind may induce some plasma convections) whereas the grain particles essentially move on Keplerian orbits. Therefore, away from the synchronous orbit (where the Kepler velocity equals the corotation velocity), the drag force between the grains and the plasma can also become significant.

The collisional forces that often becomes large in laboratory and space plasma environments are the ion drag force $\mathbf{F}_i$, neutral drag force $\mathbf{F}_i$ and thermophoretic force $\mathbf{F}_{th}$. The ion drag force arises from the momentum transfer between the gain particle and ion flows due to Coulomb collisions. Similarly the neutral drag force is due to collisions between the grain particle and neutral gas flows. The thermophoretic force is caused by a temperature gradient of the background neutral gas. In the presence of a gas temperature gradient, a larger momentum transfer from the gas to the grain particle takes place on the side of the grain surface exposed to the higher temperature than that to the lower temperature. Therefore the net momentum transfer causes the particle to move in the direction opposite to the temperature gradient (i.e., the particle moves to the colder side), which is called thermophoresis.

Other collisional forces, which are usually considered to be less important in most dust-plasma environments, include photophoretic and diffusiophoretic forces. If a grain particle is subject to heating by electromagnetic radiation, the hotter, illuminated side of the particle bounces colliding gas molecules with higher velocities than the cooler, unilluminated side. As a result, the grain particle gains momentum from the background gas and moves away from the light source, which is called photophoresis (or sometimes called photothermophoresis[37]). Diffusiophoresis refers to the motion of a grain particle caused by density gradients of the ambient gases. Typically diffusiophoresis causes a grain particle move in the direction of the diffusion flux of the heavier gas component.[38]

Returning to the three important collisional forces — ion and neutral drag forces and thermophoresis, we now summarize the formulae for those forces in the following.

Ion drag

The gravitational dynamical friction on a star moving through a uniformly distributed background stars was first calculated by Chandrasekhar[39-41] under the assumption of small deflection angles and a Maxwellian distribution of the background star velocities. Since the inverse square force law applies to both the gravitational and Coulomb forces, the same formula holds for the Coulomb friction force on a test charged particle moving through a uniform background plasma.[42-44] The drag force $\mathbf{F}_i$ on a gain particle with charge $\mathcal{Q} = -Q$ due to Coulomb collisions with plasma ions is thus give by

$$F_i = \frac{q^2\mathcal{Q}^2}{8\pi\varepsilon_0^2}\frac{n_i}{k_BT_i}\left(1+\frac{m_i}{M}\right)\left[\frac{\mathrm{erf}(s)}{s^2}-\frac{2\exp(-s^2)}{s\sqrt{\pi}}\right]\ln\Lambda\,, \tag{1.19}$$

where

$$\mathrm{erf}(s) = \frac{2}{\sqrt{\pi}}\int_0^s \exp(-x^2)\,dx$$

and $s = v_0/v_{i,th}$ with v_0 being the relative velocity between the gain particle and the plasma and $v_{i,th} = \sqrt{2k_BT_i/m_i}$ being the ion thermal velocity. The Coulomb logarism $\ln\Lambda$ is defined by $\Lambda = b_{\max}/b_{\min}$, where $b_{\max}$ and $b_{\min}$ denotes the maximum and minimum impact parameters. The usual choices for these impact parameters are $b_{\max} = \lambda_D$ and $b_{\min} = a$. In the limit of small particle radius, i.e., $a \to 0$, one may choose $b_{\min} = |q\mathcal{Q}|/4\pi\varepsilon_0 k_BT_i$, which approximates the "minimum" distance at which an ion can approach the particle despite the Coulomb repulsion.[43] It should be noted that the formula (1.19) does not take into account possible large angle scattering or collective effects (i.e., self-consistent treatment of perturbed electric fields around the particulate). More accurate results including these effects are found in Ref. 44.

From Eq. (1.19), one can derive two limiting cases. One is the low speed limit, i.e., $s \ll 1$, where the ion drag force becomes proportional to the relative velocity v_0:

$$F_i = \frac{q^2Q^2}{6\pi^{3/2}\varepsilon_0^2}\frac{n_i}{k_BT_i}s\ln\Lambda\,. \tag{1.20}$$

The other is the high speed limit, i.e., $s \gg 1$, where the relative velocity v_0 is supersonic and the ion drag force becomes inversely proportional to v_0^2:

$$F_i = \frac{q^2Q^2}{8\pi\varepsilon_0^2}\frac{n_i}{k_BT_i}\frac{1}{s^2}\ln\Lambda\,. \tag{1.21}$$

Neutral drag

If the Reynolds number of the background gas is sufficiently small and the size of the grain particle is sufficiently larger than the mean free path of the gas molecules l_{mfp} (i.e., Knudsen number $\mathrm{Kn} = l_{\mathrm{mfp}}/a \ll 1$), the neutral drag force on the grain particulate is given by the well-known Stokes equation

$$F_n = 6\pi\eta a v_0\,, \tag{1.22}$$

where η is the viscosity of the gas and v_0 again denotes the particulate velocity relative to the gas flow.

However, most weakly ionized plasmas that we are concerned with have large Knudsen numbers, $\mathrm{Kn} \gg 1$. For example, a gas with the atmospheric pressure and room temperature has the number density $n_n = 0.25\times10^{20}\mathrm{cm}^{-3}$. For the typical molecular collision cross section $\sigma_n = 10^{-16}\mathrm{cm}^2$, the mean free path $l_{\mathrm{mfp}} = 1/n_n\sigma_n = 4\mu\mathrm{m}$. Therefore, for micron-size dust particles, the Knudsen number is usually large in subatmospheric-pressure discharges.

Let us consider a spherical particle with radius a in the limit of large Knudsen number $\mathrm{Kn} \gg 1$. The reflection of the gas molecules at the spherical grain surface is assumed to be either specular (i.e., the velocity component of the colliding molecule normal to the grain surface is reversed on collision whereas the tangential velocity component remains unchanged) or diffusive (i.e., the velocity distribution of the reflected molecules is Maxwellian with the gas temperature). In the case of diffuse reflection, Baines *et al.* obtained[45]

$$F_n = 2\pi^2a^2n_nk_BT_n\left[K(S)+\frac{\sqrt{\pi}}{3}S\right]\,, \tag{1.23}$$

where

$$K(S) = \left(S + \frac{1}{2S}\right)\frac{\exp(-S^2)}{\sqrt{\pi}} + \left(S^2 + 1 - \frac{1}{4S^2}\right)\mathrm{erf}(S),$$

and $S = v_0/v_{n,th}$ with $v_{n,th} = \sqrt{2k_BT_n/m_n}$ being the gas thermal velocity. For specular reflection, the second term in the bracket of Eq. (1.23) (i.e., the term $\sqrt{\pi}S/3$) should be omitted.[45]

In the low speed limit ($S \ll 1$), Eq. (1.23) reproduces Epstein's result[46]:

$$F_n = \frac{16}{3}\sqrt{\pi}a^2 n_n k_B T_n S\left(1 + \frac{\pi}{8}\right). \tag{1.24}$$

For specular reflection, the factor $(1+\pi/8)$ should be replaced by 1.[45,46] As in the case of the ion drag force, the neutral drag is proportional to the relative velocity v_0 if v_0 is sufficiently smaller than the gas thermal velocity $v_{n,th}$. In the high speed limit ($S \gg 1$), Eq. (1.23) reproduces McCrea's result[47]:

$$F_n = \pi a^2 n_n m_n v_0^2. \tag{1.25}$$

This formula applied to both reflective and diffusive reflections.

Thermophoresis

In the region of high Knudsen number (Kn $\gg 1$), the thermophoretic force is known to be given[14,48] by

$$F_{th} = -\frac{32}{15}\frac{a^2\chi_n}{v_{th}}\nabla T_n. \tag{1.26}$$

Here χ_n is the thermal conductiviety of the gas. For a polyatomic gas, χ_n needs to be replaced by the translational component of thermal conductivity, $\chi_{nt} = 15k_B\eta/4m_n$, where η is the gas viscosity. In the derivation of Eq. (1.26), it is assumed that a fraction of the gas molecules α are scattered diffusively whereas the other molecutles $(1-\alpha)$ suffers specular reflection at the surface. The final result, Eq. (1.26), is however independent of the diffusive reflection probability α.

1.5. Summary

In this chapter we have summarized some of the known results on charging mechanisms and forces for small gains immersed in plasmas. Due to their high mobility, the flux of electrons toward the particulate surface is generally larger than that of ions. Particulates in plasmas therefore typically carry negative charges. If the particles are subject to strong electromagnetic radiation or high energy electron bombardment, however, electrons emitted from the particulate surfaces may exceed those arriving from the plasma due to photoelectrons or secondary electron emission. Under such conditions, particulates may attain positive charges.

As the number density of grains increases, a significant fraction of the electrons may reside on the grain surfaces rather than in the plasma. In this situation, the further availability of electrons limit the grain charges. In addition, if two or more charged grains are sufficiently close to each other, the surface potential of each grain is also affected by the charges of the other grains. For a system of two particles, the magnitude of the particle charge decreases as the interparticle distance decreases, as given in Eq. (1.17).

The negative charge on a grain immersed in an electropositive plasma induces an ion-rich plasma layer (i.e.,the Debye sheath) around it. In a uniform plasma, the Debye sheath is spherical and its radius is given by the Debye length λ_D of Eq. (1.9). The Debye sheath shields the electric field of its own particle charge and the potential profile around the particulate is described by the Yukawa potential of Eq. (1.11).

In a non-uniform plasma, grain particles may be subject to the electromagnetic forces, ion and neutral drag forces, thermophoresis and other forces. If the plasma density is still uniform in the presence of the external electric field $\mathbf{E}$, the total electrostatic force exerted on the grain particle of charge Q is that of unshielded field, i.e., $Q\mathbf{E}$, as given by the first term of Eq. (1.18). If there is a sharp density gradient, however, the Debye sheath around

the particle is deformed since the Debye length λ_D is a function of the plasma density. The deformed sheath has a polarization, inducing an electric field at the center where the particle resides. This deformation of the sheath exerts an electrostatic force on the particle [which can be included in the term $\mathbf{F}_{other}$ in Eq. (1.18)]. In the next two chapters, we shall discuss the polarization force in detail based on a fluid description of the plasma.

References

[1]F. Hoyle and N. C. Wickramasinghe, *The Theory of Cosmic Grains*, Kluwer Academic Publishers, London (1991).

[2]C. K. Goertz, Rev. Geophys. **27**, 271 (1989).

[3]D. A. Mendis and M. Rosenberg, Annu. Rev. Astron. Astrophys. **32**, 419 (1994).

[4]S. Mitton (ed.), *The Cambridge Encyclopaedia of Astronomy*, Trewin Copplestone, London (1977).

[5]S. Hamaguchi, Butsuri**50**, 527 (1995).

[6]B. Ganguly, A. Garscadden, J. Williams and P. Haaland, J. Vac. Sci. Technol. A**11**, 1119 (1993).

[7]R. N. Carlile, S. Geha, J. F. O'Hanlon, and J. C. Stewart, Appl. Phys. Lett. **59**, 1167 (1991).

[8]A. Bouchoule, A. Plain, L. Boufendi, J. Ph. Blondeau, and C. Laure, J. Appl. Phys. **70**, 1991 (1991).

[9]G. S. Selwyn, J. Singh, and R. S. Bennett, J. Vac. Sci. Technol. A**7**, 2758 (1989).

[10]K. G. Spears, T. J. Robinson, and R. M. Roth, IEEE Trans. Plasma Sci. **14**, 179 (1986).

[11]G. S. Higashi, E. A. Irene and T. Ohmi (eds.), *Surface Chemical Cleaning and Passivation for Semiconductor Processing*, Material Research Society Symposium Proceedings **315**, Material Research Society, Pittsburgh (1993).

[12]D. H. Everett, *Basic Principles of Colloid Science*, The Royal Society of Chemistry, London (1988).

[13]B. V. Deriagin, *Theory of stability of colloids and thin films*, Consultants Bureau, New York (1989).

[14]N. A. Fuchs and A. G. Sutugin, *Highly Dispersed Aerosols*, Ann Arbor Science Publishers, Ann Arbor (1970).

[15]H. Ikezi, Phys. Fluids **29**, 1764 (1986).

[16]R. T. Farouki and S. Hamaguchi, Appl. Phys. Lett. **61**, 2973 (1992).

[17]S. G. Brush, H. L. Sahlin, and E. Teller, J. Chem. Phys. **45**, 2102 (1966).

[18]M. Baus and J.-P. Hansen, Phys. Rep. **59**, 1 (1980).

[19]S. Ichimaru, Rev. Mod. Phys. **54**, 1017 (1982).

[20]F. J. Rogers and H. E. DeWitt (eds.), *Strongly Coupled Plasma Physics*, Plenum Press, New York (1986).

[21]R. T. Farouki and S. Hamaguchi, Phys. Rev. E**47**, 4330 (1993).

[22]Y. Hayashi and K. Tachibana, Jpn. J. App. Phys. **33**, L804, (1994).

[23]H. Thomas, G. E. Morfill, V. Demmel, J. Goree, B. Feuerbacher, and D. Möhlmann, Phys. Rev. Lett. **73**, 652 (1994).

[24]J. H. Chu and I. Lin, Physica A **205**, 183 (1994).

[25]J. H. Chu and I. Lin, Phys. Rev. Lett. **72**, 4009 (1994).

[26]Th. Trottenberg, A. Melzer, A. Piel, Plasma Sources Sci. Technol. **4**, 450 (1995).

[27]E. C. Whipple, T. G. Northrop, and D. A. Mendis, J. Geophys. Res. **90**, 7405 (1985).

[28]T. G. Northrop, Physica Scripta **45**, 475 (1992).

[29]I. Bernstein and I. Rabinowitz, Phys. Fluids **2**, 112 (1959).

[30]M. Meyer-Vernet, Astron. Astrophys. **105**, 98 (1982).

[31]B. Chapman *Glow Discharge Processes*, John Wiley & Sons, New York (1980).

[32]A. von Engel *Ionized Gases*, Oxford Univ. Press (1965).

[33]L. Spitzer, *Physical Processes in the Interstellar Medium*, John Wiley & Sons, New York (1978).

[34]A. Barkan, N. D'Angelo and R. L Merlino, Phys. Rev. Lett. **73**, 3093 (1994).

[35]V. N. Tsytovich, Comments Plasma Phys. Controlled Fusion **15**, 349 (1994).

[36]S. Hamaguchi, Comments Plasma Phys. Controlled Fusion **18**, 95 (1997).

[37]J. Brock, J. Chem. Phys. **72**, 747 (1968).

[38]J. Brock, J. Colloid and Interface Sci. **27**, 95 (1968).

[39]S. Chandrasekhar, Astrophys. J. **97**, 255 (1943).

[40]S. Chandrasekhar, Rev. Mod. Phys. **15**, 1 (1943).

[41]S. Chandrasekhar, *Principles of Stellar Dynamics*, Dover, New York (1960).

[42]L. Spitzer, *Physics of Fully Ionized Gases*, 2nd Edition, Interscience Publishers, New York (1962).

[43]B. T. Draine and E. E. Salpeter, Ap. J. **231**, 77 (1979)

[44]T. G. Northrop and T. J. Birmingham, Planet. Space Sci. **38**, 319 (1990).

[45]M. J. Baines, I. P. Williams, and A. S. Asebiomo, Mon. Not. Roy. Astron. Soc. **130**, 63, (1965).

[46]P. Epstein, Phys. Rev. **23**, 710 (1924).

[47]W. H. McCrea, Mon. Not. Roy. Astron. Soc. **95**, 509 (1935).

[48]L. Waldmann and K. H. Schmitt, in *Aerosol Sciences*, (ed. by C. N. Davies) Academic Press, New York (1962).

Chapter 2

Polarization force due to sheath deformation

2.1. Introduction

In this chapter, we are concerned with the transport of an isolated particulate, in particular with the force exerted on it by the ambient plasma.[1] Since the sizes of particulates and their Debye sheaths are typically small on the macroscopic scale (e.g., the dimensions of the discharge chamber), the particulate dynamics are determined by local plasma parameters such as the electric field, plasma density gradient, etc., at the position of the particulate. We will exploit this scale discrepancy to obtain the force as a function of macroscopic plasma parameters. Such a functional dependence may be used in conjunction with macroscopic (e.g., fluid or particle-in-cell) simulations to determine the overall particulate transport characteristics in the discharge.

As is discussed in the preceding chapter, a charged particle in a plasma is surrounded by a Debye sheath, which shields its long-range Coulomb field. Particulates in plasmas are typically negatively charged — due to the high mobility of the plasma electrons — so their Debye sheaths comprise an excess of positive ions and a deficiency of electrons. The problem addressed in this chapter is that of whether, in the presence of an external electric field, the Debye shielding effectively diminishes the magnitude of this field at the particle location (by

for example, a re-distribution of the sheath charges).

As will be clarified later, the Debye sheath does *modify* the externally applied field by a re-distribution (i.e., polarization) of the sheath charges. However, the external field is not necessarily "shielded" or diminished at the position of the particulate; the Debye sheath may either reduce or enhance the external field, depending on the sense of the mean density gradient at the particulate. In a non-uniform plasma, the deviation of the force from the nominal value $\mathcal{Q}\mathbf{E}$, that a particulate of charge $\mathcal{Q}$ would experience in a field $\mathbf{E}$ in the absence of the plasma, may be called the "polarization force" since it is due solely to the sheath polarization (neglecting ion drag force). In particular, a spherically symmetric Debye sheath would not shield the external electric field at all (although it does shield the Coulomb field of the particulate that it surrounds).

Although these characteristics of Debye shielding may be explained (see Sec. 2.6 below) intuitively, it is not a trivial matter to rigorously demonstrate them. Estimating the total force on a particulate involves not only calculation of the electrostatic sheath-polarization force, but also the contribution of pressure forces on the particulate due to the ambient plasma. It is not obvious that this pressure force and the sheath-polarization force are both small for a small particulate. The pressure force is mainly due to the positive ions, which are electrostatically attracted by the negatively-charged particulate (in this sense, the pressure force also has electrostatic origins). Generally, the ion density increases toward the particulate, and for a small particulate in a uniform plasma, the spherical symmetry of the particulate ensures zero net force due to the ion pressure. In a non-uniform plasma, however, a slight imbalance between the pressure force on one side of the particulate and that on the other may result in a finite net force even in the limit of zero particulate size. In other words, one needs detailed calculations of the pressure force to determine its magnitude, even for an infinitesimal particulate.

We now estimate the magnitude of the polarization force. As mentioned above, in a

non-uniform plasma the Debye length λ_D (which represents the thickness of the sheath) is a function of position, and the sheath around a particulate is no longer spherically symmetric. The deformed (i.e., polarized) sheath creates an electric field at the particulate location, and exerts a force — the polarization force — in addition to the external-field force $\mathcal{Q}\mathbf{E}$.

If the Debye length is $\lambda_D = 20\mu$m and the scale length for macroscopic variations is $L = 1$cm (typical values for materials-processing plasmas) the variation of macroscopic plasma variables, such as the electrostatic potential, over the sheath is very small, of order $\lambda_D/L = 2\times10^{-3}$. However, even small charge separations may create large electric fields. Let us assume that the sheath is polarized due to the plasma non-uniformity, creating an excess charge $Q\lambda_D/L$ at one end of the sheath and $-Q\lambda_D/L$ at the other (the particulate has charge $\mathcal{Q} = -Q$, so the sheath contains the opposite charge Q more or less within a sphere of radius λ_D). This charge separation creates an electric field, which exerts a force F_1 on the particulate, given roughly by

$$F_1 \simeq Q\frac{Q\lambda_D/L}{\varepsilon_0\lambda_D^2}.$$

Comparing the polarization force F_1 with the direct electric field force $F_0 = QE$, where we take $E \simeq k_BT_e/eL$ (e and T_e being electron charge and temperature), we obtain

$$\frac{F_1}{F_0} \simeq \frac{eQ}{\varepsilon_0\lambda_D k_BT_e} = \frac{Z_D}{\lambda_e^2\lambda_D n_e}.$$

Here n_e is the electron density, $Q = Z_De$, and we have used the definition of the electron Debye length $\lambda_e = (\varepsilon_0k_BT_e/e^2n_e)^{\frac{1}{2}}$. Introducing the plasma parameter $g = 1/\lambda_e^3n_e$, which is typically small — $g \ll 1$ is indeed a condition for a system of charged particles to be a "plasma"[7] — we obtain

$$\frac{F_1}{F_0} \simeq gZ_D\frac{\lambda_e}{\lambda_D}$$

Typically, $Z_D \gg 1$ and $\lambda_e \gtrsim \lambda_D$, so the ratio F_1/F_0 may be of order 1, i.e., the polarization force F_1 may be comparable to the direct electrostatic force $F_0 = QE$. To determine the

magnitude of F_1 more accurately, one needs a detailed analysis, which will be presented below.

For the sake of simplicity, we do not consider effects of a finite plasma flow in this chapter. The plasma flow, especially ion flow, influences the transport of particulates in two ways. One is to exert an (ion) drag force, which represents the effect of Coulomb collisions between ions and the charged grain, and incurs a change of the ion velocity distribution function. The other is a fluid-like effect, by which the ion flow modifies the shape of the Debye sheath. In particular, when the ion flow velocity is sufficiently large compared to the ion thermal velocity, $v_{th} = (k_B T_i/m_i)^{\frac{1}{2}}$ where T_i and m_i are the ion temperature and mass, the ions are unable to form a sheath around the particulate and consequently the Debye sheath consists only of a deficiency of electrons (the ion sheath is "blown away" by the strong ion flow). Under such conditions, the ion density distribution is almost uniform in the sheath. This fluid-like effect does not involve a change of the ion velocity distribution function.

A comprehensive study of drag forces on a particulate in a uniform plasma has recently been given by Northrop and Birmingham,[3] where large-angle Coulomb scattering,[4] dynamical friction,[5,6] and collective effects[7] are treated systematically based on the theory by Hubbard[8] and Kihara and Aono.[9] This kinetic theory by Northrop and Birmingham simultaneously deals with both effects — drag force and fluid-like effects — that we mentioned above for a uniform plasma. For a non-uniform plasma, which we are concerned with here, a similar kinetic treatment is more complex and beyond the scope of the present work. However, a more detailed study of fluid-particulate interactions in a non-uniform plasma, deferred to Chap. 3, generalizes the results of this chapter and shows that the sheath deformation due to a finite ion flow (i.e., the fluid-like effect mentioned above) has only a minor influence on the force exerted on particulates. In other words, the sum of the force presented in this chapter and the usual ion drag force[4] accounts for the particulate transport in an non-uniform plasma.

This chapter is organized as follows. In Sec. 2.2 we introduce our model of a charged particulate immersed in a non-uniform plasma. The electrostatic force is then obtained for infinitesimal and finite-radius particulates in Secs. 2.3 and 2.4. Noting that, in the absence of a finite plasma flow, the total force on the particulate is only the sum of the electrostatic force and pressure force, we derive the pressure force and total force in Sec. 2.5. In Sec. 2.6, a physical interpretation for the results obtained in Secs. 2.2 to 2.5 is presented, and in Sec. 2.7 the magnitude of the polarization force is estimated under realistic glow discharge conditions. Finally, Sec. 2.8 summarizes our results and briefly discusses effects of finite ion flows on the particulate force.

2.2. Formulation

As in Sec. 1.2, we consider an unmagnetized plasma, in which the electrostatic potential, ion and electron densities, and ion flow velocity at position $\mathbf{r}$ are given by $\Psi_0(\mathbf{r})$, $n_{i0}(\mathbf{r})$, $n_{e0}(\mathbf{r})$, and $\mathbf{v}_{i0}(\mathbf{r})$. Here the subscript 0 indicates macroscopic variables. Unlike in Sec. 1.2, however, these macroscopic variables are assumed to vary weakly over the small scale of the ion or electron Debye lengths. The mean charge density is then $\rho_0 = qn_{i0} - en_0$. We again assume ions of single species for simplicity. The extension to multiple species is straightforward. The potential satisfies Poisson's equation, $\Delta\Psi_0 = -\rho_0/\varepsilon_0$. The plasma and electric field are sustained by some external means, such as a voltage applied to the electrodes. In this sense, the field may be called an externally applied field, although the plasma adjusts itself to determine the electric field profile, $\mathbf{E}_0(\mathbf{r}) = -\nabla\Psi_0$.

Suppose a small particulate with a negative charge $-Q$ is now placed at $\mathbf{r} = \mathbf{0}$. The resultant field potential $\Psi(\mathbf{r})$ again satisfies Poisson's equation:

$$\Delta\Psi(\mathbf{r}) = -\frac{\rho(\mathbf{r})}{\varepsilon_0}, \tag{2.1}$$

where $\rho(\mathbf{r})$ denotes the total charge density given by

$$\rho(\mathbf{r}) = -Q\delta(\mathbf{r}) + qn_i(\mathbf{r}) - en_e(\mathbf{r}), \tag{2.2}$$

and $n_i(\mathbf{r})$ and $n_e(\mathbf{r})$ are ion and electron densities after the perturbation. Here the particulate is assumed to be infinitesimally small. The boundary conditions are given by

$$\Psi(\mathbf{r}) \to \Psi_0(\mathbf{r}) \quad \text{as} \quad |\mathbf{r}| \to \infty. \tag{2.3}$$

As for Eqs. (1.5) and (1.6), we assume that the local ion and electron densities are then given by the Boltzmann distributions as

$$n_i(\mathbf{r}) = n_{i0}(\mathbf{r}) \exp\left[\frac{-q\varphi(\mathbf{r})}{k_B T_i}\right], \tag{2.4}$$

$$n_e(\mathbf{r}) = n_{e0}(\mathbf{r}) \exp\left[\frac{e\varphi(\mathbf{r})}{k_B T_e}\right], \tag{2.5}$$

where

$$\varphi(\mathbf{r}) = \Psi(\mathbf{r}) - \Psi_0(\mathbf{r}).$$

The macroscopic variables $n_{i0}(\mathbf{r})$, $n_{e0}(\mathbf{r})$, and $\Psi_0(\mathbf{r})$ are slowly varying functions of $\mathbf{r}$, in the sense that $|\nabla\Psi_0(\mathbf{r})| \ll |\nabla\varphi(\mathbf{r})|$, etc.

Following Sec. (1.2), we again employ the Debye–Hückel approximation and limearize Eqs. (2.4) and (2.5) with respect to φ. Substituting the resulting expressions for $n_i(\mathbf{r})$ and $n_e(\mathbf{r})$ into Eq. (2.1) and subtracting Poisson's equation for the mean field, $\Delta\Psi_0 = -\rho_0/\varepsilon_0$, we obtain

$$\Delta\varphi(\mathbf{r}) = \frac{Q}{\varepsilon_0}\delta(\mathbf{r}) + k_D^2(\mathbf{r})\varphi(\mathbf{r}), \tag{2.6}$$

where k_D is defined in Eq. 1.8. Note that the characteristic Debye length $\lambda_D(\mathbf{r})$, defined by $\lambda_D(\mathbf{r}) = k_D^{-1}(\mathbf{r})$, is in general spatially dependent. The boundary condition for Eq. (2.6) is again given by is given by

$$\varphi(\mathbf{r}) \to 0 \quad \text{as} \quad |\mathbf{r}| \to \infty.$$

2.3. Electrostatic potential

We now solve Poisson's equation (2.6) to obtain the electric field potential around the particulate. Here the spatial dependence of $k_D = \lambda_D^{-1}$ is assumed to be weak, in the sense that $\nabla k_D/k_D \sim \delta \equiv \lambda_D/L$, with L being the macroscopic scale length. Therefore, we may expand the function $k_D^2(\mathbf{r})$ around the particulate position $\mathbf{r} = \mathbf{0}$ in a Taylor series to obtain

$$k_D^2(\mathbf{r}) = k_0^2 + \mathbf{r}\cdot\nabla k_D^2,$$

where $k_0 = \lambda_0^{-1} = k_D(\mathbf{0})$ is the inverse Debye length at $\mathbf{r} = \mathbf{0}$ and ∇k_D^2 is also evaluated at $\mathbf{r} = \mathbf{0}$. Taking the direction of ∇k_D^2 as the z–direction, we may write

$$k_D^2(z) = k_0^2 + \sigma z, \tag{2.7}$$

where $\sigma = |\nabla k_D^2|$. In terms of the Debye length λ_D, we have

$$\nabla k_D^2 = -\frac{2}{\lambda_0^3}\nabla\lambda_D, \tag{2.8}$$

or $\sigma = -2|\nabla\lambda_D|/\lambda_D^3$, evaluated at $\mathbf{r} = \mathbf{0}$.

Since the second term of Eq. (2.7) is smaller than the first (i.e., $\sigma z/k_0^2 \sim \delta$), we may solve Eq. (2.6) using a perturbation method: we write $\varphi(\mathbf{r}) = \varphi^{(0)}(\mathbf{r}) + \varphi^{(1)}(\mathbf{r})$, where the 0th order solution $\varphi^{(0)}$ satisfies

$$\Delta\varphi^{(0)}(\mathbf{r}) = \frac{Q}{\varepsilon_0}\delta(\mathbf{r}) + k_0^2\varphi^{(0)}(\mathbf{r}), \tag{2.9}$$

and the first–order correction $\varphi^{(1)}(\mathbf{r})$ satisfies

$$\Delta\varphi^{(1)}(\mathbf{r}) - k_0^2\varphi^{(1)}(\mathbf{r}) = \sigma z\varphi^{(0)}(\mathbf{r}). \tag{2.10}$$

The appropriate boundary conditions are $\varphi^{(0)}, \varphi^{(1)} \to 0$ as $|\mathbf{r}| \to \infty$.

The solution to the 0th–order equation (2.9) is the well–known screened Coulomb potential

$$\varphi^{(0)}(\mathbf{r}) = -\frac{Q}{4\pi\varepsilon_0}\frac{\exp(-k_0 r)}{r}, \tag{2.11}$$

where $r = |\mathbf{r}|$. With the use of this expression for $\varphi^{(0)}$, the solution to the first-order equation (2.10) is given by

$$\varphi^{(1)}(\mathbf{r}) = \frac{\sigma Q}{16\pi\varepsilon_0 k_0} z \exp(-k_0 r). \tag{2.12}$$

One can easily confirm Eq. (2.12) by substitution into Eq. (2.10). For a more systematic derivation of $\varphi^{(1)}$, see Appendix B.

The total charge density $\rho(\mathbf{r})$ is then given by

$$\rho(\mathbf{r}) = \rho_0(\mathbf{r}) - Q\delta(\mathbf{r}) + \rho_s(\mathbf{r}),$$

where $\rho_s(\mathbf{r})$ is the charge density of the Debye sheath, given by

$$\rho_s(\mathbf{r}) = -\varepsilon_0 k_0^2 [\varphi_0(\mathbf{r}) + \varphi_1(\mathbf{r})] - \varepsilon_0 \sigma z \varphi_0(\mathbf{r})$$

$$= \frac{k_0^2 Q}{4\pi}\left[\frac{\exp(-k_0 r)}{r} + \left(\frac{1}{r} - \frac{k_0}{4}\right)\frac{\sigma \exp(-k_0 r)}{k_0^2} z\right]. \tag{2.13}$$

In Eq. (2.13) we have retained terms to first order in $\delta = \lambda_D/L$.

Figure 2.1 shows the contour lines of the potential $\varphi = \varphi^{(0)} + \varphi^{(1)}$ given by Eqs. (2.11) and (2.12). The closed circle at the center represents the position of the particulate. Here the potential is normalized by $Qk_0/4\pi\varepsilon_0$, and the parameter σ/k_0^3 ($\simeq \lambda_D/L$) is chosen to be 0.01. Note that the contours are at logarithmic intervals. As is clearly seen, the Debye length $\lambda_D(z)$ is smaller for larger z, resulting in a positive potential — overshooting in φ — for $z/\lambda_D \gtrsim 20$. Similarly, Fig. 2.2 shows the charge density distribution around the particulate under the same conditions. The charge density is seen to be negative for $z/\lambda_D \gtrsim 20$, indicating polarization of the Debye sheath.

The dipole moment of the particulate-sheath system is given by

$$\mathbf{P} = \int \mathbf{r}\rho_s(\mathbf{r})\, d\mathbf{r},$$

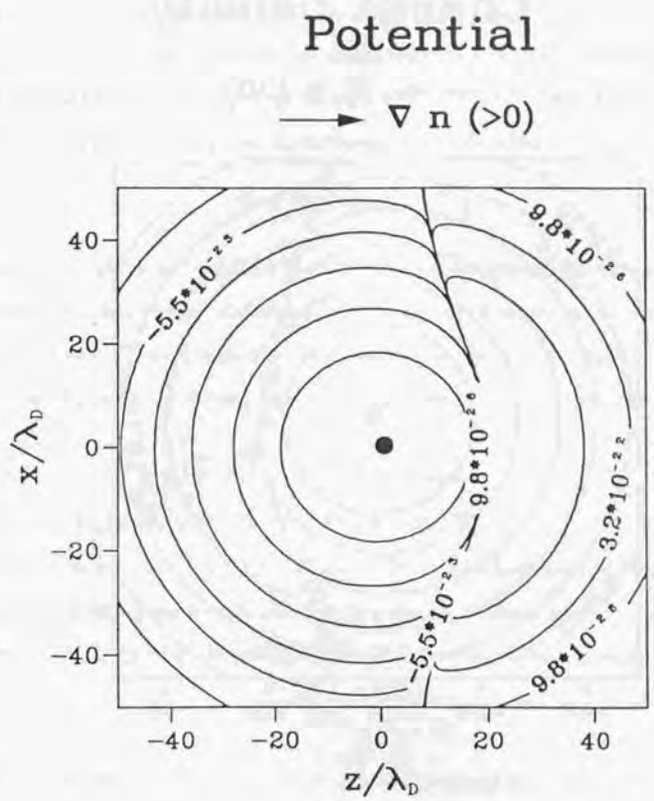

Figure 2.1: Contour lines (on a logarithmic scale) of the sheath potential $\varphi = \varphi^{(0)} + \varphi^{(1)}$ given by Eqs. (2.11) and (2.12). The mean field potential Ψ_0 is not depicted. The potential is normalized by $Qk_0/4\pi\varepsilon_0$.

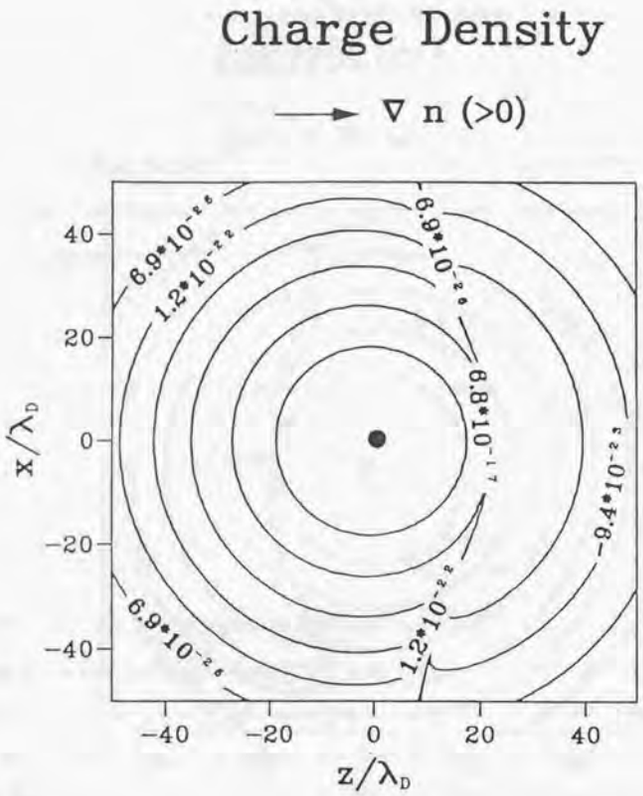

Figure 2.2: Contour lines (on a logarithmic scale) of the sheath charge density ρ_s given by Eq. (2.13) under the same conditions as those in Fig. 2.2. The background charge density ρ_0 is not depicted. The charge density is normalized by $Qk_0^3/4\pi$.

which yields $\mathbf{P} = 0$ upon substitution of ρ_s as in Eq. (2.13). In other words, the particulate-sheath system possesses no dipole moment, as one might expect (note that the plasma sheath can "shield" any multipole moment, including a monopole, i.e., a bare charge.)

The electrostatic force on the particulate may be calculated as

$$\mathbf{F}^{\mathrm{ES}} = Q\nabla\left[\Psi(\mathbf{r}) - \frac{-Q}{4\pi\varepsilon_0 r}\right],$$

where $\Psi = \Psi_0 + \varphi^{(0)} + \varphi^{(1)}$ and the second term in the parentheses represents the self-field due to the particulate charge $-Q$ that needs to be subtracted for the force calculation. Since this self-field and $\varphi^{(0)}$ are spherically symmetric, the only potentials that contribute to the net force are Ψ_0 and $\varphi^{(1)}$. Writing $\mathbf{E}_0 = -\nabla\Psi_0$ and using Eq. (2.12), we obtain

$$F_z^{\mathrm{ES}} = -QE_0 + \frac{\sigma Q^2}{16\pi\varepsilon_0 k_0}. \tag{2.14}$$

Here F_z^{ES} and E_{0z} denote the z-components of $\mathbf{F}^{\mathrm{ES}}$ and $\mathbf{E}_0$.

As will be shown in Sec. 2.5, the pressure force $\mathbf{F}^{\mathrm{P}}$ on the infinitesimal particulate vanishes, so Eq. (2.14) indeed gives the total force in the absence of mean ion flow (i.e., there is no drag force). Using Eq. (2.8) the total force, to $\mathcal{O}(\delta)$, may be written in vector form as

$$\mathbf{F} = -Q\mathbf{E}_0 - \frac{Q^2\nabla\lambda_D}{8\pi\varepsilon_0\lambda_D^2}. \tag{2.15}$$

The (Helmholtz) free energy F_H, which may be calculated from $F_H = -\int^z F_z\,dz$, is then given by

$$F_H = -Q\Psi_0 - \frac{Q^2}{8\pi\varepsilon_0\lambda_D}, \tag{2.16}$$

where Ψ_0 and λ_D are evaluated at the particle position. In Eq. (2.16), the free energy of the unperturbed system is set to zero. Note that the polarization force — the second term of Eq. (2.15) — is always in the direction of decreasing Debye length, regardless of the sign of the particulate charge. In other words, as may be seen from Eq. (2.16), the particulate has a lower free energy when it has a thinner Debye sheath (i.e., smaller λ_D).

2.4. Finite–radius effects

We now extend the preceding calculation to particulates of finite radius. For simplicity, we assume that the particulate is a perfect spherical conductor of radius a. The radius a may be comparable to the Debye length λ_D but should be significantly smaller than the macroscopic scale length (i.e., $a, \lambda_D \ll L$). The assumptions regarding plasma properties made in Sec. 2.2 are employed also in this section.

The problem may be formulated in the same manner as in Sec. 2.2, except that the total charge is now given by

$$\rho(\mathbf{r}) = qn_i(\mathbf{r}) - en_e(\mathbf{r})$$

in the plasma, and the boundary conditions are

$$\Psi(\mathbf{r}) \to \Psi_0(\mathbf{r}) \quad \text{as} \quad r \to \infty \tag{2.17}$$

$$\Psi(\mathbf{r}) = \Psi_0(0) + V_s \quad \text{at} \quad r = a\,, \tag{2.18}$$

instead of Eqs. (2.2) and (2.3). In Eq. (2.18), V_s denotes a constant voltage on the particulate surface (measured from the background potential Ψ_0 at $\mathbf{r} = 0$), which is a function of the total charge $-Q$ residing on the surface through the relation

$$Q = \varepsilon_0 \oint_{r=a} \frac{\partial \Psi}{\partial r}\, dS\,. \tag{2.19}$$

the integration being over the particulate surface (note that the quantity $-\varepsilon_0 \partial\Psi/\partial r|_{r=a}$ represents the surface charge density).

Writing $\varphi(\mathbf{r}) = \varphi^{(0)}(\mathbf{r}) + \varphi^{(1)}(\mathbf{r})$ again, the 0th order solution now satisfies

$$\Delta\varphi^{(0)}(\mathbf{r}) = k_0^2 \varphi^{(0)}(\mathbf{r})\,, \tag{2.20}$$

with the boundary conditions $\varphi^{(0)} \to 0$ as $r \to \infty$ and $\varphi^{(0)} = V_s$ at $r = a$. Here we have assumed that $\Psi_0(z) = \Psi_0(0) - E_0 z$, neglecting $\mathcal{O}(\delta^2)$ terms ($\delta = \lambda_D/L$ as before). The

solution to Eq. (2.20) is readily obtained as

$$\varphi^{(0)}(\mathbf{r}) = \frac{V_s a \exp[-k_0(r-a)]}{r}\,. \tag{2.21}$$

The first–order equation for $\varphi^{(1)}$ is given by Eq. (2.10), but with boundary conditions $\varphi^{(1)} \to 0$ as $r \to \infty$ and $-E_0 a \cos\theta + \varphi^{(1)}(\mathbf{r}) = 0$ at $r = a$. Here θ denotes the polar angle measured from the z–axis. Substituting Eq. (2.20) into Eq. (2.10) and solving the resulting equation, we obtain

$$\varphi^{(1)}(\mathbf{r}) = E_0 \left(\frac{a}{r}\right)^3 \left(\frac{1+k_0 r}{1+k_0 a}\right) \exp[-k_0(r-a)]z$$

$$-\frac{\sigma a V_s}{4k_0}\left(\frac{a}{r}\right)^3 \left(\frac{1+k_0 r}{1+k_0 a} - \frac{r^3}{a^3}\right) \exp[-k_0(r-a)]z\,, \tag{2.22}$$

where $z = r\cos\theta$. It is straightforward to confirm that the above expression for $\varphi^{(1)}$ indeed satisfies Eq. (2.10). Note that $\varphi^{(1)} = E_0 a \cos\theta$ on the surface of the particulate, which also satisfies the boundary condition stated above. A systematic derivation of Eq. (2.22) from Eq. (2.10) is given in Appendix B.

To relate the potential V_s to the particle charge $-Q$, we now substitute $\Psi = \Psi_0 + \varphi^{(0)} + \varphi^{(1)}$ into Eq. (2.19) to obtain $V_s = -Q/4\pi\varepsilon_0(1+k_0 a)a$, or

$$\varphi^{(0)}(\mathbf{r}) = -\frac{Q\exp[-k_0(r-a)]}{4\pi\varepsilon_0(1+k_0 a)r}\,, \tag{2.23}$$

and

$$\varphi^{(1)}(\mathbf{r}) = E_0 \left(\frac{a}{r}\right)^3 \left(\frac{1+k_0 r}{1+k_0 a}\right) \exp[-k_0(r-a)]z$$

$$+\frac{\sigma Q}{16\pi\varepsilon_0(1+k_0 a)k_0}\left(\frac{a}{r}\right)^3 \left(\frac{1+k_0 r}{1+k_0 a} - \frac{r^3}{a^3}\right) \exp[-k_0(r-a)]z\,. \tag{2.24}$$

The electrostatic force exerted on the particulate is given by

$$\mathbf{F}^{ES} = \int_{r\le a} \rho(\mathbf{r})\mathbf{E}(\mathbf{r})\, d\mathbf{r}$$

$$= \varepsilon_0 \oint_{r=a} \left[\mathbf{E}(\mathbf{E}\cdot\hat{\mathbf{n}}) - \frac{1}{2}\mathbf{E}^2\hat{\mathbf{n}} \right] dS\,,$$

where $\mathbf{E} = -\nabla\Psi$, $\hat{\mathbf{n}}$ is an outward unit normal vector on the particulate surface, and the above integral is taken over the entire surface. Substituting $\mathbf{E} = \mathbf{E}_0 - \nabla(\varphi^{(0)} + \varphi^{(1)})$, we obtain

$$F_z^{ES} = QE_0 \left[1 + \frac{k_0^2 a^2}{3(1+k_0 a)} \right] + \frac{\sigma Q^2 (1 + 2k_0 a/3)}{16\pi\varepsilon_0 (1+k_0 a)^2 k_0}\,. \tag{2.25}$$

Note that Eq. (2.25) agrees with Eq. (2.14) when $k_0 a = 0$.

In the case of a finite-radius particulate, the external electric field $\mathbf{E}_0$ determines the charge distribution on the particulate's conducting surface, i.e., the polarization of the particulate. The polarized surface charges then create an electric field represented by the first term in Eq. (2.24), which in turn exerts an electrostatic force on the particulate given by the second term in the bracket of Eq. (2.25). Note that this force, which exists even in the case $\sigma = 0$, is unrelated to the polarization of the sheath. This particulate-polarization field, however, also exerts a force on the plasma, increasing the ion pressure on the particulate. As will be shown in the following section, the ion pressure force exactly cancels this particulate-polarization force (but not the sheath-polarization force given by the second term of Eq. (2.24)).

2.5. Pressure forces

Besides the drag force, the only forces that are exerted on a particulate are the direct electrostatic force (which was derived in the previous sections) and the pressure force due to the ambient plasma. As discussed in Sec. 2.1, the magnitude of the pressure force is not obviously negligible, especially in the case of a finite-radius particulate. The pressure force is also strongly influenced by the electrostatic field around the particulate, since the densities of ions and electrons are determined by the local electric field. Thus, in order to assess the

effects of an external electric field, the pressure force must be self-consistently taken into account.

Expanding Eq. (2.4), the ion pressure may be written as

$$p_i(\mathbf{r}) = k_B T_i n_i(\mathbf{r}) = k_B T_i n_{i0}(\mathbf{r}) - q n_{i0}(\mathbf{r})\varphi + \frac{1}{2} q^2 \beta_i n_{i0}(\mathbf{r})\varphi^2\,,$$

where $\beta_i = 1/(k_B T_i)$. A similar expressure holds for the electron pressure, using Eq. (2.5). The sum of these pressure expressions yields the total pressure

$$p(\mathbf{r}) = p_0(\mathbf{r}) - \rho_0(\mathbf{r})\varphi + \frac{\varepsilon_0}{2} k_D^2(\mathbf{r})\varphi^2\,. \tag{2.26}$$

Here we have taken the expansion to order ε^2, where $\varepsilon \sim e\beta_e\varphi$, since the third term in Eq. (2.26) may be dominant near the particulate surface. To see this more clearly, we cast Eq. (2.26) in dimensionless form as

$$\tilde{p}(\mathbf{r}) = \tilde{p}_0(\mathbf{r}) - \frac{\rho_0(\mathbf{r})}{q n_{e0}(0)}\tilde{\varphi} + \frac{1}{2} k_D^2(\mathbf{r})\lambda_e^2 \tilde{\varphi}^2\,, \tag{2.27}$$

where

$$\tilde{\varphi} = e\beta_e\varphi \quad \text{and} \quad \tilde{p} = \beta_e p / n_{e0}(0)\,.$$

In Eq. (2.27), note that $k_D^2(\mathbf{r})\lambda_e^2 = \mathcal{O}(1)$ while the coefficient of the second term is $\rho_0/q n_{e0}(0) = \mathcal{O}(\delta^2)$, where $\delta = \lambda_e/L$, since $\rho_0 \simeq \varepsilon_0\Psi_0/L^2$ and $\Psi_0 \simeq 1/e\beta_e$. Thus, since $\tilde{\varphi} = \mathcal{O}(\varepsilon)$, the third term dominates over the second term if $\delta = \lambda_e/L \sim \varepsilon$. In particular, in the limit of a uniform plasma, the first and second terms in Eq. (2.27) vanish, and the pressure is due solely to the third term, i.e, to ions and electrons in the sheath.

Therefore, assuming that $\delta = \lambda_e/L \sim \varepsilon$ and taking terms to $\mathcal{O}(\varepsilon^3)$ in Eq.(2.27), we may rewrite Eq. (2.26) as

$$p(\mathbf{r}) = p_0(z) - \rho_0(0)\varphi + \frac{\varepsilon_0}{2}(k_0^2 + \sigma z)\varphi^2\,, \tag{2.28}$$

where for the background pressure $p_0(z)$ we take its Taylor expansion around $\mathbf{r} = 0$ only up to $\mathcal{O}(\varepsilon^3)$. In Eq. (2.28), the background quantities are assumed to depend only on z, as before.

The pressure force on the particulate is then calculated from

$$\mathbf{F}^p = -\oint p\,\hat{\mathbf{n}}\,dS\,,$$

where the integration is taken over the particulate surface with outward normal unit vector $\hat{\mathbf{n}}$. The z component of $\mathbf{F}^p$ may be expressed as

$$F_z^p = -2\pi a^2 \int_0^\pi p\cos\theta\sin\theta\,\theta\,. \tag{2.29}$$

Substituting Eq. (2.28) into Eq. (2.29), we obtain

$$F_z^p = -\frac{4}{3}\pi a^3 p_0' - \frac{2}{15}\pi a^5 p_0''' + \frac{4}{3}\pi a^3 \rho_0 E_0 - \frac{QE_0(k_0a)^2}{3(1+k_0a)} - \frac{\sigma a Q^2}{24\pi\varepsilon_0(1+k_0a)^2} - \frac{2}{5}\pi a^5 \varepsilon_0 \sigma E_0^2\,. \tag{2.30}$$

In deriving Eq. (2.30) we use $\varphi^{(0)} = Q/4\pi\varepsilon_0(1+k_0a)a$ and $\varphi^{(1)} = E_0 a\cos\theta$. Note that the magnitudes of $\varphi^{(0)}$ and $\varphi^{(1)}$ are of the same order at the surface, i.e., $e\beta_e\varphi^{(0)} \sim e\beta_e\varphi^{(1)} \sim \varepsilon$, since $E_0 \sim 1/e\beta_e L$ and $a \lesssim \lambda_e$.

If the particulate radius is sufficiently small compared to the Debye length (i.e., $a \ll \lambda_e$), which is usually the case for laboratory or space plasmas, it suffices to take terms up to $\mathcal{O}(k_0^2a^2)$ in Eq. (2.30):

$$F_z^p = -\frac{QE_0(k_0a)^2}{3(1+k_0a)} - \frac{\sigma a Q^2}{24\pi\varepsilon_0(1+k_0a)^2}\,. \tag{2.31}$$

The first term above represents the pressure force due to the sheath polarization field. As mentioned in Sec. 2.3, this pressure force vanishes as $a \to 0$.

Adding Eqs. (2.25) and (2.31), we have the total force on a small particulate (i.e., $a \ll \lambda_e$): $F_z = F_z^{KS} + F_z^p$. In vector form, this may be written as

$$\mathbf{F} = -Q\mathbf{E}_0 - \frac{Q^2}{8\pi\varepsilon_0(1+k_Da)^2}\frac{\nabla\lambda_D}{\lambda_D^2}\,, \tag{2.32}$$

where all the plasma quantities (such as $\mathbf{E}_0$ and λ_D) are evaluated at the particulate position, i.e., $\mathbf{r} = \mathbf{0}$.

The free energy F_H may be calculated from Eq. (2.32) in a manner similar to that used to obtain Eq. (2.16):

$$\begin{aligned} F_H &= -Q\Psi_0 + \frac{Q^2}{8\pi\varepsilon_0 a(1+k_Da)} \\ &= -Q\Psi_0 - \frac{Q^2k_D}{8\pi\varepsilon_0(1+k_Da)} + \frac{Q^2}{8\pi\varepsilon_0 a}\,, \end{aligned} \tag{2.33}$$

where Ψ_0 and $k_D = 1/\lambda_D$ are evaluated at the particulate position. The third term in Eq. (2.33) represents the self-energy of the particulate, which becomes infinity as $a \to 0$. This self-energy is not included in Eq. (2.16); the first and second terms of Eq. (2.33) agree with Eq. (2.16) in the limit $a \to 0$.

2.6. The role of Debye sheaths

We have shown that, in the absence of plasma flows, the total force on a particulate is the sum of the direct electrostatic force exerted by the external field and the sheath polarization force. In particular, in the case of uniform density ($\sigma = 0$), the total force on the charge $-Q$ is exactly $-Q\,\mathbf{E}_0$. Thus, although an unpolarized spherically-symmetric sheath screens the Coulomb field of the charged particulate that it surrounds (Debye shielding), it does *not* screen the particulate from an externally applied field.

The notion of a "dressed particle" is often used to explain phenomena concerning charged particles in plasmas (e.g, Ref. 7). This concept suggests that a charged particle and its oppositely-charged Debye sheath be regarded as a single "system," and serves as a convenient reminder that the electric field *due* to the particle is only of short range. However, one should be careful not to infer that the sheath also serves to shield the particulate from external fields. As shown in Sec. 2.3, the total dipole moment $\mathbf{P}$ of a "dressed particle," i.e., the system of a particulate and its sheath, is zero even in the presence of sheath polarization. One may

thus "formally" calculate the force on this dipole due to an external field as $\mathbf{F} = \nabla\mathbf{P}\cdot\mathbf{E}_0$, which is of course zero since $\mathbf{P} = \mathbf{0}$. Thus, this dipole force does not amount to the (total) force on the particle that we have derived above — contrary to what is postulated in Ref..[2]

One may also calculate the monopole moment — i.e., total charge — of a dressed particle, which is obviously zero since the total sheath charge is equal in magnitude but opposite in sign to that on the particle, regardless of whether or not the sheath is polarized. Thus, again, the "formal" force on the dressed particle is zero, which may be interpreted as perfect shielding of an external field by the sheath — i.e., the charged particle in a plasma does not move even in the presence of an external field, which again contradicts our earlier conclusions.

The source of this apparent contradiction is the misleading idea, suggested by the notion of a "dressed" particle, that the Debye sheath is somehow "permanently attached" to the particle (since the particle and sheath always move together). In fact, the Debye sheath is *not* attached to the particle. Even under the influence of an external electric field, ions and electrons in the sheath are in equilibrium under a balance between electrostatic forces (due to both the external and sheath fields) and plasma pressure forces (due to thermal motion). If the external field is increased, the plasma pressure also increases to compensate for it, maintaining a net charge (i.e., a sheath) around the particle. (Hence, it is important to take pressure forces into account, especially in the case of finite-radius particles, as was done in Sec. 2.4.)

This should not be taken to imply, however, that the sheath is "attached" to the particle through pressure forces, so that the electrostatic force on the sheath is somehow transmitted to the particle. The sheath represents only a local perturbation of the background plasma: if the particle moves from A to B, the plasma will relax to the unperturbed state about A and a new perturbation centered at B will arise. No net transport of matter is associated with such "movement" of the sheath. In other words, a dressed particle "undresses" and "dresses" each time it moves. Thus, the presence of the sheath has no effect on the particle dynamics

if the sheath is spherically symmetric: the only additional force arises from a *polarization* of the sheath. (If the particle velocity exceeds the ion thermal velocity, however, ions cannot "re-form" a sheath sufficiently rapidly around the instant position of the particle, resulting in an ion "wake." In this chapter we consider only the case of negligible plasma flows relative to the particle motion.)

2.7. Polarization forces in a glow discharge

As an application of the theory developed in Secs. 2.2–2.5, we shall estimate the magnitude of the polarization force given by the second term of Eq. (2.15) under conditions representative of glow discharges used in plasma processing applications. In such discharges, the region adjacent to the electrode sheath (i.e., the "dark space") is called the presheath, in which a weak electric field accelerates ions and electrons while maintaining local charge neutrality.

A steady-state fluid description of the presheath region may be given as

$$\frac{d}{dz}[nv_i(z)] = \nu_{\rm ion} n\,, \tag{2.34}$$

$$\frac{d}{dz}[nv_e(z)] = \nu_{\rm ion} n\,, \tag{2.35}$$

$$m_i v_i \frac{dv_i}{dz} = eE - m_i \nu_{\rm ion} v_i\,, \tag{2.36}$$

$$0 = -k_B T_e \frac{dn}{dz} - enE\,, \tag{2.37}$$

where $\nu_{\rm ion}$ is the electron-impact ionization rate. Equations (2.34) and (2.35) are continuity equations for ions and electrons, while Eqs. (2.36) and (2.37) are the corresponding momentum equations. We assume that the ion and electron flow velocities, $\mathbf{v}_i$ and $\mathbf{v}_e$, and the electric field $\mathbf{E}$ are in the z-direction (with magnitudes v_i, v_e, and E, respectively), that the electron temperature T_e is constant, and that charge neutrality holds approximately: $n = n_i \simeq n_e$. We also take ion charge $q = e$ and temperature $T_i \simeq 0$, and we set $m_e \simeq 0$ and assume that the ion-neutral and electron-neutral collision frequencies are negligibly small.

The small difference between ion and electron densities, $\delta n = n_i - n_e$, may be calculated from Poisson's equation

$$\varepsilon_0 \frac{dE}{dz} = e\delta n .$$

All variables in Eqs. (2.34)-(2.37) are macroscopic quantities and are assumed to depend only on z. The subscript 0 that was used to indicate background plasma quantities in previous sections is omitted for simplicity.

From Eqs. (2.34) and (2.35), we obtain $v_i = v_e = v$. Writing $E = -d\Psi/dz$, and using normalized variables

$$\phi = e\beta_e \Psi , \quad u = v/c_s , \quad \zeta = \nu_{\rm ion} z/c_s ,$$

$c_s = (k_B T_e/m_i)^{\frac{1}{2}}$ being the ion sound velocity, we rewrite Eqs. (2.34)-(2.37) as

$$\frac{d}{d\zeta}(nu) = n , \tag{2.38}$$

$$\frac{dn}{d\zeta} = n\frac{d\phi}{d\zeta} , \tag{2.39}$$

$$u\frac{du}{d\zeta} + u = -\frac{d\phi}{d\zeta} . \tag{2.40}$$

We also employ simple boundary conditions:

$$u = \Psi = 0, \quad n = \bar{n} \quad \text{at} \quad z = 0$$

$$v \le c_s \quad \text{(Bohm sheath criterion)} .$$

In this section, unlike the convention used in the previous sections, $z = 0$ represents the center of the glow discharge (*not* the position of the particle).

It is straightforward to show that Eqs. (2.38)-(2.40) are equivalent to

$$\frac{d\zeta}{du} = \frac{1-u^2}{1+u^2} ,$$

$$\frac{d\phi}{du} = -2\frac{u}{1+u^2}$$

on $0 \le u \le 1$, with $n = \bar{n}\exp\phi$. The solutions to these equations may be easily obtained as

$$\zeta = 2\arctan u - u , \tag{2.41}$$

$$\phi = -\log(1 + u^2) . \tag{2.42}$$

Figures 2.3 and 2.4 depict the profiles of density n, velocity v, field potential Ψ, and electric field E in the presheath region given by Eqs. (2.41) and (2.42). Here $L_0 = (\pi/2 - 1)c_s/\nu_{\rm ion}$ and $z = L_0$ is the boundary between the presheath and electrode sheath (i.e., dark space) in the discharge.

Using the density and electric field profiles in Figs. 2.3 and 2.4 for $n_{i0} = n_{e0}$ and E_0 in Eq. (2.15), where

$$k_D^2(z) = \left(\frac{q^2\beta_i}{\varepsilon_0} + \frac{e^2\beta_e}{\varepsilon_0}\right) n(z) ,$$

we may write the z-components of the external-field force and polarization force as

$$F_0(z) = -QE_0(z) = \frac{Q\nu_{\rm ion}}{e\beta_e c_s} f_0\left(\frac{z}{L_0}\right) ,$$

$$F_1(z) = \frac{\sigma(z)Q^2}{16\pi\varepsilon_0 k_D(z)} = \delta\frac{Q\nu_{\rm ion}}{e\beta_e c_s} f_1\left(\frac{z}{L_0}\right) ,$$

where $\sigma(z) = dk_D(z)^2/dz$ and

$$\delta = \frac{eQ\beta_e}{16\pi\varepsilon_0\bar{\lambda}_D}$$

with $\bar{\lambda}_D$ being the Debye length at the center of the discharge (i.e., $z = 0$). Clearly $f_0(z/L_0) = d\phi/d\zeta$ and $f_1(z/L_0) = \exp(\phi/2)d\phi/d\zeta$, where ϕ is evaluated as a function of $\zeta = (\pi/2 - 1)z/L_0$ from Eqs. (2.41) and (2.42).

Figure 2.5 shows f_0 (i.e., the force F_0 in the unit of $Q\nu_{\rm ion}/e\beta_e c_s$) and f_1 (i.e., the polarization force F_1 in the unit of $\delta Q\nu_{\rm ion}/e\beta_e c_s$) as functions of position in the presheath, as calculated from Eqs. (2.41) and (2.42). Note that the ratio of the polarization force F_1 to the external-field force F_0 is of order δ, i.e,

$$\frac{F_1}{F_0} \simeq \delta ,$$

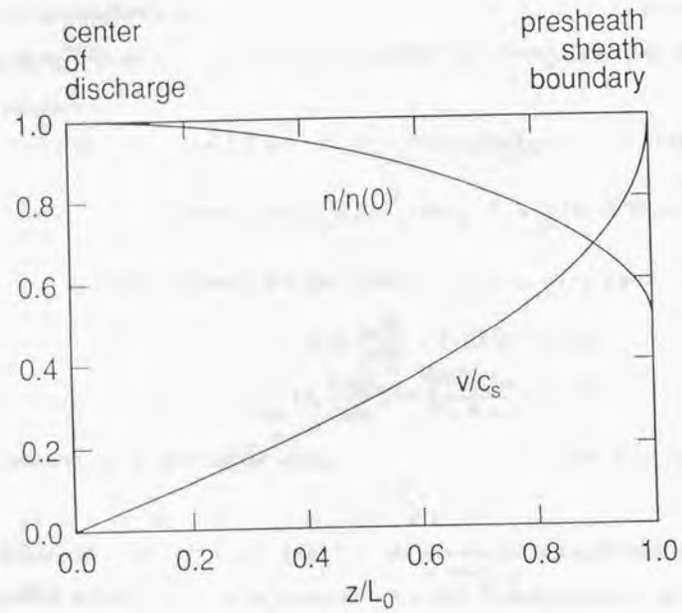

Figure 2.3: Profiles of density n and flow velocity v in the presheath region of a glow discharge obtained from Eqs. (2.41) and (2.42). The density is normalized by that at $z = 0$, i.e., $\bar{n} = n(0)$, and the flow velocity by the sound speed c_s. Here $z = 0$ is the center of the discharge and $z = L_0$ is the interface between the presheath and cathode sheath.

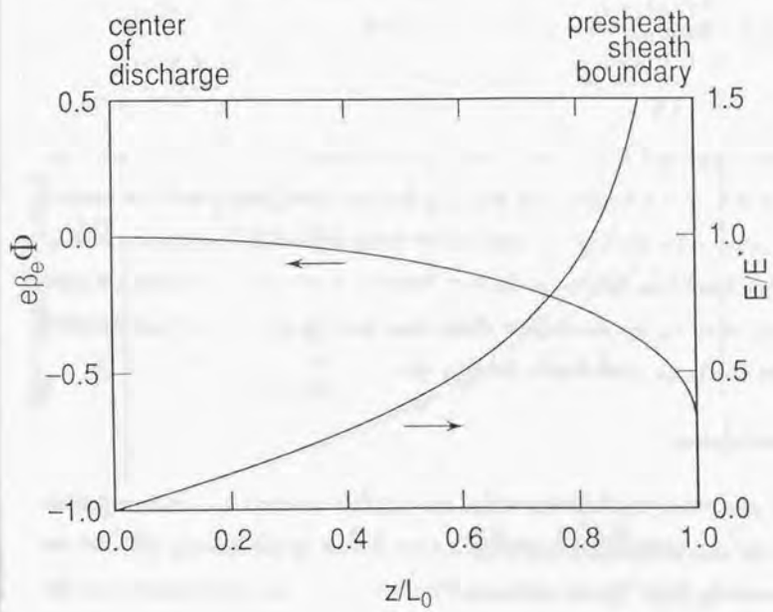

Figure 2.4: Profiles of the field potential Ψ (normalized by $1/e\beta_e$) and electric field E (normalized by $E^{\bullet} = \nu_{\rm ion}/e\beta_e c_s$) in the same presheath region as that of Fig. 2.3.

in the presheath. For a particulate of charge $Q = 1000e$ in a plasma with $T_i = 0.1\text{eV}$, $T_e = 1\text{eV}$, $n = 1 \times 10^{12}\text{cm}^{-3}$, this ratio becomes $\delta = 0.16$: the magnitude of the sheath polarization force F_1 is a fraction of the external-field force $F_0 = -QE_0$.

We note that the polarization force F_1 was derived under the assumption that the plasma flow v is negligible, whereas — as shown in Fig. 2.3 — the flow velocity in the presheath region can be large in reality, reaching the ion sound velocity c_s at the presheath–sheath boundary, $z = L_0$. In fact, it is clear from the mass conservation equations (2.34) and (2.35) that effects of the velocity gradient may not be negligible:

$$\frac{1}{n}\frac{dn}{dz} \sim \frac{1}{v}\frac{dv}{dz}.$$

In this section, therefore, we have simply estimated the magnitude of the force given by Eq. (2.15), without demonstrating that this is in fact one of the dominant forces exerted on the particulate in the presheath. Indeed, the finite ion flow velocity is known to exert a significant drag force in the direction of the flow. However, aside from this drag force, a more detailed study including the plasma flow effects shows that the force is well approximated by Eq. (2.15) even in the presence of a finite ion flow.

2.8. Discussion

We have shown that, if plasma flow effects are negligible, the total force on a particulate is given by the sum of the direct electrostatic force exerted by the external field and the sheath polarization force. For an infinitesimal particle, we obtained the expression for the total force given by Eq. (2.15), i.e.,

$$\mathbf{F} = -Q\mathbf{E}_0 - \frac{Q^2\nabla\lambda_D}{8\pi\varepsilon_0\lambda_D^2}, \tag{2.43}$$

where $\mathbf{E}_0$ and λ_D are evaluated at the particulate position. For a particle of small radius a, the force is given by Eq. (2.32). As seen in both Eqs. (2.15) and (2.32), the total force

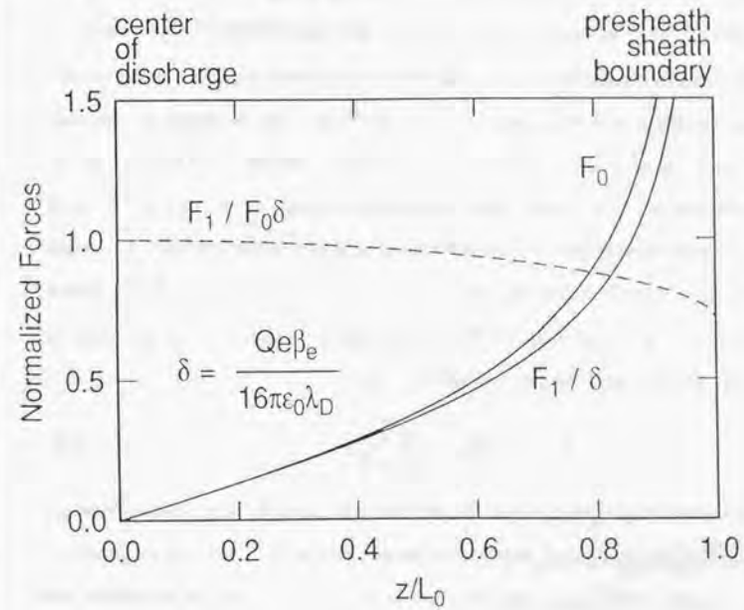

Figure 2.5: The external electrostatic force F_0 and the ratio of the polarization force F_1 to δ as functions of position in the presheath region of Figs. 2.3 and 2.4. The forces are normalized by $Q\nu_{\text{ion}}/e\beta_e c_s$.

on the charge $-Q$ is given exactly by $-Q\,\mathbf{E}_0$ in the case of uniform density (i.e., $\sigma = 0$). In other words, as one might expect, an unpolarized, perfectly spherical sheath does not mitigate the externally applied field at the particulate position. Only the polarization of the sheath modifies the external field — reducing or enhancing it, depending on the direction of the polarization force relative to that of the applied field. The polarization force is always in the direction of decreasing Debye length, regardless of the sign of the particulate charge or the direction of the applied field. In other words, the free energy of the system — given by Eqs. (2.16) and (2.33) — is smaller when the particulate has a thinner Debye sheath.

The presence of finite plasma flow may change the polarization force given by Eq. (2.43), beyond the obvious effect of a drag force on the particulate. As is shown in the next chapter, in the presence of a finite plasma flow, Eq. (2.43) is correct to $\mathcal{O}(v_{i0}^2/v_{th}^2)$, where v_{i0} and v_{th} denote the ion flow velocity and ion thermal velocity $v_{th} = (k_B T_i/m_i)^{\frac{1}{2}}$. It is also shown in the next chapter that, in the presence of a large ion flow velocity (e.g., when $v_i \simeq c_s = (k_B T_e/m_i)^{\frac{1}{2}}$, the ion sound velocity or Bohm velocity, near the presheath-sheath boundary given by $z = L_0$ in Sec. 2.7) the electrostatic and polarization forces are given by Eq. (2.43) except that one uses the *electron* Debye length:

$$\mathbf{F} = -Q\mathbf{E}_0 - \frac{Q^2 \nabla \lambda_e}{8\pi\varepsilon_0 \lambda_e^2}. \tag{2.44}$$

The physical reason for this is that, when the ion flow is sufficiently large compared to the ion thermal velocity (i.e., $v_{i0} \gg v_{th}$), ions cannot form a sheath and the sheath comprises a deficiency of electrons. In this case, ions are "blown away" by the fast ion mean flow and the ion density profile around the particulate becomes almost uniform. As is obvious from the discussion in Sec. 2.2, the constant ion density distribution [instead of Eq. (2.4)] results in the background Debye length given by the electron Debye length (i.e, $\lambda_D = \lambda_e$). In other words, the thickness of the sheath around a particulate is given by the electron Debye length λ_e in the presence of a large ion flow.

The total force on a single particulate is thus given by the sum of $\mathbf{F}$ above [either by Eq. (2.43) or Eq. (2.44) depending on whether the ion flow is small or large] *and* the ion drag force, i.e., the force due to Coulomb collisions between the flowing ions and the particulate. A complete expression for, and detailed discussion of, this drag force (as well as convenient approximate expressions) may be found in Ref. 3.

References

[1]S. Hamaguchi and R. T. Farouki, Phys. Rev. E **49**, 4430 (1994).

[2]A. Bouchoule, A. Plain, L. Boufendi, J. Ph. Blondeau, and C. Laure, J. Appl. Phys. **70**, 1991 (1991).

[3]T. G. Northrop and T. J. Birmingham, Planet. Space Sci. **38**, 319 (1990).

[4]B. A. Trubnikov, in *Review of Plasma Physics*, edited by M. A. Leontovich (Consultants Bureau, New York, 1965), Vol. 1, p. 205.

[5]S. Chandrasekhar *Principles of Stellar Dynamics*, Dover, New York (1960).

[6]L. Spitzer, Jr., *Physics of Fully Ionized Gases*, 2nd Ed., Interscience Publishers, New York (1962).

[7]N. A. Krall and A. W. Trivelpiece, *Principles of Plasma Physics*, MacGraw-Hill, New York (1973).

[8]J. Hubbard, Proc. Roy. Soc. A**260**, 114 (1961).

[9]T. Kihara and O. Aono, J. Phys. Soc. Japan**18**, 837 (1963).

Chapter 3

Particulate interactions with plasma flows

3.1. Introduction

In the preceding chapter, we have obtained an expression for the force on a particulate in the absence of plasma flows that includes components (i)-(iii) above. In this chapter, we extend our earlier study by investigating the plasma-particulate interaction in the presence of finite plasma flows.[1] Since the sizes of particulates that we are concerned with are sufficiently small compared to the Debye length of the background plasma, we consider only the case of infinitesimal particulates in this chapter. As in the preceding chapter, we shall use a fluid model for the plasma, and thus the ion drag force — which arises from diffusion of the ion distribution function in velocity space due to Coulomb collisions — must be obtained separately from kinetic theories. The main issue addressed here is the question of how the polarization force obtained in Chap. 2 is modified by the presence of finite plasma flows.

Since plasma flows will contribute to the deformation of Debye sheaths surrounding particulates, the polarization force is expected to be dependent on the flow velocity and/or flow-velocity gradients. Unlike the ion drag force, the deformation of the sheath due to a finite plasma flow may be well described by a fluid model of the plasma. Based on the fluid approximation presented in the following section, we shall discuss the plasma-particulate

interaction in detail and systematically derive an expression for the total force exerted on the particulate.

3.2. Fluid model of the plasma

Consider an unmagnetized plasma containing a particulate of negative charge $-Q$ ($Q > 0$) at position $\mathbf{r}_p$. Assuming the particulate is of negligible size on the macroscopic scale, we employ a fluid model for the plasma[2] defined by the following equations:

$$\partial_t n_i + \nabla\cdot(n_i\mathbf{v}_i) = S_i\,, \tag{3.1}$$

$$\partial_t n_e + \nabla\cdot(n_e\mathbf{v}_e) = S_e\,, \tag{3.2}$$

$$\begin{aligned} m_i n_i(\partial_t\mathbf{v}_i + \mathbf{v}_i\cdot\nabla\mathbf{v}_i) = & -k_B T_i\nabla n_i - q n_i\nabla\Phi \\ & -\nu_i m_i n_i\mathbf{v}_i - m_i S_i\mathbf{v}_i\,, \end{aligned} \tag{3.3}$$

$$\begin{aligned} m_e n_e(\partial_t\mathbf{v}_e + \mathbf{v}_e\cdot\nabla\mathbf{v}_e) = & -k_B T_e\nabla n_e + e n_e\nabla\Phi \\ & -\nu_e m_e n_e\mathbf{v}_e - m_e S_e\mathbf{v}_e\,, \end{aligned} \tag{3.4}$$

$$-\varepsilon_0\Delta\Phi = -Q\delta(\mathbf{r}-\mathbf{r}_p) + q n_i - e n_e\,, \tag{3.5}$$

where the subscripts i and e denote ion and electron quantities. Here n, $\mathbf{v}$, m, Φ, T, S, and ν represent density, flow velocity, mass, electric potential, temperature, particle source rate, and frequency of collisions with neutral species, respectively. Constant ion and electron temperatures are assumed, and ion and electron viscosities are neglected for the sake of simplicity.

In typical glow discharge or interstellar plasma environments, the sizes of particulates

and their Debye sheaths are small compared to the ion mean free path in the ambient plasma. For such systems, a fluid description of the plasma (the ions, especially) does not fully account for the interaction between a particulate and the background plasma. As noted in the previous section, for example, a fluid model cannot properly account for the ion drag force due to Coulomb scattering of ions by the charged particulate.

Recently, Northrop and Birmingham[3] have obtained the total interaction, including the ion drag force, between a microscopic dust grain and a *uniform* background plasma, based on the kinetic theories developed by Hubbard[4] and Kihara and Aono.[5] Because of the plasma uniformity, however, the polarization force vanishes in their system: the total interaction between a particulate and a uniform plasma is due to the ion drag force and "plasma collective effects" (which together may be considered to include pressure forces).

We are concerned here with non-uniform plasmas, for which a kinetic treatment of the system is substantially more complex, and thus the simpler system defined by Eqs. (3.1)-(3.5) is a reasonable alternative to study. As noted in the preceding section, deformations of the sheath due to density gradients and finite plasma flows are well described by this fluid model (which is a generalization of the model used in Chap. 2 to estimate the polarization force in the absence of plasma flows).

3.3. Equilibrium and electrostatic perturbation

We consider first a steady-state (i.e., $\partial_t = 0$), unperturbed, non-uniform plasma that contains no particulates. From Eqs. (3.1)-(3.5), the set of equations governing the equilibrium state is

$$\nabla\cdot(n_{i0}\mathbf{v}_{i0}) = S_i\,, \tag{3.6}$$

$$\nabla\cdot(n_{e0}\mathbf{v}_{e0}) = S_e\,, \tag{3.7}$$

$$m_i n_{i0} \mathbf{v}_{i0} \cdot \nabla \mathbf{v}_{i0} = -k_B T_{i0} \nabla n_{i0} - q n_{i0} \nabla \Phi_0 - \nu_i m_i n_{i0} \mathbf{v}_{i0} - m_i S_i \mathbf{v}_{i0} , \tag{3.8}$$

$$m_e n_{e0} \mathbf{v}_{e0} \cdot \nabla \mathbf{v}_{e0} = -k_B T_{e0} \nabla n_{e0} + e n_{e0} \nabla \Phi_0 - \nu_e m_e n_{e0} \mathbf{v}_{e0} - m_e S_e \mathbf{v}_{e0} , \tag{3.9}$$

$$-\varepsilon_0 \Delta \Phi_0 = q n_{i0} - e n_{e0} . \tag{3.10}$$

Here the subscript 0 denotes the unperturbed (i.e., equilibrium) state.

In this chapter, we are not directly concerned with solving Eqs. (3.6)–(3.10). Instead, we shall assume that an equilibrium plasma state satisfying these equations is given, and then determine how the introduction of a charged particulate perturbs the system. Denoting the perturbed density, potential, and flow velocity by $\tilde{n}$, ϕ, and $\tilde{\mathbf{v}}$, respectively, we may write $n = n_0 + \tilde{n}$, $\Phi = \Phi_0 + \phi$, and $\mathbf{v} = \mathbf{v}_0 + \tilde{\mathbf{v}}$. Assuming that these perturbations are small, we now linearize Eqs. (3.1)–(3.5) with respect to them.

From Eq. (3.3), for example, we obtain

$$m_i n_{i0} \partial_t \tilde{\mathbf{v}}_i + m_i n_{i0} [(\mathbf{v}_{i0} \cdot \nabla) \tilde{\mathbf{v}}_i + (\tilde{\mathbf{v}}_i \cdot \nabla) \mathbf{v}_{i0}] + m_i \tilde{n}_i (\mathbf{v}_{i0} \cdot \nabla) \mathbf{v}_{i0} = -k_B T_i \nabla \tilde{n}_i - q n_{i0} \nabla \phi - q \tilde{n}_i \nabla \Phi_0 - \nu_i m_i [n_{i0} \tilde{\mathbf{v}}_i + \tilde{n}_i \mathbf{v}_{i0}] .$$

Eliminating the term $(\mathbf{v}_{i0} \cdot \nabla) \mathbf{v}_{i0}$ from the above by using Eq. (3.8), we obtain Eq. (3.12) below. Similarly, from Eq. (3.4) and (3.9) with $m_e \to 0$, we obtain

$$-k_B T_e \nabla \left(\frac{\tilde{n}_e}{n_{e0}} \right) + e \nabla \phi = 0 .$$

Upon integration, this yields the Boltzmann relation for the electron density given by Eq. (3.14) below.

The linearized equations for the perturbed quantities are thus given by

$$\partial_t \tilde{n}_i + \nabla (n_{i0} \tilde{\mathbf{v}}_i + \tilde{n}_i \mathbf{v}_{i0}) = 0 , \tag{3.11}$$

$$m_i \partial_t \tilde{\mathbf{v}}_i = -\frac{1}{\beta_i} \nabla \left(\frac{\tilde{n}_i}{n_{i0}} \right) - q \nabla \phi + m_i [\mathbf{v}_{i0} \cdot \nabla \tilde{\mathbf{v}}_i + \tilde{\mathbf{v}}_i \cdot \nabla \mathbf{v}_{i0}] - \nu_i m_i \tilde{\mathbf{v}}_i , \tag{3.12}$$

$$-\varepsilon_0 \Delta \phi = -Q \delta(\mathbf{r} - \mathbf{r}_p) + q \tilde{n}_i - e \tilde{n}_e , \tag{3.13}$$

$$\tilde{n}_e = e \beta_e n_{e0} \phi . \tag{3.14}$$

Here $\beta_i = 1/k_B T_i$ and $\beta_e = 1/k_B T_e$. Note that the equation determining the electron flow velocity $\mathbf{v}_e$ is decoupled from the system (3.11)–(3.14).

In the case of zero ion flow velocity, Eq. (3.12) gives the Boltzmann relation $\tilde{n}_i = -q \beta_i n_{i0} \phi$ for the ions, and the system reduces to that discussed in Chap. 2. In other words, Eqs. (3.11)–(3.14), which include the effects of finite plasma flows, represent a generalization of the model used in Chap. 2.

3.4. Steady–state solutions

We now solve Eqs. (3.11)–(3.14) in a steady state to obtain the Debye sheath surrounding a particle under the influence of an external field Ψ_0, a density gradient ∇n_0, and an ion flow $\mathbf{v}_{i0}$. Since plasma perturbations due to the charged particulate are confined within a small volume (the Debye sheath), it is natural to assume that the spatial variations of perturbed quantities are much larger than those of the corresponding equilibrium quantities in the sense that, for example, $|\nabla \tilde{n}| \gg |\nabla n_0|$.

To make the system of equations more tractable, we select a local coordinate system by

setting $\mathbf{r}_p = \mathbf{0}$ and choosing the z–axis parallel to the direction of gradients of equilibrium quantities (we assume for simplicity that the ion flow velocity and the gradients of all equilibrium quantities, such as n_0, $\mathbf{v}_0$, and Ψ_0, are parallel). Then, to accuracy $\mathcal{O}(\delta)$, where $\delta = \lambda_D/L$ with L being a representative macroscopic scale (e.g., the density gradient scale $|\nabla \ln n_{i0}|^{-1}$), the equilibrium quantities in Eqs. (3.11)–(3.14) will depend only on z and are given by $n_{i0}(z) = n_{i0}(0) + n'_{i0}(0)z$, $\mathbf{v}_{i0}(z) = v_{i0}(z)\hat{\mathbf{z}} = [v_{i0}(0) + v'_{i0}(0)z]\hat{\mathbf{z}}, \ldots$ etc., where the primes denote derivatives with respect to z and $\hat{\mathbf{z}}$ is a unit vector in the z direction.

Using the following normalized variables

$$\boldsymbol{\rho} = \frac{\mathbf{r}}{\lambda_e}, \quad \zeta = \frac{z}{\lambda_e}, \quad \tilde{\nabla} = \lambda_e \nabla, \quad \mathbf{u} = \frac{\mathbf{v}_i}{v_{i,th}},$$

$$u_0 = \frac{v_{i0}}{v_{i,th}}, \quad u'_0 = \frac{\lambda_e v'_{i0}}{v_{i,th}}, \quad n = \frac{\tilde{n}_i}{n_{i0}(0)}, \quad \psi = q\beta_i\phi,$$

$$\mu = \frac{\lambda_e n'_{i0}(0)}{n_{i0}(0)}, \quad \mu_e = \frac{\lambda_e n'_{e0}(0)}{n_{e0}(0)}, \quad \alpha = \frac{\kappa_i^2}{\kappa_e^2}, \quad Q^* = -\frac{q\beta_i Q}{\varepsilon_0 \lambda_e},$$

where $\mathbf{r}$ is the position vector in the new local coordinate system, $v_{i,th} = (k_B T_i/m_i)^{1/2}$ is the ion thermal velocity, $\lambda_e = \kappa_e^{-1} = [\varepsilon_0/e^2\beta_e n_{e0}(0)]^{1/2}$ and $\kappa_i^{-1} = [\varepsilon_0/q^2\beta_i n_{i0}(0)]^{1/2}$ are the electron and ion Debye lengths evaluated at the particulate position $\mathbf{r} = \mathbf{0}$, we may rewrite Eqs. (3.11)–(3.13) in the steady state as

$$\tilde{\nabla}\cdot\mathbf{u} + u_0\frac{\partial n}{\partial \zeta} = -\mu\tilde{\nabla}\cdot(\zeta\mathbf{u}) - u'_0\frac{\partial}{\partial\zeta}(\zeta n), \tag{3.15}$$

$$\tilde{\nabla}n + \tilde{\nabla}\psi + u_0\frac{\partial}{\partial\zeta}\mathbf{u} = \mu n\hat{\mathbf{z}} - \mu\zeta\tilde{\nabla}\psi + (u'_0 + \mu u_0)\zeta\frac{\partial}{\partial\zeta}\mathbf{u} - u'_0 u_z\hat{\mathbf{z}} - \frac{\nu_i\lambda_e}{v_{i,th}}(1+\mu\zeta)\mathbf{u}, \tag{3.16}$$

$$\tilde{\Delta}\psi - \psi + \alpha n = -Q^*\delta(\boldsymbol{\rho}) + \mu_e\zeta\psi. \tag{3.17}$$

Here u_z is the z component of $\mathbf{u}$, and $\tilde{\Delta} = \tilde{\nabla}^2$ is the normalized Laplacian. Note that μ, μ_e, and u'_0 are $\mathcal{O}(\delta)$.

In the last term of Eq. (3.16), the coefficient is $\nu_i\lambda_e/v_{i,th} \simeq \lambda_e/\lambda_{mfp} \ll 1$, where λ_{mfp} denotes the mean free path for collisions between ions and neutral species (which is usually

large compared to the electron Debye length). In other words, the effects of collision between ions and neutral species may be ignored for dynamics on the scale of the Debye length. Thus, the last term of Eq. (3.16) (i.e., the term proportional to ν_i) will be dropped henceforth.

To solve Eqs. (3.15)–(3.17), we use the Fourier transformation defined by

$$\hat{f}(\mathbf{k}) = \int f(\boldsymbol{\rho})\exp(i\,\mathbf{k}\cdot\boldsymbol{\rho})\,d\boldsymbol{\rho},$$

where $f(\boldsymbol{\rho})$ is an arbitrary function and the integration is over all space. Note that under this transformation $\nabla f \to -i\mathbf{k}\hat{f}$, $\zeta f \to -i d\hat{f}/dk_z$, and $\delta(\boldsymbol{\rho}) \to 1$. The Fourier transformation of Eqs. (3.15)–(3.17) is then readily obtained as

$$\mathbf{k}\cdot\hat{\mathbf{u}} + u_0 k_z\hat{n} = i\mu\mathbf{k}\cdot\frac{d\hat{\mathbf{u}}}{dk_z} + iu'_0 k_z\frac{d\hat{n}}{dk_z}, \tag{3.18}$$

$$\mathbf{k}\hat{n} + \mathbf{k}\hat{\psi} + u_0 k_z\hat{\mathbf{u}} = i\mu\hat{n}\hat{\mathbf{z}} - iu'_0\hat{u}_z\hat{\mathbf{z}} + i\mu\frac{d}{dk_z}(\mathbf{k}\hat{\psi}) - i(u'_0 + \mu u_0)\frac{d}{dk_z}(k_z\hat{u}), \tag{3.19}$$

$$(k^2+1)\hat{\psi} - \alpha\hat{n} = Q^* + i\mu_e\frac{d}{dk_z}\hat{\psi}. \tag{3.20}$$

Since the system is symmetric about the z–axis, we may choose a unit vector $\hat{\mathbf{e}}_\perp$ orthogonal to $\hat{\mathbf{z}}$ such that $\mathbf{u} = u_\perp\hat{\mathbf{e}}_\perp + u_z\hat{\mathbf{z}}$ and $\mathbf{k} = k_\perp\hat{\mathbf{e}}_\perp + k_z\hat{\mathbf{z}}$. Equations (3.18)–(3.20) may then be written in matrix form as

$$M\boldsymbol{\xi} = iA_1\boldsymbol{\xi} + iA_2\frac{d}{dk_z}\boldsymbol{\xi} + \mathbf{b}, \tag{3.21}$$

where

$$\boldsymbol{\xi} = \begin{bmatrix} \hat{u}_\perp \\ \hat{u}_z \\ \hat{n} \\ \hat{\psi} \end{bmatrix} \quad \text{and} \quad \mathbf{b} = \begin{bmatrix} 0 \\ 0 \\ 0 \\ Q^* \end{bmatrix}.$$

Also

$$M = \begin{bmatrix} k_\perp & k_z & u_0 k_z & 0 \\ u_0 k_z & 0 & k_\perp & k_\perp \\ 0 & u_0 k_z & k_z & k_z \\ 0 & 0 & -\alpha & 1+k^2 \end{bmatrix},$$

$$A_1 = \begin{bmatrix} 0 & 0 & 0 & 0 \\ -(u_0' + \mu u_0) & 0 & 0 & 0 \\ 0 & -(2u_0' + \mu u_0) & \mu & \mu \\ 0 & 0 & 0 & 0 \end{bmatrix},$$

and

$$A_2 = \begin{bmatrix} \mu k_\perp & \mu k_z & u_0' k_z & 0 \\ -(u_0' + \mu u_0) k_z & 0 & 0 & \mu k_\perp \\ 0 & -(u_0' + \mu u_0) k_z & 0 & \mu k_z \\ 0 & 0 & 0 & \mu_e \end{bmatrix},$$

where $k = |\mathbf{k}|$. Note that each non-zero entry of A_1 and A_2 is $\mathcal{O}(\delta)$.

The solution to Eq. (3.21) may be given in the form $\boldsymbol{\xi} = \boldsymbol{\xi}^{(0)} + \boldsymbol{\xi}^{(1)}$, where $\boldsymbol{\xi}^{(0)} = \mathcal{O}(1)$ and $\boldsymbol{\xi}^{(1)} = \mathcal{O}(\delta)$. The 0th order solution $\boldsymbol{\xi}^{(0)}$ to Eq. (3.21) then evidently satisfies $M\boldsymbol{\xi}^{(0)} = \mathbf{b}$ or, from Eqs. (3.18)-(3.20),

$$\mathbf{k}\cdot\hat{\mathbf{u}}^{(0)} + u_0 k_z \hat{n}^{(0)} = 0\,, \tag{3.22}$$

$$\mathbf{k}\hat{n}^{(0)} + \mathbf{k}\hat{\psi}^{(0)} + u_0 k_z \hat{\mathbf{u}}^{(0)} = 0\,, \tag{3.23}$$

$$(k^2+1)\hat{\psi}^{(0)} - \alpha\hat{n}^{(0)} = Q^*\,. \tag{3.24}$$

Solving the above equations, we obtain the 0th order potential

$$\hat{\psi}^{(0)}(\mathbf{k}) = Q^* \left[k^2 + 1 + \frac{\alpha}{1 - u_0^2\cos^2\theta} \right]^{-1}, \tag{3.25}$$

where $\cos\theta = k_z/k$. In dimensional form, the equation above becomes

$$\frac{\lambda_e^2 \hat{\psi}^{(0)}(\mathbf{k})}{q\beta_i} = -\frac{Q}{\varepsilon_0}\left[\tilde{k}^2 + \kappa_e^2 + \frac{\kappa_i^2}{1 - u_0^2\cos^2\theta} \right]^{-1},$$

where $\tilde{k} = \kappa_e k$. Note that, when $u_0 < 1$, the ion Debye length $\lambda_i = \kappa_i^{-1}$ is effectively replaced by $\lambda_i(1 - u_0^2\cos^2\theta)^{\frac{1}{2}}$. Namely the sheath thickness around the particle is reduced most along the z axis (i.e., $\theta = 0$ and π).

In coordinate space, the sheath potential is given to lowest order by

$$\phi^{(0)}(\mathbf{r}) = \frac{1}{q\beta_i(2\pi)^3}\int \hat{\psi}^{(0)}(\mathbf{k})\exp(-i\mathbf{k}\cdot\mathbf{r}/\lambda_e)\,d\mathbf{k}\,. \tag{3.26}$$

In particular, if $u_0 \ll 1$, this potential becomes

$$\begin{aligned} \phi^{(0)}(\mathbf{r}) = & -\frac{Q}{4\pi\varepsilon_0 r}\exp(-\kappa_D r) \\ & + \frac{Q\kappa_i v_{i0}^2}{16\pi\varepsilon_0 v_{i,th}^2}\left[\left(1 - \frac{z^2}{r^2}\right)\exp(-\kappa_D r)\right. \\ & \left. - \frac{8}{\kappa_D^3 r^3}\left(1 - \frac{3z^2}{r^2}\right)\left\{1 - \exp(-\kappa_D r)\left(1 + \kappa_D r + \frac{1}{2}\kappa_D^2 r^2\right)\right\}\right], \end{aligned} \tag{3.27}$$

where $r = |\mathbf{r}|$ and $\kappa_D = (\kappa_i^2 + \kappa_e^2)^{\frac{1}{2}}$. The derivation of this expression is given in Appendix C. The first term of Eq. (3.27) represents the well-known screened Coulomb potential. Figure 3.1 illustrates Eq. (3.27) for $u_0^2 = (v_{i,0}/v_{i,th})^2 = 0.1$ and $\kappa_i/\kappa_D = 1$.

The force exerted on the particulate by the electrostatic field is given by

$$\begin{aligned} \mathbf{F} &= (-Q)\mathbf{E}|_{\mathbf{r}=\mathbf{0}} \\ &= Q\nabla\left(\phi(\mathbf{r}) - \frac{-Q}{4\pi\varepsilon_0 r}\right)\Big|_{\mathbf{r}=\mathbf{0}} - Q\mathbf{E}_0(\mathbf{0}) \qquad (3.28) \\ &= \frac{-iQ}{\lambda_e q\beta_i(2\pi)^3}\int d\mathbf{k}\,\mathbf{k}\left[\hat{\psi}(\mathbf{k}) + \frac{Q}{\varepsilon_0 k^2}\right] - Q\mathbf{E}_0(\mathbf{0})\,. \qquad (3.29) \end{aligned}$$

The term $-Q/4\pi\varepsilon_0 r$ in Eq. (3.28) represents the self-energy of the particulate, which must be subtracted out in the force calculation. Note that the Fourier transform of $1/4\pi\rho$ is $1/k^2$.

By substituting Eq. (3.25) into Eq. (3.29), we find that the force $\mathbf{F}^{\mathrm{p}} = \mathbf{F} + Q\mathbf{E}_0(\mathbf{0})$ due to the lowest-order sheath field potential $\phi^{(0)}(\mathbf{r})$ vanishes, i.e., $\mathbf{F}^{\mathrm{p}} = \mathbf{0}$, since the integral over the polar angle θ vanishes. Indeed, as may be easily seen from Eq. (3.26), the lowest-order sheath potential $\phi^{(0)}$ is symmetric about the x-y plane — $\phi^{(0)}(\mathbf{r})$ is invariant under the map $z \to -z$. In other words, the Debye sheath does *not* become polarized in the presence of a uniform ion flow $\mathbf{v}_{i0}$, although the sheath may be somewhat squeezed in the z direction, as depicted in Fig. 3.1. No charge separation is associated with this symmetric deformation of

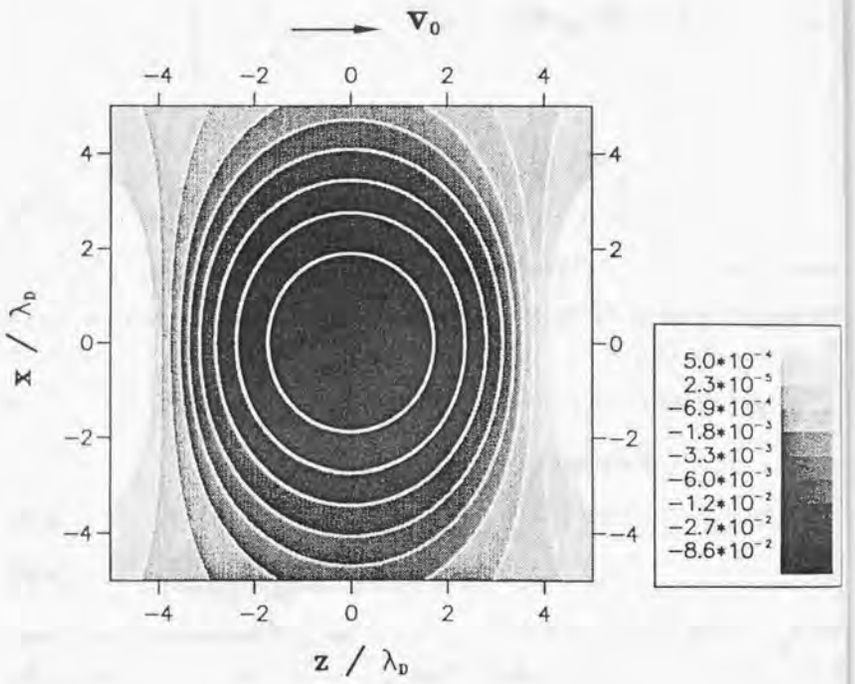

Figure 3.1: The potential contours around an infinitesimal particle (located at the origin) obtained from Eq. (3.27). Here $u_0^2 = 0.1$ and $\kappa_D = \kappa_s$ are assumed. The potential is normalized by $Q\kappa_D/a\pi\varepsilon_0$. Note that the contours are on a logarithmic scale.

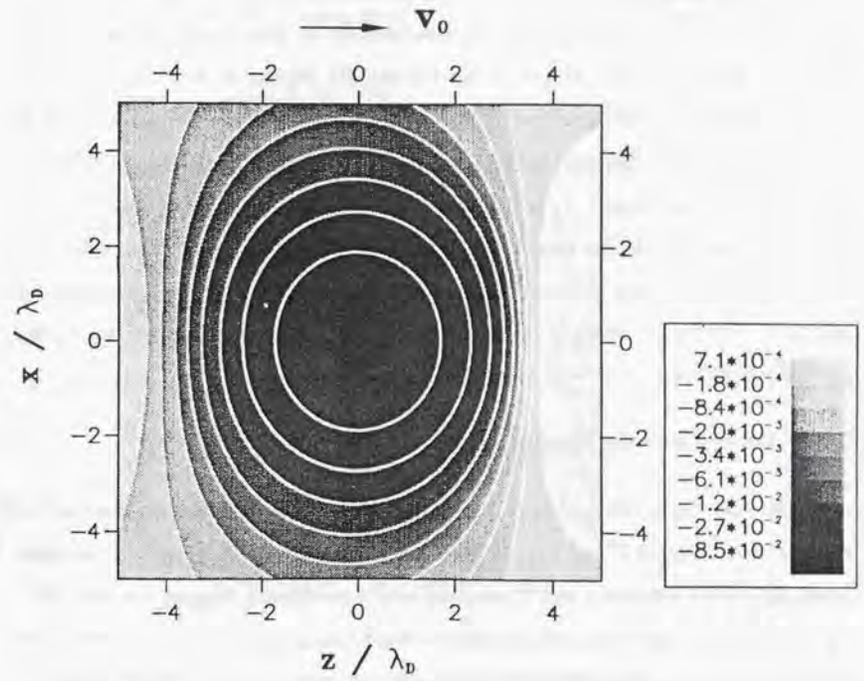

Figure 3.2: The total potential $\phi^{(0)}+\phi^{(1)}$ obtained from Eqs. (3.27) and (3.36). To emphasize the ion flow effects, we have assumed $\sigma = 0$ and $v'_{i,0} = v_{i,0}/L > 0$ with $\lambda_D/L = 0.3$. The other parameters are the same as those in Fig. 3.1. Note that the contours are on a logarithmic scale.

the Debye sheath, and thus no net electrostatic force is exerted on the particulate. The first term $\mathbf{F}^{\mathrm{P}}$ of Eq. (3.29) may be called a polarization force, since it becomes non-zero only when there is a charge separation (i.e., polarization) of the sheath surrounding the particulate.

Uniform ion flows thus exert no net force on particulates in the fluid approximation. In kinetic treatments, however, Coulomb collisions between the flowing ions and particulates cause an asymmetry in the ion distribution function and give rise to a non-zero ion drag force.[6] (The situation here is somewhat different from the well-known d'Alembert paradox in fluid dynamics, which states that two-dimensional, incompressible, irrotational, inviscid flows exert no drag forces.) In our fluid model, although the size of the particulate is infinitesimal, we nevertheless assume that it is a "small" macroscopic object immersed in the plasma. Under such conditions, the force due to the non-uniformity of the background plasma — such as the polarization force — becomes the dominant force exerted on the particulate. We therefore proceed to higher-order calculations.

3.5. Forces due to plasma non-uniformity

As shown in the previous section, the effects of plasma non-uniformity are contained in the first order solution $\boldsymbol{\xi}^{(1)}$ to Eq. (3.21) — a uniform plasma with finite flows, as represented by the 0th order solution $\boldsymbol{\xi}^{(0)}$, does not exert a polarization force on the particulate. Therefore, we now solve Eq. (3.21) to $O(\delta)$ to obtain the non-zero polarization force. The algebraic manipulations in this section were mostly performed using the AXIOM system.[7]

By solving $M\boldsymbol{\xi}^{(0)} = \mathbf{b}$, or Eqs. (3.22)-(3.24), we obtain

$$\boldsymbol{\xi}^{(0)} = \frac{1}{P}\begin{bmatrix} k_\perp k_z u_0 \\ k_z^2 u_0 \\ k^2 \\ k_z^2 u_0^2 - k^2 \end{bmatrix}, \tag{3.30}$$

where

$$P = -(1+k^2)(k^2 - k_z^2 u_0^2) - \alpha k^2.$$

Then, from Eq. (3.21), the first-order solution $\boldsymbol{\xi}^{(1)}$ satisfies

$$M\boldsymbol{\xi}^{(1)} = iA_1\boldsymbol{\xi}^{(0)} + iA_2\frac{d}{dk_z}\boldsymbol{\xi}^{(0)}.$$

Substituting Eq. (3.30) into the equation above and inverting the matrix M, we readily obtain the solution $\boldsymbol{\xi}^{(1)}$.

In particular, the first-order potential perturbation may be given as

$$\tilde{\psi}^{(1)}(\mathbf{k}) = iQ^{*}\frac{\mu\tilde{\psi}_\mu + \mu_e\tilde{\psi}_{\mu e} + u_0'\tilde{\psi}_u}{\{[k_z^4 + (k_\perp^2+1)k_z^2]u_0^2 - k^2(k^2+\alpha+1)\}^3}, \tag{3.31}$$

where

$$\begin{aligned}\tilde{\psi}_\mu =& 2\alpha k_z k^6 \\ &-\alpha k_z k^2\left[6k_z^4 + (3k_\perp^2 - 2\alpha - 2)k_z^2 - 3k_\perp^4 - (5\alpha+3)k_\perp^2\right]u_0^2 \\ &+\alpha k_z^3\left[4k_z^4 + (5k_\perp^2 - 2)k_z^2 + k_\perp^4 + k_\perp^2\right]u_0^4,\end{aligned} \tag{3.32}$$

$$\begin{aligned}\tilde{\psi}_{\mu e} =& 2k_z k^6 \\ &-2k_z k^2(3k_z^4 + 3k_\perp^2 k_z^2 - \alpha k_\perp^2)u_0^2 \\ &+2k_z^3(3k_z^4 + 3k_\perp^2 k_z^2 - \alpha k_\perp^2)u_0^4 \\ &-2k_z^7 u_0^6,\end{aligned} \tag{3.33}$$

$$\begin{aligned}\tilde{\psi}_u =& 2\alpha k_z k^4(k^2+\alpha+1)u_0 \\ &-2\alpha k_z^3 k^2(k^2+1)u_0^3.\end{aligned} \tag{3.34}$$

It is neither easy nor practical to use the full solution for $\tilde{\psi}^{(1)}(\mathbf{k})$ given by Eqs. (3.31)-(3.34) to estimate the polarization force. Instead we shall consider two important limiting cases, in which the expression for the polarization force provides clearer physical insight and concise formulae that may be used in macroscopic (e.g., fluid or particle-in-cell) simulations to determine overall particulate transport characteristics in the plasma.

3.6. Small flow limit

In order to elucidate the relation between the complete solution obtained in the preceding section and that given in Chap. 2, we first take the limit of a small ion flow (i.e., $u_0 \ll 1$) in Eq. (3.31):

$$\hat{\psi}^{(1)}(\mathbf{k}) = -iQ^* \left[\frac{2(\alpha\mu + \mu_e)k_z}{(k^2+\alpha+1)^3} + u_0' u_0 \frac{2\alpha k_z}{k^2(k^2+\alpha+1)^2} + \mathcal{O}(u_0^2) \right]. \tag{3.35}$$

Here we have assumed that $\delta = \lambda_D/L \simeq u_0 \ll 1$ and $u_0' = \mathcal{O}(\delta)$, rather than $u_0' = \mathcal{O}(\delta u_0)$ (i.e., the ion flow velocity is assumed to have a steep gradient near the particle), to clarify the effects of the ion flow gradient. Note that $\alpha\mu + \mu_e = \mathcal{O}(\delta)$.

The inverse Fourier transform of Eq. (3.35) yields

$$\begin{aligned}
\phi^{(1)}(\mathbf{r}) =& \frac{1}{q\beta_i}\psi^{(1)}(\mathbf{r}) \\
=& \frac{1}{q\beta_i(2\pi)^3}\int \hat{\psi}^{(1)}(\mathbf{k})\exp(-i\mathbf{k}\cdot\mathbf{r}/\lambda_e)\,d\mathbf{k} \\
=& \frac{Q\sigma z}{16\pi\varepsilon_0\kappa_D}\exp(-\kappa_D r) \\
&+ \frac{v_{i,0}v_{i,0}'\kappa_i^2 Q z}{2\pi v_{i,th}^2\kappa_D^4 r^3}\left[1-\exp(-\kappa_D r)\left(1+\kappa_D r+\frac{1}{2}\kappa_D^2 r^2\right)\right],
\end{aligned} \tag{3.36}$$

where $\kappa_D = (\kappa_i^2+\kappa_e^2)^{1/2}$ as before, and $\sigma = d\kappa_D^2(z)/dz$. Details of the above calculation are given in Appendix C. The first term in Eq. (3.36) represents the potential perturbation due to the density gradient (i.e., the gradient of the Debye length $\lambda_D = \kappa_D^{-1}$), while the second is due to the gradient of the ion flow velocity. Hence, polarizations of the Debye sheath represented by the first and second terms of Eq. (3.36) may be called the density-gradient and ion-flow-gradient polarizations, respectively. In the case of zero ion flow or flow gradient, Eq. (3.36) evidently reduces to the first-order potential perturbation given in Chap. 2.

Figure 3.2 shows the total potential (except for that of the applied electric field $\mathbf{E}_0$), i.e., $\phi^{(0)} + \phi^{(1)}$, derived from Eqs. (3.27) and (3.36). The particle is located at the origin. To

emphasize the ion flow effects, we have assumed $\sigma = 0$ and $v_{i,0}' = v_{i,0}/L > 0$ with $\lambda_D/L = 0.3$. The other parameters are the same as those in Fig. 3.1. Note that, since $v_{i,0}' > 0$ (and thus $v_{i,0}$ is larger in the region $z > 0$ than in $z < 0$), the sheath thickness is smaller for $z > 0$ than for $z < 0$.

As remarked in Sec. 3.4, the 0th order solution $\hat{\psi}^{(0)}(\mathbf{k})$ does not contribute to the polarization force. Therefore, from Eq. (3.29), the z component of the polarization force $\mathbf{F}^{\mathrm{P}}$ may be obtained from

$$\begin{aligned}
F_z^{\mathrm{P}} =& \frac{-iQ}{\lambda_e q\beta_i(2\pi)^3}\int k_z\hat{\psi}^{(1)}(\mathbf{k})\,d\mathbf{k} \\
=& \frac{\sigma Q^2}{16\pi\varepsilon_0\kappa_D}\left[1+\mathcal{O}(\varepsilon^2)\right] + \frac{v_{i0}v_{i0}'}{v_{i,th}^2}\frac{Q^2\kappa_i^2}{12\pi\varepsilon_0\kappa_D}\left[1+\mathcal{O}(\varepsilon^2)\right],
\end{aligned} \tag{3.37}$$

where $\varepsilon = u_0 = v_{i0}/v_{i,th}$ (the derivation of Eq. (3.37) is given in Appendix C). As in Eq. (3.36), the first and second terms of Eq. (3.37) represent the density-gradient and ion-flow-gradient polarization forces, respectively. Again, in the case $\varepsilon = 0$, the above polarization force agrees with that given in Chap. 2.

To obtain the total force, one needs to consider also the contribution of pressure forces. As in Chap. 2, however, a direct calculation of the plasma pressure shows that the pressure force on an infinitesimal particle is zero. Therefore, aside from the ion drag force that needs to be obtained from kinetic theories, the total force $\mathbf{F}$ is given by the sum of the direct electrostatic force $(-Q)\mathbf{E}_0$ and the polarization force given by Eq. (3.37). In vector form, we may write

$$\begin{aligned}
\mathbf{F} =& -Q\mathbf{E}_0 - \frac{\nabla\lambda_D}{\lambda_D^2}\frac{Q^2}{8\pi\varepsilon_0}\left[1+\mathcal{O}(\varepsilon^2)\right] \\
&+ \frac{\nabla|\mathbf{v}_{i0}|^2}{v_{i,th}^2}\frac{Q^2\lambda_D}{24\pi\varepsilon_0\lambda_i^2}\left[1+\mathcal{O}(\varepsilon^2)\right].
\end{aligned} \tag{3.38}$$

Here we have used $\sigma = -2\lambda_D^{-3}d\lambda_D/dz$. Note that, in Eq. (3.38), all plasma quantities are evaluated at the position of the particulate.

Under typical plasma flow conditions, the flow velocity gradient v'_{i0} is expected to be of order v_{i0}/L (where L is the macroscopic length scale), rather than $v'_{i0} = v_{i0}/\lambda_D$ as assumed above. In this case $u'_0 = \mathcal{O}(\delta\varepsilon)$, where $\delta = \lambda_D/L$ and $\varepsilon = v_{i0}/v_{i,th}$, and therefore $|\nabla\lambda_D| = \mathcal{O}(\delta)$ and $\lambda_D|\nabla \mathbf{v}^2_{i,0}|/\mathbf{v}^2_{i,th} = \mathcal{O}(\delta\varepsilon^2)$. Then Eq. (3.38) may be written as

$$\mathbf{F} = -Q\mathbf{E}_0 - \frac{Q^2}{8\pi\varepsilon_0}\frac{\nabla\lambda_D}{\lambda_D^2} + \mathcal{O}(\delta\varepsilon^2), \tag{3.39}$$

where the first two terms are the same as the total force obtained in Chap. 2. In other words, if the ion flow velocity is small compared to the ion thermal velocity, the ion-flow-gradient polarization force is $\mathcal{O}(\delta\varepsilon^2)$ whereas the density polarization force is $\mathcal{O}(\delta)$. The force expression given by the first two terms of Eq. (3.39) is therefore a good approximation for a non-uniform plasma with small ion flows.

3.7. Large flow limit

In typical glow discharges used in industrial applications, particulates become "trapped" at the plasma-sheath boundary — i.e., the boundary between the bulk plasma and the sheath adjacent to the electrode, as we discussed in the preceding chapter. Ions in the presheath region are accelerated toward the plasma-sheath boundary and the ion flow velocity v_{i0} reaches the sound (or Bohm) velocity $c_s = (k_B T_e/m_i)^{1/2}$. Since $T_e \gg T_i$ under typical conditions, the ion flow velocity exceeds the ion thermal velocity, i.e., $v_{i0} \simeq c_s \gg v_{i,th}$.

In the large ion flow limit we set $u_0 \gg 1$ in Eqs. (3.31)–(3.34) and retain only the lowest-order terms in the expansion parameter $1/u_0$. This gives

$$\tilde{\phi}^{(1)}(\mathbf{k}) = -2iQ^*\mu_e\frac{k_z}{(k^2+1)^3} + \mathcal{O}\left(\frac{\delta}{u_0^2}\right), \tag{3.40}$$

where $\mu_e = \mathcal{O}(\delta)$. Note that the lowest-order term is independent of u_0.

As in Eq. (3.36), the inverse Fourier transform of Eq. (3.40) gives the potential $\phi^{(1)}$, to

lowest order, as

$$\phi^{(1)}(\mathbf{r}) = \frac{Q\sigma_e z}{16\pi\varepsilon_0\kappa_e}\exp(-\kappa_e r),$$

where $\sigma_e = -2\lambda_e^{-3}d\lambda_e/dz$. As in Eq. (3.37), the z component of the polarization force may be obtained from Eq. (3.40). To lowest order, we have

$$F_z^p = \frac{\sigma_e Q^2}{16\pi\varepsilon_0\kappa_e}.$$

Since the pressure force is zero for an infinitesimal particulate, the total force in the presence of a large ion flow may be written in vector form as

$$\mathbf{F} = -Q\mathbf{E}_0 - \frac{Q^2}{8\pi\varepsilon_0}\frac{\nabla\lambda_e}{\lambda_e^2} + \mathcal{O}(\varepsilon^{*2}), \tag{3.41}$$

where $\varepsilon^* = 1/u_0 = v_{i,th}/v_{i0}$. Note again that, in the limit of strong ion flows, the ion-flow-gradient polarization force vanishes to lowest order.

Comparing expressions (3.39) and (3.41) for the opposite limits of small and large ion flows, we see that they differ only in the Debye length that is used: in the small-flow limit, λ_D is used, whereas λ_e is appropriate to the large-flow limit. This reflects the fact that, in the absence of ion flows, the size of the Debye sheath surrounding a particulate is given by the "characteristic" Debye length $\lambda_D = (1/\lambda_i^2 + 1/\lambda_e^2)^{-1/2}$, while in the presence of large ion flows it is given by just the electron Debye length λ_e.

The physical reason for this is that when the ion flow is large compared to the ion thermal velocity (i.e., $v_{i0} \gg v_{i,th}$), ions cannot form a sheath, and the sheath comprises a deficiency of electrons. In this case, the ions are "blown away" by the fast ion flow, and the ion density profile around the particulate becomes almost uniform. In typical glow discharges, however, plasma flow velocities are generally small compared to the *electron* thermal velocity $v_{e,th} = (k_B T_e/m_e)^{1/2}$, so that the electron sheath, of dimension λ_e, is hardly affected by the plasma flow.

3.8. Concluding remarks

In this chapter we have extended the results of the preceding chapter to obtain the total force $\mathbf{F}$ exerted on a charged particulate in a non-uniform plasma under the influence of finite ion flows. We have rigorously demonstrated, in the context of a fluid approximation of the plasma, that the expression for the polarization force given in Chap. 2 is a good approximation unless the ion flow velocity is comparable to the ion thermal velocity.

From Eqs. (3.41) and (3.39) we may write the total force on a particulate as

$$\mathbf{F} = -Q\mathbf{E}_0 - \frac{Q^2}{8\pi\varepsilon_0}\frac{\nabla\lambda}{\lambda^2} + (\text{ion drag force}), \tag{3.42}$$

where λ represents the thickness of the Debye sheath around the particulate. The first term is the electrostatic force on the particulate charge $-Q$ exerted by the external electric field $\mathbf{E}_0$, while the second term is the polarization force, i.e., the force due to the polarized Debye sheath. Note that $\mathbf{E}_0$ and λ in Eq. (3.42) are to be evaluated at the particulate position.

In the fluid approximation, polarization of Debye sheaths may be caused by density gradients and/or ion flow gradients. As discussed in Secs. 3.6 and 3.7, however, the ion-flow-gradient polarization force is typically small and may be neglected to lowest order, as shown in Eq. (3.42).

If the ion flow velocity is small compared to the ion thermal velocity, i.e., $v_{i0} \ll v_{i,th}$, the sheath thickness is given by the characteristic Debye length $\lambda_D = (1/\lambda_i^2 + 1/\lambda_e^2)^{-1/2}$, and λ_D should be used for λ in Eq. (3.42). Note that if $T_e \gg T_i$ (as is the case in typical glow discharges), we have $\lambda_D \simeq \lambda_i$.

On the other hand, if the ion flow velocity is large compared to the ion thermal velocity, i.e., $v_{i0} \gg v_{i,th}$, the sheath thickness is given by the electron Debye length λ_e. In this case, the ion density profile around the particulate is almost uniform, and the sheath comprises only a deficiency of electrons. The conditions for such fast ion flows arise when particulates

are trapped (due to a balance between electrostatic forces and drag forces) at the plasma-sheath boundaries of glow discharges, where the ion flow velocity equals the sound speed c_s. Under such conditions, λ_e should be used for λ in Eq. (3.42).

Strictly speaking, Eq. (3.42) holds only in these two limiting cases. For intermediate values of v_{i0}, as is clear from Eq. (3.38), the contribution from the ion flow gradient to the polarization force may be comparable to that from the density gradient. A more accurate evaluation of the total force at arbitrary v_{i0} may be obtained by performing the integration (3.29) numerically, using the complete expression for $\tilde{\psi}^{(1)}(\mathbf{k})$ (which is valid for any $v_{i,0}$) given by Eqs. (3.31)–(3.34).

Note also that, as indicated in Eqs. (3.39) and (3.41), the errors incurred by using Eq. (3.42) in the two limiting cases are only of second order, i.e., $\mathcal{O}(v_{i0}^2/v_{i,th}^2)$ for $v_{i0} \ll v_{i,th}$ and $\mathcal{O}(v_{i,th}^2/v_{i0}^2)$ for $v_{i,th} \ll v_{i0}$. (The ion-flow-gradient polarization force is represented explicitly by the third term of Eq. (3.38) when the ion flow is relatively small.)

It is interesting to note that, regardless of the sign of the particulate charge, the polarization force is always in the direction of decreasing Debye length. From Eq. (3.42), we may calculate the (Helmholtz) free energy $F_H = -\int^z F_z\,dz$ (neglecting the ion drag force) as

$$F_H = -Q\Psi_0 - \frac{Q^2}{8\pi\varepsilon_0\lambda}.$$

It is evident from this expression that the particulate has a lower free energy when it has a thinner Debye sheath (i.e., smaller λ).

As noted in Sec. 3.2, in most particulate systems observed in laboratory or space plasmas, the sizes of the particulates and their Debye sheaths are small compared to the ion mean free path for the background plasma. Therefore the fluid approximation that we have employed here is not strictly valid, especially when it is applied to phenomena that involve significant variation of the ion distribution function. The most important aspect of such kinetic effects is the ion drag force, which needs to be obtained separately from kinetic calculations and

added to the fluid force, as indicated in Eq. (3.42).

As shown in Sec. 3.4, the drag force for an infinitesimal particulate vanishes in the fluid approximation. However, the polarization force, with which we have been concerned, is well described by the fluid model. Although a systematic kinetic treatment of non-uniform plasmas is rather formidable, the question of whether such kinetic effects substantially modify the polarization force obtained from the fluid approximation deserves attention.

For expressions of the ion drag force, the reader is referred to Ref. 3, where large-angle Coulomb scattering,[8] dynamical friction,[9,10] and collective effects[6] are treated systematically. (In this treatment, however, the background plasma is assumed uniform, so the effects of external fields and density gradients are excluded. Thus, to obtain the total force in a non-uniform plasma, one needs to add the first two terms of Eq. (3.42), which represent the external electrostatic force and polarization force, to the drag force — assuming that such a superposition is a valid approximation.) The final expression obtained in this manner, which is a function of local plasma conditions such as the electric field, plasma density gradients, etc., may be used in conjunction with macroscopic simulations to determine the overall particulate transport characteristics in a discharge.

References

[1]S. Hamaguchi and R. T. Farouki, Phys. Plasmas **1**, 2110 (1994).

[2]S. I. Braginskii, in *Review of Plasma Physics* edited by M. A. Leontovich, (Consultants Bureau, New York, 1965), Vol. 1, p. 205.

[3]T. G. Northrop and T. J. Birmingham, Planet. Space Sci. **38**, 319 (1990).

[4]J. Hubbard, Proc. Roy. Soc. A**260**, 114 (1961).

[5]T. Kihara and O. Aono, J. Phys. Soc. Japan**18**, 837 (1963).

[6]N. A. Krall and A. W. Trivelpiece, *Principles of Plasma Physics*, (McGraw-Hill, New York, 1973).

[7]R. D. Jenks and R. S. Sutor, *AXIOM: the Scientific Computation System*, (Springer, New York, 1992).

[8]B. A. Trubnikov, in *Review of Plasma Physics* edited by M. A. Leontovich, (Consultants Bureau, New York, 1965), Vol. 1, p. 105.

[9]S. Chandrasekhar, *Principles of Stellar Dynamics*, (Dover, New York, 1960).

[10]L. Spitzer, Jr., *Physics of Fully Ionized Gases*, 2nd Ed., (Interscience Publishers, New York, 1962).

Chapter 4

Excess energy of Yukawa systems

4.1. Introduction

In the present and next chapters, we investigate the behavior of strongly interacting charged dust particles immersed in a plasma.[1] To model such a system, we consider an idealized model comprising N identical point charges (representing the particulates) immersed in a "smooth" (i.e., statistically-averaged) neutralizing background medium. This background may be a mixture of different media, each assumed to be in thermal equilibrium at a given temperature. For the sake of simplicity, we shall not consider non-equilibrium effects of the background plasma (such as plasma and neutral flows, ambient electric fields, etc.) on the strongly-coupled charged particle system.

As we have discussed earlier, the electric potential at position $\mathbf{r}$ in this system is given by the Yukawa (i.e., screened Coulomb) potential $\phi(\mathbf{r}) = -(Q/4\pi\varepsilon_0 r)\exp(-k_D r)$, where $r = |\mathbf{r}|$ and k_D^{-1} is the characteristic Debye length for the background medium, if a point charge $-Q$ is located at $\mathbf{r} = 0$ and the effect of all other point charges is ignored. This represents a linearized solution (the Debye–Hückel approximation) of the Poisson–Boltzmann system. There have been several Monte Carlo (MC) and molecular-dynamics (MD) simulations of "Yukawa systems," i.e., systems of particles that interact through a pair potential given by the Yukawa form or some variant thereof (e.g., Refs. 2–5).

These earlier studies, however, do not take proper account of the energy due to the charged background medium in the analysis of simulation data. The contribution of the background to the total energy becomes particularly important when one evaluates thermodynamical quantities from MC or MD simulations in the weak screening limit. As will be explained in detail later, the total Yukawa-system potential energy diverges in the weak screening limit. To obtain physical quantities in such a case, one must therefore subtract the correct infinite energy due to the background charge from the total Yukawa potential energy.

In the next chapter, we present MD simulations for Yukawa systems in both the weakly- and strongly-screened regimes.[6-8] If the screening vanishes completely, the system is called the one-component plasma (OCP).[9-16] In this chapter, we derive an expression for the total excess energy of Yukawa systems that converges to that of the OCP system. This expression is used to calculate various thermodynamical quantities in the next chapter. In the derivation of the excess energy, we employ full periodic boundary conditions (which are also used in the MD simulations presented in the next chapter) and establish the correct relation between the Yukawa pair potential and the Ewald potential used for the OCP system.

As we discussed earlier, the dust grains are negatively charged due to the high electron mobility, and surrounded by Debye sheaths of radius comparable to the Debye length k_D^{-1}. If the plasma consists of electrons and a single species of ions, the characteristic Debye length is related to the ion and electron Debye lengths λ_i and λ_e by $k_D^{-1} = (1/\lambda_i^2 + 1/\lambda_e^2)^{-1/2}$. In low-density discharge plasmas, the electron temperature T_e is typically much higher than the ion temperature T_i, so that $\lambda_i \ll \lambda_e$ and $k_D \approx \lambda_i^{-1}$.

If the Yukawa particulate system is in thermodynamic equilibrium, it may be characterized in terms of two dimensionless parameters[6,17]: the ratio $\kappa = k_D a$ of the inter-particulate distance $a = (3/4\pi n)^{1/3}$ (where n is the particulate density) to the screening length k_D^{-1}, and

the normalized inverse temperature

$$\Gamma = \frac{Q^2}{4\pi\varepsilon_0 a k_B T}. \tag{4.1}$$

Γ represents the Coulomb energy of a pair of particulates measured in units $k_B T$, although the real pair potential energy is smaller by factor $\exp(-\kappa)$ due to the Debye shielding. (Note that in some earlier work, e.g., Refs. 5,6,17, the quantity

$$\Gamma^* = \frac{Q^2 \exp(-\kappa)}{4\pi\varepsilon_0 a k_B T}$$

is used instead of Eq. (4.1). In the next chapter, however, Γ as defined by Eq. (4.1) is used since the particulate temperature — kinetic energy — and screening length are then conveniently proportional to Γ^{-1} and κ^{-1}.)

For example, for ion density $n_i = 10^9\,\mathrm{cm}^{-3}$, temperature $T_i = 0.1\,\mathrm{eV}$ ($\ll T_e$), and charge $q = Z_i e = e$, and particulate density $n = 10^6\,\mathrm{cm}^{-3}$, temperature (i.e., kinetic energy) $T = 0.1\,\mathrm{eV}$, and charge $-Q = -Z_D e = -10^3 e$, we have $\kappa = 0.83$, $\Gamma = 232$, and $\Gamma^* = 101$. The system may be called "strongly coupled" since the ratio of the typical interparticle energy to the thermal energy ($\simeq \Gamma^*$) is sufficiently larger than 1. The free electron density is determined by charge neutrality: $n_e = Z_i n_i - Z_D n \approx 0$ in this case, i.e., all electrons are attached to dust grains. The example is typical of process plasmas, but κ and Γ may vary widely depending on the plasma state.

If the system is not in thermodynamic equilibrium, particulates may be subject to various forces, including drag forces[18] and polarization forces,[19,20] in addition to the interparticle forces.

4.2. Derivation of the field potential

We first derive the electrostatic potential generated by charged particulates and a neutralizing background medium confined to a cubical domain V of side length L ($V = L^3$). The potential satisfies periodic boundary conditions.

Consider a system of N identical, infinitesimally small dust grains of mass m and charge $-Q = -Z_D e$. The average density of dust grains is then given by $n = N/V$. The potential $\Psi(\mathbf{r})$ satisfies Poisson's equation

$$\Delta\Psi(\mathbf{r}) = -\frac{\rho(\mathbf{r})}{\varepsilon_0}, \tag{4.2}$$

where the charge density $\rho(\mathbf{r})$ is given by

$$\rho(\mathbf{r}) = -Q\sum_{j=1}^{N}\delta(\mathbf{r}-\mathbf{r}_j) + q n_i(\mathbf{r}) - e n_e(\mathbf{r}).$$

Here $q = Z_i e$ denotes the charge on each ion, and $n_i(\mathbf{r})$ and $n_e(\mathbf{r})$ are the ion and electron densities at position $\mathbf{r}$. The overall charge neutrality condition requires $\int_V \rho(\mathbf{r})d\mathbf{r} = 0$. We shall assume ions of a single species; the extension to multiple species is straightforward.

Assuming that motion of charged particulates is sufficiently slow so that the background plasma may be considered in thermal equilibrium at each time instance, we may employ Boltzmann distributions for ions and electrons, i.e., $n_\alpha(\mathbf{r}) \propto \exp(-q_\alpha\beta_\alpha\Psi)$ for $\alpha = i, e$ where $q_i = q$, $q_e = -e$, and $\beta_\alpha = 1/k_B T_\alpha$.[21] The ion and electron temperatures, T_i and T_e, are assumed to be constant throughout V. Defining the mean ion and electron densities by

$$\bar{n}_\alpha = \frac{1}{V}\int_V n_\alpha(\mathbf{r})\,d\mathbf{r} \quad \text{for } \alpha = i, e,$$

we have

$$n_\alpha(\mathbf{r}) = \frac{\bar{n}_\alpha \exp(-q_\alpha\beta_\alpha(\Psi(\mathbf{r}) - C))}{V^{-1}\int_V \exp(-q_\alpha\beta_\alpha(\Psi(\mathbf{r}) - C))\,d\mathbf{r}}, \tag{4.3}$$

where C is an arbitrary constant. If the constant C may be chosen in such a way that the conditions

$$|q_\alpha\beta_\alpha(\Psi(\mathbf{r}) - C)| \ll 1 \tag{4.4}$$

hold everywhere for $\alpha = i$ and e (i.e., the variation of $\Psi(\mathbf{r})$ over V is much smaller than the thermal energy $k_B T_\alpha$), Eq. (4.3) may be linearized to obtain

$$n_\alpha(\mathbf{r}) = q_\alpha\bar{n}_\alpha[1 - q_\alpha\beta_\alpha\varphi(\mathbf{r})], \tag{4.5}$$

where

$$\varphi(\mathbf{r}) = \Psi(\mathbf{r}) - \overline{\Psi} \tag{4.6}$$

and

$$\overline{\Psi} = \frac{1}{V}\int_V \Psi(\mathbf{r})\, d\mathbf{r}\,.$$

Using Eq. (4.5), we rewrite the charge density as

$$\rho(\mathbf{r}) = -Q\sum_{j=1}^{N}\delta(\mathbf{r}-\mathbf{r}_j) + Qn - \varepsilon_0 k_D^2\varphi(\mathbf{r}). \tag{4.7}$$

Here $k_D^2 = \sum_\alpha q_\alpha^2 \bar{n}_\alpha \beta_\alpha/\varepsilon_0 = 1/\lambda_i^2 + 1/\lambda_e^2$ (where λ_i and λ_e are the ion and electron Debye lengths) and we have used the condition of overall charge neutrality,

$$Qn = q\bar{n}_i - e\bar{n}_e\,.$$

The first term of Eq. (4.7)

$$\rho_D = -Q\sum_{j=1}^{N}\delta(\mathbf{r}-\mathbf{r}_j) \tag{4.8}$$

obviously represents the particulate charge density. The second term

$$\rho_0^{\mathrm{bg}} = Qn \tag{4.9}$$

represents the constant background charges that neutralize the particulate charges, and the third term

$$\delta\rho^{\mathrm{bg}} = -\varepsilon_0 k_D^2\varphi(\mathbf{r}) \tag{4.10}$$

represents the background plasma density perturbation due to the electrostatic perturbation. Note that the space average of $\delta\rho^{\mathrm{bg}}$ vanishes; there is no net charge contribution from Eq. (4.10). Note also that the charge perturbation $\delta\rho^{\mathrm{bg}}$ vanishes in the high plasma temperature limit (i.e., $T_i, T_e \to \infty$ and therefore $k_D \to 0$) since the background plasma becomes so mobile in this limit that it can maintain a uniform density. As mentioned in the previous section, this is the OCP limit.

Under the linear response conditions (4.5), Eq. (4.2) may be rewritten as

$$(\Delta - k_D^2)\varphi(\mathbf{r}) = \frac{Q}{\varepsilon_0}\sum_{j=1}^{N}\left[\delta(\mathbf{r}-\mathbf{r}_j) - \frac{1}{V}\right]. \tag{4.11}$$

Periodic boundary conditions for a cube of side length L ($V = L^3$) require

$$\varphi(\mathbf{r}+\mathbf{n}L) = \varphi(\mathbf{r}), \tag{4.12}$$

where $\mathbf{n} = (\ell, m, n)$ denotes a integer triplet. This periodic boundary condition may be used in MC or MD simulations to emulate an infinite system.

The Green's function $G(\mathbf{r},\mathbf{r}')$ for the operator $\Delta - k_D^2$ defined on the unit cell $D = \{(x,y,z) \mid 0 \le x,y,z \le L\}$ with periodic boundary conditions is given by

$$G(\mathbf{r},\mathbf{r}') = \frac{1}{4\pi}\sum_{\mathbf{n}}\frac{\exp(-k_D|\mathbf{r}-\mathbf{r}'-\mathbf{n}L|)}{|\mathbf{r}-\mathbf{r}'-\mathbf{n}L|} \quad (\mathbf{r},\mathbf{r}' \in D),$$

where $\sum_{\mathbf{n}}$ denotes the sum over all integer triplets $\mathbf{n}$. Using this Green's function, one may express the solution to Eq. (4.11) as

$$\begin{aligned}\varphi(\mathbf{r}) &= \frac{-Q}{4\pi\varepsilon_0}\sum_{j=1}^{N}\int_D\sum_{\mathbf{n}}\frac{\exp(-k_D|\mathbf{r}-\mathbf{r}'-\mathbf{n}L|)}{|\mathbf{r}-\mathbf{r}'-\mathbf{n}L|}\left[\delta(\mathbf{r}'-\mathbf{r}_j) - \frac{1}{L^3}\right]d\mathbf{r}' \\ &= \frac{-Q}{4\pi\varepsilon_0}\sum_{j=1}^{N}\sum_{\mathbf{n}}\int_{D_{\mathbf{n}}}\frac{\exp(-k_D|\mathbf{r}-\boldsymbol{\rho}|)}{|\mathbf{r}-\boldsymbol{\rho}|}\left[\delta(\boldsymbol{\rho}-\mathbf{r}_j-\mathbf{n}L) - \frac{1}{L^3}\right]d\boldsymbol{\rho},\end{aligned} \tag{4.13}$$

where $\boldsymbol{\rho} = \mathbf{r}' + \mathbf{n}L$ and $D_{\mathbf{n}} = D + \mathbf{n}L = \{(x+\ell L, y+mL, z+nL) \mid (x,y,z) \in D\}$. Note that, for a given $\mathbf{n}$ and $\boldsymbol{\rho} \in D_{\mathbf{n}}$, the equation $\delta(\boldsymbol{\rho}-\mathbf{r}_j-\mathbf{n}'L) = 0$ holds for all $\mathbf{n}' \neq \mathbf{n}$ since $\mathbf{r}_j \in D$. Thus we have

$$\delta(\mathbf{r}'-\mathbf{r}_j) = \delta(\boldsymbol{\rho}-\mathbf{r}_j-\mathbf{n}L) = \sum_{\mathbf{n}'}\delta(\boldsymbol{\rho}-\mathbf{r}_j-\mathbf{n}'L).$$

Using this relation and the fact that $\sum_{\mathbf{n}}\int_{D_{\mathbf{n}}} = \int_{V_\infty}$ with V_∞ being the entire space $\mathbf{R}^3$, we obtain from Eq. (4.13)

$$\varphi(\mathbf{r}) = \frac{-Q}{4\pi\varepsilon_0}\int_{V_\infty}\frac{\exp(-k_D|\mathbf{r}-\boldsymbol{\rho}|)}{|\mathbf{r}-\boldsymbol{\rho}|}\sum_{j=1}^{N}\left[\sum_{\mathbf{n}}\delta(\boldsymbol{\rho}-(\mathbf{r}_j+\mathbf{n}L)) - \frac{1}{L^3}\right]d\boldsymbol{\rho}$$

$$= -\frac{Q}{4\pi\varepsilon_0}\sum_{j=1}^{N}\sum_{\mathbf{n}}\frac{\exp(-k_D|\mathbf{r}-\mathbf{r}_j-\mathbf{n}L|)}{|\mathbf{r}-\mathbf{r}_j-\mathbf{n}L|}+\frac{Qn}{\varepsilon_0 k_D^2}. \tag{4.14}$$

From the above it is easy to verify that $\int_D \varphi(\mathbf{r})\,d\mathbf{r}=0$. From Eq. (4.6), we obtain

$$\Psi(\mathbf{r}) = -\frac{Q}{4\pi\varepsilon_0}\sum_{j=1}^{N}\sum_{\mathbf{n}}\frac{\exp(-k_D|\mathbf{r}-\mathbf{r}_j-\mathbf{n}L|)}{|\mathbf{r}-\mathbf{r}_j-\mathbf{n}L|}, \tag{4.15}$$

and

$$\overline{\Psi} = -\frac{Qn}{\varepsilon_0 k_D^2}.$$

As might be expected, the potential $\Psi(\mathbf{r})$ given above comprises Yukawa potentials $\phi(|\mathbf{r}|)$ for all the particulates (at $\mathbf{r}_j$) in D and all their images (at $\mathbf{r}_j+\mathbf{n}L$) under periodic boundary conditions.

4.3. Hamiltonian for Yukawa systems

As shown in Appendix D, the Hamiltonian for the system of N particulates is given by

$$H = \sum_{j=1}^{N}\frac{|\mathbf{p}_j^2|}{2m}+U_{\rm ex}, \tag{4.16}$$

where $\mathbf{p}_j$ is the momentum of the j-th particulate and $U_{\rm ex}$ is the Helmholtz free energy of the particulates and background plasma. The term $U_{\rm ex}$ is also called the "excess energy" since it represents the energy in excess of the thermal (kinetic) energy of the particulates.

The excess energy has the form

$$U_{\rm ex} = F_{\rm id}^{\rm bg}+F_{\rm int}^{\rm bg}, \tag{4.17}$$

where

$$F_{\rm id}^{\rm bg} = \sum_{\alpha=i,e} k_B T_\alpha \int_V n_\alpha(\mathbf{r})[\ln n_\alpha(\mathbf{r})\Lambda_{T\alpha}^3-1]\,d\mathbf{r} \tag{4.18}$$

denotes the ideal gas contribution to the background free energy and

$$F_{\rm int}^{\rm bg} = \frac{1}{2}\int_V \rho(\mathbf{r})\Psi(\mathbf{r})\,d\mathbf{r}-\frac{Q^2}{8\pi\varepsilon_0}\sum_{j=1}^{N}\int_V\frac{\delta(\mathbf{r}-\mathbf{r}_j)}{|\mathbf{r}-\mathbf{r}_j|}\,d\mathbf{r} \tag{4.19}$$

represents the electrostatic potential energy of all the charged species. In Eq. (4.18), $\Lambda_{T\alpha}=(h^2/2\pi m_\alpha k_B T_\alpha)^{1/2}$ denotes the thermal de Broglie wavelength. The second term in Eq. (4.19) serves to subtract the infinite self-energy of each dust grain, which is formally included in the first term.

Substituting the linear response relation (4.5) into (4.18) and taking the terms up to the second order in $q_\alpha\beta\varphi(\mathbf{r})$, we obtain

$$F_{\rm id}^{\rm bg} = F_{\rm unif}^{\rm bg}+\tfrac{1}{2}\varepsilon_0 k_D^2\int_{V_\infty}\varphi^2(\mathbf{r})\,d\mathbf{r}, \tag{4.20}$$

where

$$F_{\rm unif}^{\rm bg} = V\sum_\alpha k_B T_\alpha \overline{n}_\alpha(\ln\overline{n}_\alpha\Lambda_{T\alpha}^3-1) \tag{4.21}$$

is the free energy of the uniform (i.e., unperturbed) background plasma. Since $F_{\rm unif}^{\rm bg}$ only provides obvious thermodynamical information on the unperturbed (ideal gas) background plasma, we shall drop this term from the $U_{\rm ex}$ expression in the following argument for simplicity.

If the linear response relation (4.5) holds, we may write Eq. (4.20) (after ignoring the term $F_{\rm unif}^{\rm bg}$) as

$$F_{\rm id}^{\rm bg} = -\frac{1}{2}\int_V \delta\rho^{\rm bg}(\mathbf{r})\Psi(\mathbf{r})\,d\mathbf{r}. \tag{4.22}$$

Clearly this free energy is equal in size but opposite in sign to the potential energy of background plasma perturbations. Note that $F_{\rm id}^{\rm bg}$ vanishes as $k_D\to 0$, i.e., in the OCP limit (see Appendix E).

Substituing Eqs. (4.8)-(4.10) into Eqs. (4.19) and (4.22), we obtain the excess energy of the Yukawa system as

$$U_{\rm ex} = -\frac{Q}{2}\int_V\sum_{j=1}^{N}\left[\delta(\mathbf{r}-\mathbf{r}_j)-\frac{1}{V}\right]\Psi(\mathbf{r})\,d\mathbf{r} - \frac{Q^2}{8\pi\varepsilon_0}\sum_{j=1}^{N}\int_V\frac{\delta(\mathbf{r}-\mathbf{r}_j)}{|\mathbf{r}-\mathbf{r}_j|}\,d\mathbf{r}. \tag{4.23}$$

From Eq. (4.15), it is straightforward to confirm that Eq. (4.23) may be written as

$$U_{ex} = \frac{1}{2}\sum_{i\neq j}\sum \psi(\mathbf{r}_i - \mathbf{r}_j) + U_0\,, \tag{4.24}$$

with the pair potential

$$\psi(\mathbf{R}) = \frac{Q^2}{4\pi\varepsilon_0}\int_{V_\infty}\left[\sum_{\mathbf{n}}\delta(\boldsymbol{\rho}-\mathbf{n}L) - \frac{1}{L^3}\right]\frac{\exp(-k_D|\boldsymbol{\rho}-\mathbf{R}|)}{|\boldsymbol{\rho}-\mathbf{R}|}\,d\boldsymbol{\rho}. \tag{4.25}$$

and the constant

$$U_0 = \tfrac{1}{2}N\lim_{|\mathbf{R}|\to 0}\left(\psi(\mathbf{R}) - \frac{Q^2}{4\pi\varepsilon_0|\mathbf{R}|}\right). \tag{4.26}$$

Carrying out the integration in Eq. (4.25), we obtain

$$\psi(\mathbf{R}) = \frac{Q^2}{4\pi\varepsilon_0}\sum_{\mathbf{n}}\frac{\exp(-k_D|\mathbf{R}-\mathbf{n}L|)}{|\mathbf{R}-\mathbf{n}L|} - \frac{Q^2}{\varepsilon_0 k_D^2 L^3} \tag{4.27}$$

and the energy constant

$$U_0 = -\frac{Q^2 n}{2\varepsilon_0 k_D^2} - \frac{NQ^2 k_D}{8\pi\varepsilon_0} + \frac{Q^2 N}{8\pi\varepsilon_0}\sum_{\mathbf{n}\neq 0}\frac{\exp(-k_D L|\mathbf{n}|)}{|\mathbf{n}|L} \tag{4.28}$$

It is easy to confirm that $\psi(\mathbf{R}) = \psi(-\mathbf{R})$.

From Eqs. (4.24), (4.27), and (4.28), it is sometimes more convenient to express the excess energy in terms of the periodic Yukawa pair potential

$$\Phi(\mathbf{R}) = \frac{Q^2}{4\pi\varepsilon_0}\sum_{\mathbf{n}}\frac{\exp(-k_D|\mathbf{R}-\mathbf{n}L|)}{|\mathbf{R}-\mathbf{n}L|}$$

as

$$\begin{aligned} U_{ex} = {} & \frac{1}{2}\sum_{i\neq j}\sum \Phi(\mathbf{r}_i - \mathbf{r}_j) \\ & - \frac{NQ^2 n}{2\varepsilon_0 k_D^2} - \frac{NQ^2 k_D}{8\pi\varepsilon_0} + \frac{Q^2 N}{8\pi\varepsilon_0}\sum_{\mathbf{n}\neq 0}\frac{\exp(-k_D L|\mathbf{n}|)}{|\mathbf{n}|L} \end{aligned} \tag{4.29}$$

In Eq. (4.29), the second term on the right-hand side represents the free energy (excluding the uniform ideal gas free energy) of the background plasma that, on average, neutralizes

the charge of the particulates. The third term represents the free energy of each sheath (see Eq. (17) of Ref. 19), and the fourth term represents the energy of interaction of every particulate and its own images under periodic boundary conditions.

The equation of motion of each particulate may be obtained directly from the Hamiltonian, i.e., Eqs. (4.16) and (4.29), as

$$\frac{d\mathbf{p}_i}{dt} = -\sum_{j(\neq i)=1}^{N}\frac{\partial}{\partial\mathbf{r}_i}\Phi(\mathbf{r}_i - \mathbf{r}_j).$$

This is the equation for the ith particulate that will be used in the MD simulations described in the succeeding chapter. Note that particulates interact with each other through the Yukawa potential.

The Yukawa pair potential may also be derived from the density functional approach[22] under the conditions that we have stated above; e.g., sufficiently high background-plasma temperatures Eq. (4.4), which allows the linearization of the density perturbation Eq. (4.5) — this is often referred to as small "inhomogeneity" —, and weak coupling of the background-plasma, which allows us to neglect the correlation term discussed in Appendix D. Under more general conditions, of course, the true interparticle potential deviates from the Yukawa potential. To study such a general system, one may use *ab initio* numerical simulations.[23]

4.4. Classical OCP limit

If the background screening is sufficiently weak ($\kappa = k_D a \ll 1$), one expects the densities of the background species, $n_i(\mathbf{r})$ and $n_e(\mathbf{r})$, to become almost uniform due to the rapid thermal motions of these species, and thus the system will approach the classical one-component plasma. However, this is not immediately apparent from the pair potential expressions given in Eq. (4.27) since both the first and second terms diverge as $k_D \to 0$. We now show that the form (4.27) of the pair potential appropriate to periodic boundary conditions does in fact reduce to the standard Ewald potential[9,10,24,25] for the classical OCP in the limit $\kappa \to 0$.

The classical OCP consists of ions (which correspond to our dust grains) of charge Q and a uniform electron background giving overall charge neutrality. The ions interact with each other through the Coulomb potential, and thus the pair potential for the OCP is given by

$$\psi^{\mathrm{OCP}}(\mathbf{R}) = \frac{Q^2}{4\pi\varepsilon_0}\int_{V_\infty}\left[\sum_{\mathbf{n}}\delta(\rho-\mathbf{n}L)-\frac{1}{L^3}\right]\frac{1}{|\rho-\mathbf{R}|}\,d\rho. \tag{4.30}$$

The second term in the square bracket is proportional to the charge due to the uniform background. The infinite lattice sum in this expression is only conditionally convergent, and the physically-meaningful convergent sum is given by the Ewald potential:

$$\begin{aligned}\psi^{\mathrm{OCP}}(\mathbf{R}) &= \frac{Q^2}{4\pi\varepsilon_0}\left[\frac{\mathrm{erfc}(\sqrt{\pi}\,|\mathbf{R}|/L)}{|\mathbf{R}|}-\frac{1}{L}\right]\\ &+\frac{Q^2}{4\pi\varepsilon_0}\sum_{\mathbf{n}\neq 0}\left[\frac{\mathrm{erfc}(\sqrt{\pi}\,|\mathbf{R}+\mathbf{n}L|/L)}{|\mathbf{R}+\mathbf{n}L|}+\frac{\exp(-\pi|\mathbf{n}|^2)\cos(2\pi\mathbf{n}\cdot\mathbf{R}/L)}{\pi|\mathbf{n}|^2L}\right],\end{aligned} \tag{4.31}$$

where erfc( ) is the complementary error function. The excess energy is then given by[9,10]:

$$U_{ex}^{\mathrm{OCP}} = \frac{1}{2}\sum_{i}\sum_{j\neq i}\psi^{\mathrm{OCP}}(\mathbf{r}_i-\mathbf{r}_j)+U_0^{\mathrm{OCP}},$$

where, as in Eq. (4.26),

$$U_0^{\mathrm{OCP}} = \tfrac{1}{2}N\lim_{|\mathbf{R}|\to 0}\left(\psi^{\mathrm{OCP}}(\mathbf{R})-\frac{Q^2}{4\pi\varepsilon_0|\mathbf{R}|}\right) \tag{4.32}$$

$$\approx -1.4186487\,\frac{Q^2N}{4\pi\varepsilon_0 L}. \tag{4.33}$$

The pair potential for the Yukawa system is given by Eq. (4.25), or equivalently Eq. (4.27). It is evident from Eq. (4.25) and Eq. (4.30) that $\psi(\mathbf{R})\to\psi^{\mathrm{OCP}}(\mathbf{R})$ as $k_D\to 0$. However, it is not clear how each term of the Ewald potential (4.31) corresponds to the terms of the Yukawa pair potential. To establish this correspondence, we now derive an alternative expression for the Yukawa pair potential $\psi(\mathbf{r})$.

Let us split $\psi(\mathbf{R})$ in Eq. (4.25) into the following two parts:

$$\psi(\mathbf{R}) = \psi_1(\mathbf{R})+\psi_2(\mathbf{R}),$$

where

$$\psi_1(\mathbf{R}) = \frac{Q^2}{4\pi\varepsilon_0}\int_{V_\infty} w(\rho)\eta(|\rho-\mathbf{R}|)\frac{\exp(-k_D|\rho-\mathbf{R}|)}{|\rho-\mathbf{R}|}\,d\rho, \tag{4.34}$$

$$\psi_2(\mathbf{R}) = \frac{Q^2}{4\pi\varepsilon_0}\int_{V_\infty} w(\rho)[1-\eta(|\rho-\mathbf{R}|)]\frac{\exp(-k_D|\rho-\mathbf{R}|)}{|\rho-\mathbf{R}|}\,d\rho. \tag{4.35}$$

In these expressions we have introduced the functions

$$w(\rho) = \sum_{\mathbf{n}}\delta(\rho-\mathbf{n}L)-\frac{1}{L^3},$$

$$\eta(x) = A\int_x^\infty \exp(k_Dt-\gamma^2t^2)\,dt = B\,\mathrm{erfc}\left(\gamma x-\frac{k_D}{2\gamma}\right),$$

where

$$A = \frac{2\gamma B}{\sqrt{\pi}}\exp\left(-\frac{k_D^2}{4\gamma^2}\right)\quad\text{and}\quad B = \frac{1}{1+\mathrm{erf}(k_D/2\gamma)}.$$

Here γ is a positive constant (which will be set to be $\sqrt{\pi}/L$ later) and erf( ) is the error function, $\mathrm{erf}(x)\equiv 1-\mathrm{erfc}(x)$. Note that

$$\eta(0) = A\int_0^\infty \exp(k_Dt-\gamma^2t^2)\,dt = 1,$$

$$1-\eta(x) = A\int_0^x \exp(k_Dt-\gamma^2t^2)\,dt,$$

and

$$\lim_{k_D\to 0}\eta(x) = \mathrm{erfc}(\gamma x).$$

Evaluating the integral in Eq. (4.34) yields

$$\begin{aligned}\psi_1(\mathbf{R}) &= \frac{Q^2}{4\pi\varepsilon_0}\left\{\frac{\eta(|\mathbf{R}|)}{|\mathbf{R}|}\exp(-k_D|\mathbf{R}|)\right.\\ &\left.-\frac{4\pi}{k_D^2L^3}\left[1-\frac{\exp(-k_D^2/4\gamma^2)}{1+\mathrm{erf}(k_D/2\gamma)}\left(1+\frac{k_D}{\sqrt{\pi}\gamma}\right)\right]\right\}\\ &+\frac{Q^2}{4\pi\varepsilon_0}\sum_{\mathbf{n}\neq 0}\frac{\eta(|\mathbf{R}-\mathbf{n}L|)}{|\mathbf{R}-\mathbf{n}L|}\exp(-k_D|\mathbf{R}-\mathbf{n}L|).\end{aligned} \tag{4.36}$$

By setting $\gamma = \sqrt{\pi}/L$, one can readily confirm that the first term (i.e., all the terms in the bracket) of Eq. (4.36) corresponds to the first term of the Ewald potential (4.31) in the

$k_D \to 0$ limit, and the second term corresponds to the first term in the second square bracket of Eq. (4.31):

$$\lim_{k_D \to 0} \psi_1(\mathbf{R}) = \frac{Q^2}{4\pi\varepsilon_0}\left[\frac{\mathrm{erfc}(\sqrt{\pi}\,|\mathbf{R}|/L)}{|\mathbf{R}|} - \frac{1}{L}\right] + \frac{Q^2}{4\pi\varepsilon_0}\sum_{\mathbf{n}\neq 0}\frac{\mathrm{erfc}(\sqrt{\pi}\,|\mathbf{R}+\mathbf{n}L|/L)}{|\mathbf{R}+\mathbf{n}L|}.$$

To evaluate $\psi_2(\mathbf{R})$ in Eq. (4.35) we use Parseval's identity. The Fourier transform of $w(\mathbf{R})$ is

$$\tilde{w}(\mathbf{k}) = \sum_{\mathbf{n}} \exp(2\pi i L\mathbf{r}\cdot\mathbf{n}) - \frac{1}{L^3}\,\delta(\mathbf{k})$$

Since the Poisson sum formula yields

$$\sum_{\mathbf{n}} \exp(2\pi i L\mathbf{r}\cdot\mathbf{n}) = \frac{1}{L^3}\sum_{\mathbf{n}}\delta\left(\mathbf{k}-\frac{\mathbf{n}}{L}\right),$$

we obtain

$$\tilde{w}(\mathbf{k}) = \frac{1}{L^3}\sum_{\mathbf{n}\neq 0}\delta\left(\mathbf{k}-\frac{\mathbf{n}}{L}\right). \tag{4.37}$$

On the other hand, the Fourier transform of the term

$$[1-\eta(|\boldsymbol{\rho}-\mathbf{R}|)]\frac{\exp(-k_D|\boldsymbol{\rho}-\mathbf{R}|)}{|\boldsymbol{\rho}-\mathbf{R}|}$$

may be calculated by means of integration by parts:

$$\begin{aligned}
F(\mathbf{k}) &= \frac{2A}{k}\exp(2\pi i\mathbf{k}\cdot\mathbf{R})\int_0^\infty dx\,\sin(2\pi kx)\exp(-k_D x)\int_0^x dt\,\exp(k_D t-\gamma^2 t^2)\\
&= \frac{2A}{k}\frac{\exp(2\pi i\mathbf{k}\cdot\mathbf{R})}{k_D^2+4\pi^2k^2}\int_0^\infty dx\,(k_D\sin 2\pi kx + 2\pi k\cos 2\pi kx)\exp(-\gamma^2x^2)\\
&= \frac{2A}{k}\frac{\exp(2\pi i\mathbf{k}\cdot\mathbf{R})}{k_D^2+4\pi k^2}\frac{\exp(-\pi^2k^2/\gamma^2)}{\gamma}\left[\pi\sqrt{\pi}k + k_D\int_0^{\pi k/\gamma}dt\,\exp(t^2)\right],
\end{aligned}$$

where $k = |\mathbf{k}|$. Therefore, from Parseval's identity, we obtain

$$\begin{aligned}
\psi_2(\mathbf{R}) &= \frac{Q^2}{4\pi\varepsilon_0}\frac{1}{L^3}\int\sum_{\mathbf{n}\neq 0}\delta\left(\mathbf{k}-\frac{\mathbf{n}}{L}\right)F(\mathbf{k})\,d\mathbf{k}\\
&= \frac{Q^2}{4\pi\varepsilon_0}\frac{2A}{\gamma L}\sum_{\mathbf{n}\neq 0}\exp\left(\frac{2\pi i\mathbf{n}\cdot\mathbf{R}}{L}\right)\exp\left(-\frac{\pi^2|\mathbf{n}|^2}{\gamma^2L^2}\right)\left[\frac{\pi\sqrt{\pi}}{k_D^2L^2+4\pi^2|\mathbf{n}|^2}\right.\\
&\quad\left.+\frac{k_DL}{(k_D^2L^2+4\pi^2|\mathbf{n}|^2)|\mathbf{n}|}\int_0^{\pi|\mathbf{n}|/\gamma L}dt\,\exp(t^2)\right]
\end{aligned} \tag{4.38}$$

Noting the asymptotic expansion

$$\begin{aligned}
\exp(-x^2)\int_0^x \exp(t^2)\,dt &\overset{\text{asymp}}{=} \sum_{m=0}^{\infty}\frac{(2m-1)!!}{2^{m+1}x^{2m+1}} \qquad \text{as } x\to\infty\\
&= \frac{1}{2x}+\frac{1}{4x^3}+\cdots
\end{aligned}$$

one see that the infinite sum over $\mathbf{n}\neq\mathbf{0}$ of the second term in the square bracket of Eq. (4.38) converges algebraically. Therefore, with $\gamma = \sqrt{\pi}/L$, the potential $\psi_2(\mathbf{R})$ corresponds to the second term in the second square bracket of the Ewald potential (4.31), i.e,

$$\lim_{k_D\to 0}\psi_2(\mathbf{R}) = \frac{Q^2}{4\pi\varepsilon_0}\sum_{\mathbf{n}\neq 0}\frac{\exp(2\pi i\mathbf{n}\cdot\mathbf{R}/L)\exp(-\pi|\mathbf{n}|^2)}{\pi|\mathbf{n}|^2L}. \tag{4.39}$$

Note that the functions $\exp(2\pi i\mathbf{n}\cdot\mathbf{R}/L)$ in Eqs. (4.38) and (4.39) may be replaced by their real parts $\cos(2\pi\mathbf{n}\cdot\mathbf{R}/L)$, since the imaginary parts cancel when the summations are taken over $\mathbf{n}$.

It is evident that $U_0 \to U_0^{\mathrm{OCP}}$ since Eqs. (4.26) and (4.32) hold and $\psi(\mathbf{R}) \to \psi^{\mathrm{OCP}}(\mathbf{R})$. Although both the first and third terms of Eq. (4.28) diverge as $k_D \to 0$, the difference of these terms converges to the constant given by Eq. (4.33).

4.5. Concluding remarks

We have derived the excess energy U_{ex} (i.e., Eq. (4.29)) of the Yukawa system under periodic boundary conditions, taking into account the energy contributions from the background charges. It was also demonstrated that U_{ex} converges to the excess energy U_{ex}^{OCP} of the OCP system in the weak screening limit (i.e., $\kappa = k_Da \to 0$). The derived excess energy serves as a basis for calculating various thermodynamical quantities from simulation data, especially near the OCP limit, as demonstrated in the next chapter. (Note that the obvious contributions from the unperturbed ideal-gas background to the excess energy, which is given by Eq. (4.21), is not included in U_{ex} of Eq. (4.29) for simplicity.)

It is interesting to note that the excess energy U_{ex} is the Helmholtz free energy of the system, rather than the internal energy $\langle H_{micro} \rangle$, as shown in Appendix D. This is of course due to the fact that the background species are continuously exchanging energy with a heat bath so as to maintain constant temperature during the particulate motion. Historically, there was some confusion in this respect: at an early stage of the development of lyophobic colloid theory, erroneous pair potentials were derived from the total potential energy.[26] The errors were later corrected when the use of Helmholtz free energy was suggested by Derjaguin[27] and Verwey and Overbeek.[28,29]

The pair potentials that may be derived from the total potential energy $\langle H_{micro} \rangle$ exhibits an attractive potential superimposed on the Yukawa repulsive potential [see Eq. (E.7) in Appendix E]. This fallacious attractive potential was once used to account for the experimentally observed attraction between colloid particles, which is now essentially explained by the Van der Waals interactions. The attractive potential reflects the electrostatic potential between the space charge in the Debye sheath of one particulate and the opposite charge on another particulate.

This potential would incur an attractive force between particulates if the space charges were "attached" to the particulate and thus the particulate and its Debye sheath formed an inseparable single system. In reality, however, the sheath space charge is merely a perturbation of the background plasma induced by the charge on the particulate. If the particulate moves from position A to position B, the plasma will relax to the unperturbed state around A and a new perturbation will be formed around B. The Debye sheaths are thus not "attached" to the particulates at all.

The true behavior of the background charges is indeed thermodynamically expressed by the second term of Eq. (D.4), i.e., the heat gain by the system from the heat bath. The ideal-gas contribution to the Helmholtz free energy F_{id}^{bg} of Eq. (4.22) — which is essentially the heat term of Eq. (D.4) — exactly cancels the attractive potential energy included in

$\langle H_{micro} \rangle$. The resulting true pair potential then becomes the Yukawa potential.

In the OCP limit, the ideal-gas Helmholtz free energy F_{id}^{bg} vanishes, as demonstrated in Appendix E. Consequently, for the OCP system, the excess energy U_{ex}^{OCP} indeed agrees with its total potential energy. Therefore, in most studies of the OCP system, the excess energy U_{ex}^{OCP} is simply derived from the total potential energy (e.g., Ref. 9) although its physical meaning should be the Helmholtz free energy, as has been discussed in this chapter.

References

[1]S. Hamaguchi and R. T. Farouki, J. Chem. Phys. **101**, 9876 (1994).

[2]R. O. Rosenberg and D. Thirumalai, Phys. Rev. A **36**, 5690 (1987).

[3]M. O. Robbins, K. Kremer, and G. S. Grest, J. Chem. Phys. **88**, 3286 (1988).

[4]E. J. Meijer and D. Frenkel, J. Chem. Phys. **94**, 2269 (1991).

[5]R. T. Farouki and S. Hamaguchi, Appl. Phys. Lett. **61**, 2973 (1992).

[6]R. T. Farouki and S. Hamaguchi, J. Comp. Phys. **115**, 276 (1994).

[7]S. Hamaguchi, R. T. Farouki, and D. H. E. Dubin, Phys. Rev. E (1997) (in press).

[8]S. Hamaguchi, R. T. Farouki, and D. H. E. Dubin, J. Chem. Phys. **105**, 7641 (1996).

[9]S. G. Brush, H. L. Sahlin, and E. Teller, J. Chem. Phys. **45**, 2102 (1966).

[10]J.-P. Hansen, Phys. Rev. A **8**, 3096 (1973).

[11]H. E. DeWitt, Phys. Rev. A **14**, 1290 (1976).

[12]M. Baus and J.-P. Hansen, Phys. Rep. **59**, 1 (1980).

[13]S. Ichimaru, Rev. Mod. Phys. **54**, 1017 (1982).

[14]G. S. Stringfellow, H. E. DeWitt, and W. L. Slattery, Phys. Rev. A**41**, 1105 (1990).

[15]*Strongly Coupled Plasma Physics*, (F. J. Rogers and H. E. DeWitt, eds.), Plenum Press, New York (1986).

[16]R. T. Farouki and S. Hamaguchi, Phys. Rev. E, **47**, 4330 (1993).

[17]H. Ikezi, Phys. Fluids **29**, 1764 (1986).

[18]T. G. Northrop and T. J. Birmingham, Planet. Space Sci. **38**, 319 (1990).

[19]S. Hamaguchi and R. T. Farouki, Phys. Rev. E **49**, 4430 (1994).

[20]S. Hamaguchi and R. T. Farouki, Phys. Plasmas **1**, 2110 (1994).

[21]E. C. Whipple, T. G. Northrop, and D. A. Mendis, J. Geophys. Res. **90**, 7405 (1985).

[22]Y. Rosenfeld, Phys. Rev. E **49**, 4425 (1994).

[23]H. Löwen, P. A. Madden, and J.-P. Hansen, Phys. Rev. Lett. **68**, 1081 (1992).

[24]P. P. Ewald, Ann. Phys. **64**, 253 (1921).

[25]B. R. A. Nijboer and F. W. De Wette, Physica **23**, 309 (1957).

[26]S. Levine and G. P. Dube, Trans. Faraday Soc. **35**, 1125, 1141 (1939).

[27]B. Derjaguin, Trans. Faraday Soc. **36**, 203 (1940).

[28]E. J. Verwey and J. Th. G. Overbeek, Discuss. Faraday Soc. B **42**, 117 (1946).

[29]E. J. Verwey and J. Th. G. Overbeek, *Theory of the stability of lyophobic colloids*, Elsevier, Amsterdam (1948).

Chapter 5

Phase diagram of Yukawa systems

5.1. Introduction

In this chapter, we employ molecular dynamics (MD) simulation to obtain the phase diagram of Yukawa systems.[1-3] Small particles in a plasma are typically negatively-charged, due to the high mobility of electrons, and they interact with each other through a Yukawa-type (i.e., screened Coulomb) pair potential, as we have discussed in the preceding chapters. Laboratory experiments have recently demonstrated that, when the interparticle potential energy exceeds the kinetic energy, particulates in plasmas may form crystalline structures (Coulomb crystals).[4-10] The goal of this chapter is to determine under what conditions dust particles in a plasma form Coulomb crystals.

As in the previous chapter, let us consider a system of identical particles of mass m, charge $-Q = -Ze$ ($Z > 1$) immersed in a neutralizing background plasma. The interparticle potential is of Yukawa type, given by

$$\phi(r) = \frac{Q^2}{4\pi\epsilon_0 r}\exp(-k_D r),$$

where r denotes the radial distance between two particles. The Debye length $\lambda_D = k_D^{-1}$ of the background plasma is defined by

$$\lambda_D = \left(\frac{q_i^2\bar{n}_i}{\epsilon_0 kT_i} + \frac{e^2\bar{n}_e}{\epsilon_0 kT_e}\right)^{-1/2},$$

q_i, $\bar{n}_i$, and T_i being the charge, mean density, and temperature of plasma ions, and $-e$, $\bar{n}_e$, and T_e the corresponding quantities for plasma electrons.

Using the Wigner–Seitz radius $a = (3/4\pi n)^{1/3}$ as the unit of length, where n is the particle number density, we may describe the thermodynamics of the Yukawa system in terms of two dimensionless ratios:

$$\kappa = \frac{a}{\lambda_D} \quad \text{and} \quad \Gamma = \frac{Q^2}{4\pi\epsilon_0 akT}. \tag{5.1}$$

Note that parameter Γ is roughly the ratio of the (unscreened) Coulomb potential energy to the kinetic energy per particle.

Although we have derived in the preceding chapter Yukawa systems as models for dust particles in plasmas, Yukawa systems also serve as models for monodisperse colloidal particles in electrolyte solutions. As mentioned earlier, it is recognized in early 1940s that the interparticle potential between such colloidal particles may be described essentially by the Yukawa potential.[11-13] Especially after experimental observations of phase transitions[14-17] were made in colloidal systems, Yukawa systems began to attract theoretical interest. For example, energy calculations of Yukawa systems at zero temperature showed that the solid phase transition from bcc to fcc occurs as κ increases.[18,19] For non-zero temperatures, the fcc–bcc and melting phase transitions were also studied theoretically[20,21] (the results of which are now unfortunately known to be inconsistent with those of recent numerical studies).

Despite this long history of scientific interest in Yukawa systems, it is only after mid 1980s that extensive numerical simulations[22,23] were used to study thermodynamical properties of Yukawa systems. The only exception is the special case of $\kappa = 0$, i.e., the OCP (a system of mobile charges immersed in a strictly uniform neutralizing background), which has been extensively studied numerically[24-30] since mid 1960s as a model for the interior of white dwarf stars. Including such OCP simulations, most of early MC and MD simulations were conducted for systems of soft-core potentials, i.e., $\phi(r) \propto 1/r^n$ (which becomes the OCP

potential at $n = 1$ and the hard-core potential at $n \to \infty$) and its variations (such as the Lennard-Jones potential) in the light of interest in condensed matter physics.

In this chapter, we are mainly interested in the regime of weak Debye screening ($\kappa \lesssim 1$), which is relevant to experimental observations of strongly-coupled particulate systems in plasmas. No simulation has been done previously in this regime, except for the case of $\kappa = 0$ (OCP). We also apply this MD method to more strongly screened Yukawa systems, up to $\kappa = 5$, and compare the results with those of earlier MD and MC simulation studies[22,23,31-33] of Yukawa systems. These earlier simulations employed potential cutoffs, and are therefore applicable only to the regime $\kappa \gg 1$.

5.2. Free energy calculations

For MD simulations in the weak-screening regime, where the range of the interparticle force becomes comparable to or greater than the side L of the cubical simulation volume, one must use the effective pair potential[3]

$$\Phi(\mathbf{r}) = \phi(|\mathbf{r}|) + \sum_{\mathbf{n}\neq 0} \phi(|\mathbf{r} + \mathbf{n}L|), \tag{5.2}$$

which reflects periodic boundary conditions imposed on the simulation box, to emulate correct particle-particle interactions. In the above equation, $\Phi(\mathbf{r})$ represents the interaction energy of particle i with particle j (at separation $\mathbf{r} = \mathbf{r}_j - \mathbf{r}_i$) and with all periodic images of the latter. The infinite sum of ϕ over integer vectors $\mathbf{n} = (l, m, n)$ represents the periodic images. Numerically this periodic image potential is approximated by a tensor-product spline function interpolating an array of $40 \times 40 \times 40$ discrete values, summed to high accuracy. The approximation can be efficiently evaluated in the simulations and has a fractional deviation from the exact value of no more than $\sim 10^{-7}$. Full details of the approximation scheme may be found in Ref. 34.

The total potential energy (or "excess energy") U of the model system with periodic

boundary conditions is then given by the expression

$$\frac{U}{NkT} = \Gamma \left[\frac{1}{N} \sum_{j=1}^{N-1} \sum_{k=j+1}^{N} \tilde{\Phi}(\boldsymbol{\xi}_k - \boldsymbol{\xi}_j) - \frac{3}{2\kappa^2} - \frac{\kappa}{2} + \frac{1}{2} \sum_{\mathbf{n}\neq 0} \frac{\exp(-\kappa|\mathbf{n}|\Lambda)}{|\mathbf{n}|\Lambda} \right], \tag{5.3}$$

where N is the number of particles, $\Lambda = L/a = (4\pi N/3)^{1/3}$ is the size of the cubical simulation volume in units of the Wigner-Seitz radius, $\boldsymbol{\xi}_i = \mathbf{r}_i/a$ is the dimensionless location of particle i, and $\tilde{\Phi} = 4\pi\varepsilon_0 a \Phi/Q^2$.

The energy associated with the background plasma in Eq. (5.3) is not just the potential energy, but the free energy — including the contribution of the entropy associated with thermal motions of the plasma ions and electrons. Thus, the partial derivative of U with respect to $\mathbf{r}_i$ gives the true force on the i-th particle,[35] as we have discussed in the preceding chapter. In Eq. (5.3), the second term inside the square bracket represents the free energy (excluding the uniform ideal gas free energy) of the background plasma that, on average, neutralizes the charge of the particulates. The third term represents the free energy of each Debye sheath [see Eq. (2.16)], and the fourth term represents the energy of interaction of each particulate with its own images under periodic boundary conditions.

In the limit of $\kappa \to 0$, the first, second, and last terms on the right-hand side of Eq. (5.3) diverge in such a manner that the limiting value of U equals the well-known expression $U_{\rm OCP}$ for the OCP potential energy given[3,24] by

$$\frac{U_{\rm OCP}}{NkT} = \Gamma \left[\frac{1}{N} \sum_{j=1}^{N-1} \sum_{k=j+1}^{N} \tilde{\Phi}^{\rm OCP}(\boldsymbol{\xi}_k - \boldsymbol{\xi}_j) + \frac{E_m}{2} \right],$$

where

$$\Phi^{\rm OCP}(\boldsymbol{\xi}) = \frac{\mathrm{erfc}(\sqrt{\pi}\,\xi/\Lambda)}{\xi} - \frac{1}{\Lambda} + \sum_{\mathbf{n}\neq 0} \left[\frac{\mathrm{erfc}(\sqrt{\pi}\,|\boldsymbol{\xi} + \mathbf{n}\Lambda|/\Lambda)}{|\boldsymbol{\xi} + \mathbf{n}\Lambda|} + \frac{\exp(-\pi|\mathbf{n}|^2)\cos(2\pi\mathbf{n}\cdot\boldsymbol{\xi}/\Lambda)}{\pi|\mathbf{n}|^2\Lambda} \right]$$

and

$$E_m = \lim_{\xi \to 0} \left[\tilde{\Phi}_{\rm OCP}(\xi) - \frac{1}{\xi} \right] = \frac{-2.837297479}{\Lambda}.$$

Here $\xi = \xi_k - \xi_j$ denotes the position of particle k relative to particle j and $\mathrm{erfc}(\cdot)$ is the complementary error function. As the screening length increases (i.e., as $\kappa \to 0$), each particulate has an increasingly strong interaction with both the charge-neutralizing background plasma and the other charged particulates. Thus, the magnitude of the background-plasma free energy — the second term in Eq. (5.3) — increases to cancel the increase of direct electrostatic interactions among charged particles, i.e., the first and last terms in Eq. (5.3).

To see the correspondence between the Yukawa system and OCP system more clearly, one may write

$$U = \sum_{j=1}^{N-1} \sum_{k=j+1}^{N} \psi(\mathbf{r}_k - \mathbf{r}_j) + U_0,$$

where

$$\frac{\psi(\mathbf{r})}{NkT} = \frac{\Gamma}{N} \left[\tilde{\Phi}(\xi) - \frac{3}{\kappa^2 N} \right],$$

and

$$\frac{U_0}{NkT} = \frac{\Gamma}{2} \left[\sum_{\mathbf{n} \neq \mathbf{0}} \frac{\exp(-\kappa|\mathbf{n}|\Lambda)}{|\mathbf{n}|\Lambda} - \frac{3}{\kappa^2 N} - \kappa \right].$$

Then, in the OCP limit $\kappa \to 0$, one can show that the pair potential ψ and energy constant U_0 converge to those of the OCP, i.e., $\psi \to \psi^{\rm OCP}$ and $U_0 \to U_0^{\rm OCP}$, where

$$\begin{aligned} \psi^{\rm OCP}(\mathbf{r}) &= \frac{Q^2}{4\pi\varepsilon_0} \int_{V_\infty} \left[\sum_{\mathbf{n}} \delta(\boldsymbol{\rho} - \mathbf{n}L) - \frac{1}{L^3} \right] \frac{1}{|\boldsymbol{\rho} - \mathbf{r}|} \, d\boldsymbol{\rho} \\ &= \frac{Q^2}{4\pi\varepsilon_0 a} \tilde{\Phi}^{\rm OCP}(\xi) \end{aligned}$$

and

$$\begin{aligned} U_0^{\rm OCP} &= \tfrac{1}{2} N \lim_{|\mathbf{r}| \to 0} \left(\psi^{\rm OCP}(\mathbf{r}) - \frac{Q^2}{4\pi\varepsilon_0 |\mathbf{r}|} \right) \\ &= \frac{Q^2 N}{8\pi\varepsilon_0 a} E_m \\ &= -1.4186487 \frac{Q^2 N}{4\pi\varepsilon_0 L}. \end{aligned}$$

We denote the internal energy and Helmholtz free energy per particle in units of kT by

$$u = \frac{U}{NkT}, \qquad f = \frac{F}{NkT}. \tag{5.4}$$

The thermal component of the potential energy is defined by

$$u_{\rm th}(\kappa, \Gamma) = u(\kappa, \Gamma) - u_\infty(\kappa),$$

where $u_\infty(\kappa)$ represents the Madelung energy (for an appropriate lattice) per particle in units of kT. We also define

$$E(\kappa) = \lim_{\Gamma \to \infty} \frac{u(\kappa, \Gamma)}{\Gamma},$$

i.e., the Madelung energy per particle in units of $Q^2/4\pi\epsilon_0 a$, so that $u_\infty(\kappa) = E(\kappa)\Gamma$. In the limit of zero temperature (i.e., $\Gamma \to \infty$), we evidently have $u(\kappa, \infty) = u_\infty(\kappa)$. The values for the bcc and fcc Madelung energies, $E_{\rm bcc}(\kappa)$ and $E_{\rm fcc}(\kappa)$, are listed in Table 5.1. Note that the bcc Madelung energy is smaller than the fcc Madelung energy[3,19] $[E_{\rm bcc}(\kappa) < E_{\rm fcc}(\kappa)]$ for $\kappa < 1.066$.

Since $\partial f / \partial \Gamma = u(\kappa, \Gamma)/\Gamma$, the dimensionless Helmholtz free energy for the fluid phase may be defined by

$$f_{\rm fluid}(\kappa, \Gamma) = \int_0^\Gamma u(\kappa, \Gamma') \frac{d\Gamma'}{\Gamma'} + f_{\rm ideal}(\Gamma). \tag{5.5}$$

Here the last term represents the ideal-gas contribution to the total free energy, i.e.,

$$\begin{aligned} f_{\rm ideal}(\Gamma) &= \ln \left[\left(\frac{2\pi\hbar^2}{mkT} \right)^{3/2} n \right] - 1 \\ &= 3 \ln \Gamma + \frac{3}{2} \ln (kT)_{\rm Ry} - 1 + \ln \frac{3\sqrt{\pi}}{4}, \end{aligned} \tag{5.6}$$

where $(kT)_{\rm Ry}$ denotes kT measured in Rydberg units, $\frac{1}{2}(Q^2/4\pi\epsilon_0\hbar)^2 m$, for the particle. Although $f_{\rm ideal}$ depends on $(kT)_{\rm Ry}$ as well as Γ, we do not explicitly express the dependence on the former for the sake of simplicity.

For the solid phase, we use

$$f_{\rm solid}(\kappa, \Gamma) = \int_\infty^\Gamma \left[u_{\rm th}(\kappa, \Gamma') - \frac{3}{2} \right] \frac{d\Gamma'}{\Gamma'} + f_{\rm harm}(\kappa, \Gamma), \tag{5.7}$$

κ	$E_{\rm bcc}$	$E_{\rm fcc}$
0.0	−0.895929	−0.895873
0.1	−0.896966	−0.896911
0.2	−0.900074	−0.900020
0.3	−0.905240	−0.905190
0.4	−0.912448	−0.912402
0.5	−0.921671	−0.921631
0.6	−0.932879	−0.932844
0.7	−0.946032	−0.946004
0.8	−0.961088	−0.961067
0.9	−0.977997	−0.977984
1.0	−0.996706	−0.996701
1.1	−1.017158	−1.017161
1.2	−1.039292	−1.039302
1.4	−1.088350	−1.088374
1.6	−1.143352	−1.143389
1.8	−1.203757	−1.203803
2.0	−1.269026	−1.269079
2.2	−1.338637	−1.338694
2.4	−1.412096	−1.412154
2.6	−1.488941	−1.488998
2.8	−1.568750	−1.568804
3.0	−1.651144	−1.651194
3.2	−1.735781	−1.735826
3.4	−1.822360	−1.822400
3.6	−1.910618	−1.910653
3.8	−2.000326	−2.000356
4.0	−2.091283	−2.091309
4.2	−2.183319	−2.183341
4.4	−2.276286	−2.276304
4.6	−2.370058	−2.370072
4.8	−2.464525	−2.464537
5.0	−2.559596	−2.559606

Table 5.1: Madelung energies for bcc and fcc Yukawa lattices.

where $u_{\rm th} - 3/2$ is the anharmonic component of the potential energy in units of kT. The free energy for the harmonic lattice vibration is given by

$$f_{\rm harm}(\kappa,\Gamma) = E(\kappa)\Gamma + \Sigma(\kappa) + \frac{9}{2}\ln\Gamma + \frac{3}{2}\ln(kT)_{\rm Ry} + \frac{3}{2}\ln\frac{3}{2}, \tag{5.8}$$

where $\Sigma(\kappa)$ denotes the harmonic entropy constant, i.e.,

$$\Sigma(\kappa) = \lim_{N\to\infty}\frac{1}{N}\sum_{k=1}^{3N-3}\ln\frac{\omega_k}{\omega_{\rm p}}. \tag{5.9}$$

Here the sum is taken over the $3N-3$ normal-mode frequencies ω_k for the oscillation of a lattice of N particles. The eigenfrequencies ω_k of an N-particle Yukawa lattice may be computed using standard techniques,[36] and the quantity $\Sigma(\kappa)$ can then be estimated for various κ values by letting $N \to \infty$. Table 5.2 gives the values of $\Sigma(\kappa)$ for bcc and fcc Yukawa lattices. (The data of Table 5.2 was obtained by D. H. E. Dubin from lattice-dynamics calculations[1,2,37]). Note that the bcc structure becomes unstable for $\kappa > 4.76$ against shear in the (110) direction.[23] The OCP values (i.e., $\kappa = 0$) in Table 5.2 are taken from Table I of Ref. 38.

5.3. Molecular dynamics simulation method

MD simulations are used to evaluate the potential energy u for given values of the thermodynamic variables κ and Γ. In the MD simulations, the equations of motion

$$\frac{d^2\mathbf{r}_i}{dt^2} = -\sum_{j(\neq i)}^{N}\nabla\Phi(\mathbf{r}_i - \mathbf{r}_j)$$

for $i = 1, 2, \cdots N$ with the effective pair potential $\Phi(\mathbf{r})$ given by Eq. (5.2) are integrated and the velocities of all particles are renormalized periodically to bring the system kinetic energy into agreement with the target Γ value. The number of particles N used for the simulations reported here are $N = 686$ for a bcc and $N = 500$ for an fcc lattice. These lattices are used

κ	$\Sigma_{\rm bcc}$	$\Sigma_{\rm fcc}$
0.0	−2.4939	−2.4537
0.2	−2.5172	−2.4767
0.4	−2.5808	−2.5393
0.6	−2.6829	−2.6394
0.8	−2.8185	−2.7722
1.0	−2.9843	−2.9347
1.2	−3.1773	−3.1236
1.4	−3.3950	−3.3366
1.6	−3.6350	−3.5714
1.8	−3.8953	−3.8259
2.0	−4.1740	−4.0985
2.2	−4.4697	−4.3876
2.4	−4.7805	−4.6916
2.6	−5.1054	−5.0095
2.8	−5.4430	−5.3398
3.0	−5.7922	−5.6817
3.2	−6.1522	−6.0341
3.4	−6.5220	−6.3962
3.6	−6.9008	−6.7673
3.8	−7.2878	−7.1466
4.0	−7.6826	−7.5334
4.2	−8.0847	−7.9273
4.4	−8.4936	−8.3275
4.6	−8.9095	−8.7337
4.8	—	−9.1455
5.0	—	−9.5625

Table 5.2. Harmonic entropy constants for bcc and fcc Yukawa lattices.[1,2,37] The values at $\kappa = 0$ are quoted from Ref. 38. Note that the bcc structure becomes unstable for $\kappa > 4.76$ against shear in the (110) direction.[23]

as initial conditions, and the system is allowed to equilibrate to the desired Γ for typically 100 time units before averaging its properties over $100 < \tau < 300$. Here the time unit is defined to be $\sqrt{3}\,\omega_{\rm p}^{-1}$ with the plasma frequency of the particles $\omega_{\rm p} = \sqrt{Q^2 n/\epsilon_0 m}$, so that $\tau = \omega_{\rm p} t/\sqrt{3}$. For some large Γ values, we allowed the the system to equilibrate for 300 time units. Cases that melted to a fluid state did so well before $\tau = 100$.

The potential (i.e., excess) energy per particle (in units of $Q^2/4\pi\epsilon_0 a$), u/Γ, for various Γ and κ values ($\kappa \leq 1$) obtained from MD simulations is listed in Tables 5.3, 5.4 and 5.5, For each run in this Table, the initial state is either a bcc (N=686) or an fcc lattice (N=500) and therefore in the solid state the structure remains as the given lattice. We did not consider fcc lattices for the runs of $\kappa \leq 1$ since the Madelung energy for an bcc lattice is always lower than that of the corresponding fcc lattice for $\kappa < 1.066$, as mentioned earlier. These energy data are used to evaluate the free energy of the system through Eqs. (5.5) and (5.7).

For the fluid phase, we assume that the potential energy depends on Γ as

$$u(\kappa,\Gamma) = a(\kappa)\Gamma + b(\kappa)\Gamma^s + c(\kappa) + d(\kappa)\Gamma^{-s} \tag{5.10}$$

with $s = 1/3$ for $\Gamma \leq 1$. The coefficients a, b, c, and d, which are functions of κ, are determined by fitting measured potential energies to the above expression. The functional form of Eq. (5.10) has been applied to internal energy fitting of various OCP simulations.[28] The well-defined dependence of u on Γ given in Eq. (5.10) makes it easier to evaluate the integral of Eq. (5.5). Since Eq. (5.10) diverges as $\Gamma \to 0$, we evaluate the integral of Eq. (5.5) by a direct numerical quadrature for $\Gamma \leq 1$:

$$f_{\rm fluid}(\kappa,\Gamma) = \int_1^\Gamma u(\kappa,\Gamma')\,\frac{{\rm d}\Gamma'}{\Gamma'} + f_1(\kappa) + f_{\rm ideal}(\Gamma), \tag{5.11}$$

with

$$f_1(\kappa) = \int_0^1 u(\kappa,\Gamma')\,\frac{{\rm d}\Gamma'}{\Gamma'}, \tag{5.12}$$

where Eq. (5.10) is used to evaluate the first integral of Eq. (5.11) and $f_1(\kappa)$ is evaluated through a Simpson-rule quadrature of the u/Γ values given in Tables 5.6. Note that $u/\Gamma \to$

Γ	$\kappa = 0.0$	$\kappa = 0.2$	$\kappa = 0.4$
1	-0.57173 ± 0.01388	-0.57866 ± 0.01429	-0.59912 ± 0.01449
2	-0.65983 ± 0.00800	-0.66589 ± 0.00785	-0.68345 ± 0.00775
5	-0.75101 ± 0.00419	-0.75677 ± 0.00425	-0.77038 ± 0.00396
10	-0.79954 ± 0.00235	-0.80447 ± 0.00250	-0.81795 ± 0.00235
20	-0.83340 ± 0.00136	-0.83783 ± 0.00147	-0.85100 ± 0.00143
40	-0.85648 ± 0.00078	-0.86064 ± 0.00086	-0.87340 ± 0.00078
60	-0.86595 ± 0.00052	-0.87029 ± 0.00056	-0.88290 ± 0.00060
80	-0.87156 ± 0.00046	-0.87578 ± 0.00047	-0.88841 ± 0.00049
100	-0.87519 ± 0.00035	-0.87944 ± 0.00041	-0.89196 ± 0.00033
120	-0.87786 ± 0.00033	-0.88200 ± 0.00031	-0.89444 ± 0.00035
140	-0.87982 ± 0.00031	-0.88404 ± 0.00029	-0.89656 ± 0.00029

Γ	$\kappa = 0.6$	$\kappa = 0.8$	$\kappa = 1.0$
1	-0.63168 ± 0.01266	-0.67876 ± 0.01273	-0.73423 ± 0.01155
2	-0.71215 ± 0.00876	-0.75145 ± 0.00761	-0.79866 ± 0.00718
5	-0.79536 ± 0.00380	-0.82793 ± 0.00395	-0.87127 ± 0.00396
10	-0.84051 ± 0.00240	-0.87192 ± 0.00245	-0.91103 ± 0.00238
20	-0.87284 ± 0.00136	-0.90269 ± 0.00145	-0.94029 ± 0.00143
40	-0.89471 ± 0.00078	-0.92372 ± 0.00080	-0.96063 ± 0.00080
60	-0.90385 ± 0.00061	-0.93265 ± 0.00060	-0.96910 ± 0.00059
80	-0.90907 ± 0.00044	-0.93773 ± 0.00043	-0.97408 ± 0.00049
100	-0.91261 ± 0.00036	-0.94126 ± 0.00034	-0.97735 ± 0.00036
120	-0.91523 ± 0.00032	-0.94366 ± 0.00033	-0.97976 ± 0.00030
140	-0.91718 ± 0.00029	-0.94556 ± 0.00028	-0.98156 ± 0.00029
160	-0.91874 ± 0.00027	-0.94705 ± 0.00025	-0.98303 ± 0.00025
180	—	—	-0.98423 ± 0.00022

Table 5.3: (a)Excess energy per particle, u/Γ, obtained from MD simulations for $\kappa \leq 1$. The numbers after $\pm$ indicate fluctuation levels. The number of simulation particles is $N = 686$.

Γ	$\kappa = 1.2$	$\kappa = 1.4$	$\kappa = 2.0$
1	-0.797097 ± 0.010904	-0.869746 ± 0.011675	-1.110066 ± 0.009674
2	-0.855439 ± 0.009179	-0.920097 ± 0.008272	—
5	-0.921138 ± 0.004200	-0.978642 ± 0.004510	-1.184378 ± 0.003545
10	-0.958561 ± 0.002799	-1.012022 ± 0.002587	-1.208846 ± 0.002178
20	-0.985481 ± 0.001533	-1.037095 ± 0.001467	-1.227788 ± 0.001343
40	-1.004536 ± 0.000893	-1.055146 ± 0.000911	-1.241424 ± 0.000743
60	-1.012768 ± 0.000683	-1.062759 ± 0.000616	-1.247832 ± 0.000638
80	-1.017387 ± 0.000559	-1.067144 ± 0.000495	-1.251210 ± 0.000509
100	-1.020683 ± 0.000433	-1.070322 ± 0.000426	-1.253666 ± 0.000469
120	-1.022726 ± 0.000427	-1.072513 ± 0.000409	—
140	-1.024535 ± 0.000353	-1.074088 ± 0.000329	—
160	-1.025919 ± 0.000310	-1.075469 ± 0.000253	—
180	-1.027188 ± 0.000249	-1.076467 ± 0.000301	—
200	-1.028005 ± 0.000250	-1.077485 ± 0.000250	-1.259467 ± 0.000268
240	—	-1.078874 ± 0.000204	—

Γ	$\kappa = 2.6$	$\kappa = 3.0$	$\kappa = 3.6$
1	-1.377115 ± 0.008032	-1.563017 ± 0.006990	-1.847809 ± 0.005863
5	-1.427355 ± 0.003300	-1.602063 ± 0.002709	-1.875608 ± 0.002235
10	-1.444503 ± 0.002193	-1.615664 ± 0.001819	-1.885249 ± 0.001503
20	-1.457552 ± 0.001221	-1.625862 ± 0.001042	-1.892620 ± 0.000969
40	-1.467763 ± 0.000669	-1.633625 ± 0.000660	-1.898153 ± 0.000550
60	-1.472134 ± 0.000512	-1.637184 ± 0.000492	-1.900557 ± 0.000408
80	-1.474749 ± 0.000426	-1.639302 ± 0.000357	-1.902094 ± 0.000293
100	-1.476616 ± 0.000361	-1.640850 ± 0.000293	-1.903025 ± 0.000299
200	-1.480988 ± 0.000187	-1.644389 ± 0.000195	-1.905567 ± 0.000166
400	-1.484027 ± 0.000116	-1.646847 ± 0.000115	-1.907295 ± 0.000101
700	-1.485724 ± 0.000076	-1.648282 ± 0.000079	-1.908312 ± 0.000057
1000	—	—	-1.908807 ± 0.000051
2000	—	—	-1.909541 ± 0.000025

Table 5.3: (b) Equilibrium potential energy per particle, u/Γ, in the fluid phase for $\kappa > 1$. The numbers after $\pm$ indicate fluctuation levels. The number of simulation particles is $N = 500$.

Γ	$\kappa = 4.0$	$\kappa = 4.6$	$\kappa = 5.0$
1	-2.040283 ± 0.004831	-2.332756 ± 0.004502	-2.528765 ± 0.003806
5	-2.063313 ± 0.001730	-2.350043 ± 0.001769	-2.542942 ± 0.001500
10	-2.070905 ± 0.001221	-2.355369 ± 0.001234	-2.547653 ± 0.000874
20	-2.077051 ± 0.000695	-2.359643 ± 0.000679	-2.551214 ± 0.000552
40	-2.081242 ± 0.000456	-2.362851 ± 0.000449	-2.553848 ± 0.000315
60	-2.083236 ± 0.000332	-2.364342 ± 0.000337	-2.554926 ± 0.000240
80	-2.084381 ± 0.000227	-2.365221 ± 0.000239	-2.555673 ± 0.000196
100	-2.085288 ± 0.000209	-2.365722 ± 0.000205	-2.556105 ± 0.000173
200	-2.087226 ± 0.000135	-2.367119 ± 0.000122	-2.557248 ± 0.000086
400	-2.088586 ± 0.000082	-2.368103 ± 0.000075	-2.558051 ± 0.000052
700	-2.089387 ± 0.000049	-2.368670 ± 0.000049	-2.558476 ± 0.000036
1000	-2.089779 ± 0.000040	-2.368941 ± 0.000035	-2.558705 ± 0.000023
2000	-2.090338 ± 0.000019	-2.369329 ± 0.000018	-2.559011 ± 0.000017
3000	—	-2.369513 ± 0.000015	-2.559144 ± 0.000012
4000	—	-2.369609 ± 0.000014	-2.559223 ± 0.000009
5000	—	-2.369679 ± 0.000011	-2.559275 ± 0.000009
6000	—	-2.369727 ± 0.000010	-2.559310 ± 0.000006
8000	—	—	-2.559366 ± 0.000007
10000	—	—	-2.559410 ± 0.000005

Table 5.3: (b) Equilibrium potential energy per particle for $\kappa > 1$ (continued). The number of simulation particles are $N = 500$ for $\kappa = 4.6$ and $N = 686$ for $\kappa = 4.0$ and 5.0.

Γ	$\kappa = 0.0$	$\kappa = 0.2$	$\kappa = 0.4$
160	$-0.88561^{*} \pm 0.00027$	$-0.88930^{*} \pm 0.00065$	$-0.90216^{*} \pm 0.00030$
180	-0.88706 ± 0.00021	-0.89118 ± 0.00023	-0.90352 ± 0.00019
200	-0.88800 ± 0.00020	-0.89214 ± 0.00020	-0.90449 ± 0.00023
240	-0.88943 ± 0.00016	-0.89357 ± 0.00014	-0.90593 ± 0.00015
300	-0.89078 ± 0.00012	-0.89492 ± 0.00012	-0.90729 ± 0.00012
400	-0.89210 ± 0.00009	-0.89624 ± 0.00009	-0.90861 ± 0.00012
500	-0.89288 ± 0.00008	-0.89702 ± 0.00008	-0.90939 ± 0.00008
600	-0.89340 ± 0.00007	-0.89754 ± 0.00007	-0.90991 ± 0.00007
800	-0.89404 ± 0.00005	-0.89818 ± 0.00005	-0.91055 ± 0.00005
1000	-0.89442 ± 0.00004	-0.89856 ± 0.00004	-0.91093 ± 0.00004
∞	-0.89593	-0.90007	-0.91245

Γ	$\kappa = 0.6$	$\kappa = 0.8$	$\kappa = 1.0$
180	$-0.92377^{*} \pm 0.00022$	$-0.95173^{*} \pm 0.00026$	—
200	-0.92488 ± 0.00021	-0.95304 ± 0.00020	$-0.98821^{*} \pm 0.00030$
240	-0.92634 ± 0.00016	-0.95451 ± 0.00016	-0.99008 ± 0.00017
300	-0.92770 ± 0.00012	-0.95590 ± 0.00011	-0.99149 ± 0.00015
400	-0.92903 ± 0.00009	-0.95723 ± 0.00009	-0.99284 ± 0.00010
500	-0.92982 ± 0.00007	-0.95802 ± 0.00008	-0.99364 ± 0.00007
600	-0.93034 ± 0.00006	-0.95854 ± 0.00007	-0.99416 ± 0.00006
800	-0.93098 ± 0.00004	-0.95919 ± 0.00005	-0.99480 ± 0.00005
1000	-0.93136 ± 0.00004	-0.95957 ± 0.00004	-0.99519 ± 0.00004
∞	-0.93288	-0.96109	-0.99671

Table 5.4: (a) Equilibrium potential energy per particle, u/Γ, for bcc solids ($N = 686$) for $\kappa \leq 1$. The numbers after $\pm$ indicate fluctuation levels. The energy value with asterisk (*) was not used for fitting since the value clearly deviates from either fitting curve, indicating the system is in a mixed fluid–solid state. Note that $u/\Gamma \to E_{\mathrm{bcc}}(\kappa)$ as $\Gamma \to \infty$.

Γ	$\kappa = 1.2$	$\kappa = 1.4$	$\kappa = 2.0$
240	$-1.032521^{\bullet} \pm 0.000184$	—	—
300	-1.034044 ± 0.000117	-1.083042 ± 0.000134	—
400	-1.035414 ± 0.000103	-1.084449 ± 0.000099	—
500	-1.036214 ± 0.000072	-1.085260 ± 0.000088	—
600	-1.036742 ± 0.000064	-1.085788 ± 0.000054	—
700	—	—	-1.266822 ± 0.000063
800	-1.037388 ± 0.000045	-1.086444 ± 0.000042	—
1000	-1.037774 ± 0.000044	-1.086828 ± 0.000038	-1.267497 ± 0.000040
2000	—	—	-1.268270 ± 0.000022
∞	-1.039292	-1.088350	-1.269026

Γ	$\kappa = 2.6$	$\kappa = 3.0$	$\kappa = 3.6$
1000	-1.487386 ± 0.000041	—	—
2000	—	-1.650380 ± 0.000021	—
3000	-1.488437 ± 0.000017	-1.650640 ± 0.000016	—
4000	-1.488563 ± 0.000014	-1.650767 ± 0.000016	-1.910240 ± 0.000011
5000	-1.488639 ± 0.000012	-1.650843 ± 0.000014	-1.910317 ± 0.000010
6000	—	-1.650893 ± 0.000012	-1.910368 ± 0.000010
8000	—	-1.650956 ± 0.000009	-1.910431 ± 0.000009
∞	-1.488941	-1.651144	-1.910618

Γ	$\kappa = 4.0$
5000	-2.090982 ± 0.000009
6000	-2.091033 ± 0.000007
8000	-2.091097 ± 0.000006
10000	-2.091134 ± 0.000004
13000	-2.091169 ± 0.000003
16000	-2.091190 ± 0.000003
∞	-2.091283

Table 5.4: (b) Equilibrium potential energy per particle, u/Γ, for bcc solids ($N = 686$) for $\kappa > 1$. The numbers after $\pm$ indicate fluctuation levels. The energy value with asterisk ($^{\bullet}$) was not used for fitting since the value clearly deviates from either fitting curve, indicating the system is in a mixed fluid–solid state. Note that $u/\Gamma \to E_{bcc}(\kappa)$ as $\Gamma \to \infty$.

Γ	$\kappa = 1.2$	$\kappa = 1.4$	$\kappa = 2.0$
240	$-1.032173^{\bullet} \pm 0.000228$	—	—
300	-1.034003 ± 0.000150	-1.082998 ± 0.000165	—
400	-1.035392 ± 0.000110	-1.084437 ± 0.000114	—
500	-1.036209 ± 0.000085	-1.085274 ± 0.000091	—
600	-1.036735 ± 0.000071	-1.085804 ± 0.000082	—
700	—	—	-1.266858 ± 0.000068
800	-1.037390 ± 0.000058	-1.086460 ± 0.000057	—
1000	-1.037778 ± 0.000046	-1.086849 ± 0.000049	-1.267541 ± 0.000051
2000	—	—	-1.268320 ± 0.000031
∞	-1.039302	-1.088374	-1.269079

Γ	$\kappa = 2.6$	$\kappa = 3.0$	$\kappa = 3.6$
1000	-1.487424 ± 0.000061	—	—
2000	—	-1.650422 ± 0.000029	—
3000	-1.488490 ± 0.000021	-1.650685 ± 0.000016	—
4000	-1.488618 ± 0.000017	-1.650813 ± 0.000010	-1.910270 ± 0.000013
5000	-1.488695 ± 0.000015	-1.650890 ± 0.000011	-1.910349 ± 0.000014
6000	—	-1.650941 ± 0.000010	-1.910400 ± 0.000013
8000	—	—	-1.910464 ± 0.000010
∞	-1.488998	-1.651194	-1.910653

Γ	$\kappa = 4.0$	$\kappa = 4.6$	$\kappa = 5.0$
5000	-2.091000 ± 0.000010	—	—
6000	-2.091054 ± 0.000011	—	—
8000	-2.091119 ± 0.000006	—	—
10000	-2.091158 ± 0.000004	-2.369920 ± 0.000006	—
13000	-2.091193 ± 0.000004	-2.369956 ± 0.000004	—
16000	-2.091214 ± 0.000004	-2.369979 ± 0.000003	—
20000	—	-2.369997 ± 0.000003	-2.559530 ± 0.000003
25000	—	—	-2.559546 ± 0.000002
30000	—	-2.370022 ± 0.000002	-2.559556 ± 0.000002
40000	—	-2.370034 ± 0.000002	-2.559568 ± 0.000003
50000	—	—	-2.559576 ± 0.000002
∞	-2.091309	-2.370072	-2.559606

Table 5.5: Equilibrium potential energy per particle, u/Γ, for fcc solids ($N = 500$). The numbers after $\pm$ indicate fluctuation levels. The energy value with asterisk ($^{\bullet}$) was not used for fitting since the value clearly deviates from either fitting curve, indicating the system is in a mixed fluid–solid state. Note that $u/\Gamma \to E_{fcc}(\kappa)$ as $\Gamma \to \infty$.

$-\kappa/2$ as $\Gamma \to 0$. The value $-\kappa/2$ represents the normalized energy of the Debye sheath.[39] The numerical values of $f_1(\kappa)$ are listed in Table 5.7.

For $\kappa \leq 1$, we assume polynomial dependence of the normalized potential energy u on κ (i.e., Taylor expansion around $\kappa = 0$) and fit the function over the dual independent variables κ and Γ. For example, we may first write $a(\kappa) = E_{\rm bcc}(\kappa) + \delta a(\kappa)$ and apply least-squares fit to $E_{\rm bcc}(\kappa)$ data of $\kappa \leq 1$ given in Table 5.1. The resulting expression becomes[3]

$$E_{\rm bcc}(\kappa) = -\,0.895929 \;-\; 0.103731\,\kappa^2 + 0.003084\,\kappa^4 - 0.000131\,\kappa^6 \qquad \text{for} \;\; \kappa \leq 1\,. \tag{5.13}$$

To fit the fluid data given in Table 5.3(a) to expression (5.10) for $\kappa \leq 1$, we take the dependence of the coefficients $\delta a, b, c, d$ on κ to be no more than quartic with even powers only (the odd-power terms do not appear in the expressions, as discussed in Ref. 40), i.e., we write

$$\delta a(\kappa) = \delta a_0 + \delta a_2\kappa^2 + \delta a_4\kappa^4\,,$$

and similarly for $b(\kappa)$, $c(\kappa)$, and $d(\kappa)$. Twelve term fits of the fluid data over the dual independent variables κ and Γ yield

$$\delta a(\kappa) = -\,0.003366 \;+\; 0.000660\kappa^2 \;-\; 0.000089\kappa^4\,, \tag{5.14}$$

$$b(\kappa) = \;\; 0.565004 \;-\; 0.026134\kappa^2 \;-\; 0.002689\kappa^4\,, \tag{5.15}$$

$$c(\kappa) = -\,0.206893 \;-\; 0.086384\kappa^2 \;+\; 0.018278\kappa^4\,, \tag{5.16}$$

$$d(\kappa) = -\,0.031402 \;+\; 0.042429\kappa^2 \;-\; 0.008037\kappa^4\,, \tag{5.17}$$

for $\kappa \leq 1$.

For the solid phase, the following form for the thermal potential energy is assumed:

$$u_{\rm th}(\kappa, \Gamma) = \frac{3}{2} + \frac{A_1(\kappa)}{\Gamma} + \frac{A_2(\kappa)}{\Gamma^2}\,, \tag{5.18}$$

Γ	$\kappa = 0.0$	$\kappa = 0.2$	$\kappa = 0.4$	$\kappa = 0.6$	$\kappa = 0.8$
0.00	0.0000	−0.100000	−0.200000	−0.300000	−0.400000
0.10	−0.265180	−0.280939	−0.329445	−0.392027	−0.475008
0.20	−0.348262	−0.360031	−0.393997	−0.452019	−0.519462
0.40	−0.443081	−0.450926	−0.479437	−0.525131	−0.579895
0.60	−0.496155	−0.508795	−0.531896	−0.573248	−0.623842
0.80	−0.540589	−0.547594	−0.570788	−0.608673	−0.656128
1.00	−0.571726	−0.578664	−0.599118	−0.631676	−0.678762

Γ	$\kappa = 1.0$	$\kappa = 1.2$	$\kappa = 1.4$	$\kappa = 2.0$	$\kappa = 2.6$
0.00	−0.500000	−0.600000	−0.700000	−1.000000	−1.300000
0.10	−0.557792	−0.648425	−0.740415	−1.025685	−1.319127
0.20	−0.596414	−0.680595	−0.770037	−1.042716	−1.331495
0.40	−0.648070	−0.724539	−0.806296	−1.067750	−1.348344
0.60	−0.684570	−0.757346	−0.831754	−1.085879	−1.360226
0.80	−0.713870	−0.782004	−0.852470	−1.099115	−1.369705
1.00	−0.734226	−0.797097	−0.869746	−1.110066	−1.377115

Γ	$\kappa = 3.0$	$\kappa = 3.6$	$\kappa = 4.0$	$\kappa = 4.6$	$\kappa = 5.0$
0.00	−1.500000	−1.800000	−2.000000	−2.300000	−2.500000
0.10	−1.517696	−1.815104	−2.009731	−2.309720	−2.509010
0.20	−1.527809	−1.821103	−2.018270	−2.315081	−2.512796
0.40	−1.540813	−1.831725	−2.027327	−2.321292	−2.520736
0.60	−1.549763	−1.838610	−2.033013	−2.327181	−2.523305
0.80	−1.558136	−1.843731	−2.037149	−2.329887	−2.525945
1.00	−1.563017	−1.847809	−2.040283	−2.332756	−2.528765

Table 5.6: Excess energy per particle u/Γ at small Γ values ($N = 500$). Note that $u/\Gamma \to -\kappa/2$ as $\Gamma \to 0$.

κ	$f_1(\kappa)$
0.00	−0.436765
0.20	−0.449484
0.40	−0.480913
0.60	−0.528365
0.80	−0.586650
1.00	−0.654089
1.20	−0.730380
1.40	−0.810280
2.00	−1.070980
2.60	−1.350351
3.00	−1.542363
3.60	−1.832581
4.00	−2.027406
4.60	−2.322260
5.00	−2.519954

Table 5.7: $f_1(\kappa) = f_{\rm fluid}(\kappa, 1) - f_{\rm ideal}(1)$ defined by Eq. (5.12).

where 3/2 is the harmonic component, and the power series in Γ^{-1} represents the anharmonic terms. From a least squares fit of the bcc solid phase data given in Table 5.3(a) over the dual independent variables κ and Γ, we obtain

$$A_1(\kappa) = 9.13 + 4.37\kappa^2 \tag{5.19}$$

$$A_2(\kappa) = 1526 + 479\kappa^2 \tag{5.20}$$

for bcc lattices with $\kappa \leq 1$.

For $\kappa > 1$, we do not use Taylor-series expansions in κ for the coefficients, as defined by Eqs. (5.13)–(5.20). Instead we fit the potential energy functional forms, Eqs. (5.10) and (5.18), to the simulation data for each κ value separately. For $\kappa > 1$, the u/Γ values for the fluid phase, bcc solid phase, and fcc solid phase are given in Tables 5.3(b), 5.4(b), and 5.5(b), respectively. Least squares fitting of the functional forms to these data ($\Gamma \geq 1$) yields the coefficient values shown in Tables 5.8 and 5.9. Figure 5.1 present examples of least-squares

κ	a	b	c	d
1.2	−1.041816	0.522733	−0.305649	0.026740
1.4	−1.090801	0.514325	−0.344195	0.049258
2.0	−1.270571	0.442193	−0.382900	0.100506
2.6	−1.489806	0.366308	−0.411566	0.159826
3.0	−1.651703	0.312503	−0.394913	0.173963
3.6	−1.910871	0.239251	−0.362000	0.195448
4.0	−2.091363	0.182517	−0.257154	0.131096
4.6	−2.370109	0.139276	−0.232476	0.142315
5.0	−2.559633	0.115580	−0.215437	0.149102

Table 5.8: Fluid fitting parameters a, b, c, and d defined by Eq. (5.10). For $\kappa \leq 1.0$, these parameters are given as functions of κ by Eqs. (5.14)–(5.17). Note that $\delta a(\kappa)$ in Eq. (5.14) is defined as $\delta a(\kappa) = a(\kappa) - E_{\rm bcc}(\kappa)$.

fitting to the fluid and solid phases at $\kappa = 3.0$. The dotted lines represent the ranges of fitting uncertainties, which will be discussed in the next section.

5.4. Simulation results and phase diagram

For a given κ, the intersection of the free energies of the fluid and solid phases determined the fluid–solid phase transition (i.e., melting or freezing) Γ value, which we denote $\Gamma_{\rm m}$. The free energies are evaluated from Eqs. (5.7)–(5.18) as well as the fitting parameters listed in Tables 5.8 and 5.9. Table 5.10 shows $\Gamma_{\rm m}$ values at the fluid–bcc solid free-energy intersection whereas Table 5.11 shows $\Gamma_{\rm m}$ values at the fluid–fcc solid free-energy intersection . The dimensionless temperatures $\mathcal{T}$ listed in these tables is defined by Eq. (5.21) below. As will be discussed later, along the fluid–solid phase transition boundary, the free energy of the bcc phase is lower than that of the fcc phase for $\kappa \lesssim 4.3$. Therefore $\Gamma_{\rm m}$ and $\mathcal{T}_{\rm m}$ for $2.6 \leq \kappa \leq 4.0$ in Table 5.10 are not on the phase boundary curve.

Similarly the intersection of the bcc and fcc solid free-energies given by Eq. (5.7) yields Γ values at the bcc–fcc phase transition, which we denote $\Gamma_{\rm s}$. The values of $\Gamma_{\rm s}$, together with

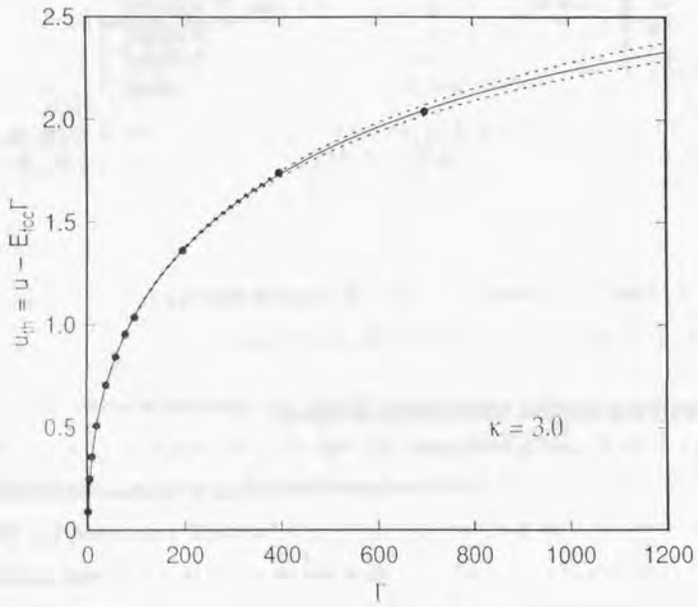

Figure 5.1: (a) The thermal potential energy in the fluid phase, defined by $u_{th} = u - E_{fcc}\Gamma$, at $\kappa = 3.0$. The filled circles are data obtained from Table 5.3(b). The solid line is the least-squares fit to the data; the dotted lines represent the range of uncertainties due to the coefficient $a = 1.651703 \pm 0.000037$.

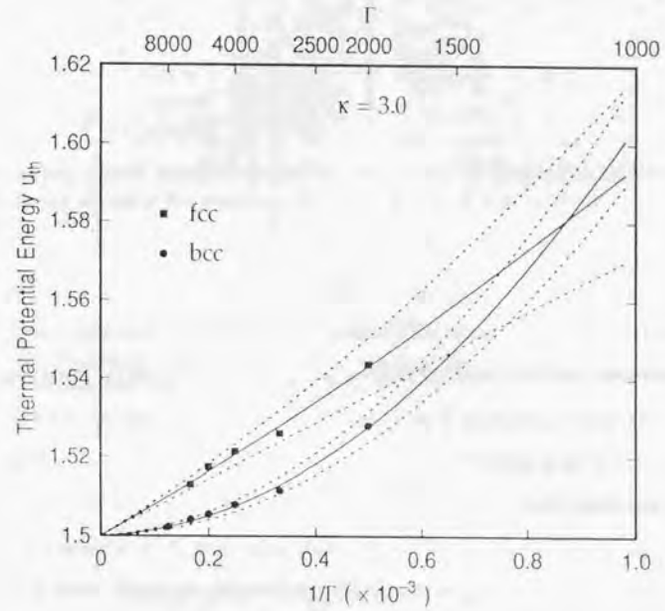

Figure 5.1: (b) The thermal potential energies at $\kappa = 3.0$, defined by $u_{th} = u - E_{bcc}\Gamma$ for the bcc lattice and $u_{th} = u - E_{fcc}\Gamma$ for the fcc lattice. The filled circles are bcc data obtained from Table 5.4(b), and the filled squares are fcc data obtained from 5.5(b). The solid lines are the least-squares fits to these data. The dotted lines represent the ranges of uncertainties due to the coefficients $A_1 = 5.344 \pm 3.462$ and $A_2 = 99742.3 \pm 8643.8$ for the bcc lattice, and $A_1 = 77.822 \pm 6.653$ and $A_2 = 16822.5 \pm 16374.6$.
for the fcc lattice.

κ	A_1^{bcc}	A_2^{bcc}	A_1^{fcc}	A_2^{fcc}
1.2	15.42	2042.56	21.13	1712.24
1.4	16.12	3398.78	17.87	4735.20
2.0	23.53	4526.98	37.68	414.70
2.6	30.16	24377.67	67.44	5735.30
3.0	5.34	99742.33	77.82	16822.48
3.6	−45.39	392246.46	91.35	151465.97
4.0	−175.68	1067933.16	25.63	904495.83
4.6	—	—	−114.88	2828867.93
5.0	—	—	−1069.10	27561540.63

Table 5.9: Solid fitting parameters A_1 and A_2 for bcc and fcc Yukawa lattices defined by Eq. (5.18). For $\kappa \leq 1.0$, $A_1(\kappa)$ and $A_2(\kappa)$ for bcc Yukawa lattices are given by Eq. (5.19) and (5.20).

the dimensionless temperatures $\mathcal{T}$ at the solid–solid phase transition, are listed in Table 5.12.

As mentioned earlier, we have used the dual-value (Γ and κ) fitting of the free energies for $\kappa \leq 1.0$ and the single-value (i.e., Γ only) fitting for each κ that is larger than 1. To check the consistency of this approach, we also applied the single-value fitting method to the cases $\kappa \leq 1$, and found that it gave Γ_m values very similar to those from the dual-value fit. For example, Γ_m for $\kappa = 1.0$ obtained from the single-value fit is 217.9, whereas Γ_m from the dual-value fit is 217.4. Similarly, for the OCP case ($\kappa = 0$), the single-value fit gives 171.2 while the dual-value fit gives 171.8. These values are in very good agreement with most recent Γ_m estimates for the OCP system.[30,41,42]

First we focus on the phase diagram for small κ, where no MD or MC simulations were performed previously except for the case of $\kappa = 0$ (OCP). Figure 5.2 shows the phase diagram in the κ–Γ plane for $\kappa \leq 1.5$. The filled circles represent the data points given in Table 5.10 and the solid curve is the least-squares fit given by

$$\Gamma_m = 171.8 + 42.46\,\kappa^2 + 3.841\,\kappa^4 \qquad \text{for } \kappa \leq 1.4.$$

The bcc–fcc phase transition curve given in Table 5.12 is off-scale in Fig. 5.2.

κ	Γ_m	$\mathcal{T}_m$
0.0	171.8	2.240×10^{-3}
0.2	173.5	2.267×10^{-3}
0.4	178.6	2.332×10^{-3}
0.6	187.1	2.425×10^{-3}
0.8	199.6	2.535×10^{-3}
1.0	217.4	2.647×10^{-3}
1.2	243.3	2.736×10^{-3}
1.4	268.8	2.907×10^{-3}
2.0	440.1	3.095×10^{-3}
2.6	758.9	3.420×10^{-3}
3.0	1185	3.498×10^{-3}
3.6	2378	3.682×10^{-3}
4.0	3837	3.851×10^{-3}

Table 5.10: Transition values of Γ and $\mathcal{T}$ at the fluid–bcc solid phase boundary. The normalized temperature $\mathcal{T}$ is defined by Eq. (5.21)

κ	Γ_m	$\mathcal{T}_m$
2.6	779.4	3.330×10^{-3}
3.0	1216	3.408×10^{-3}
3.6	2422	3.614×10^{-3}
4.0	3862	3.827×10^{-3}
4.6	8609	3.881×10^{-3}
5.0	1.506×10^4	3.888×10^{-3}

Table 5.11: Transition values of Γ and $\mathcal{T}$ at the fluid–fcc solid phase boundary. Note that values only for $\kappa = 4.6$ and 5.0 represent the actual fluid–solid phase-transition points. The normalized temperature $\mathcal{T}$ is defined by Eq. (5.21)

κ	Γ_s	$\mathcal{T}_s$
1.066	∞	0.000
1.2	5070	1.313×10^{-4}
1.4	2325	3.361×10^{-4}
2.0	1228	1.109×10^{-4}
2.6	1273	2.040×10^{-4}
3.0	1634	2.537×10^{-4}
3.6	2884	3.036×10^{-4}
4.0	4185	3.531×10^{-4}

Table 5.12: Transition values of Γ and $\mathcal{T}$ at the bcc–fcc phase boundary. The normalized temperature $\mathcal{T}$ is defined by Eq. (5.21)

Some earlier studies[22,23,31–33] have used normalizations different from Eq. (5.4) to represent the particulate temperature T and the Debye screening length λ_D. For example, one may use $\rho = n^{-1/3}$ instead of the Wigner-Seitz radius a as the length unit, and define $K = \rho/\lambda_D$. Kremer, Robbins, and Grest[22] normalized the temperature T by the typical phonon energy of the fcc Yukawa lattice according to

$$\mathcal{T} = \frac{kT}{m\omega_E^2\rho^2}, \tag{5.21}$$

where ω_E is the Einstein frequency for the fcc Yukawa lattice, defined by

$$\omega_E^2 = \frac{2k_D^2}{3m}\sum_{i\neq j}\phi(|\mathbf{r}_i - \mathbf{r}_j|)$$

with all particles situated at fcc lattice sites. The Einstein frequency is related to the Madelung energy in units of $Q^2/4\pi\varepsilon_0 a$, i.e., $E_{fcc}(\kappa)$, by

$$\frac{m\omega_E^2 a^2}{Q^2/4\pi\varepsilon_0 a} = \frac{2}{3}\kappa^2\left[E_{fcc}(\kappa) + \frac{3}{2\kappa^2} + \frac{\kappa}{2}\right]. \tag{5.22}$$

It follows from Eqs. (5.1), (5.21), and (5.22) that the dimensionless temperature $\mathcal{T}$ is related to κ and Γ as

$$\mathcal{T} = \frac{1}{\Gamma}\left(\frac{3}{4\pi}\right)^{\frac{2}{3}}\left[\frac{2}{3}\kappa^2 E_{fcc}(\kappa) + \frac{\kappa^3}{2} + 1\right]^{-1} \tag{5.23}$$

In the OCP limit of $\kappa \to 0$, Eq. (5.22) evidently becomes 1 and $\mathcal{T} \to (3/4\pi)^{2/3}/\Gamma$. The Einstein phonon energies for the fcc Yukawa lattice in units of $Q^2/4\pi\varepsilon_0\rho$, i.e.,

$$\Omega^2 = \frac{m\omega_E^2\rho^2}{Q^2/4\pi\varepsilon_0\rho} = 4\pi\left(\frac{\omega_E}{\omega_p}\right)^2 \tag{5.24}$$

are given in Table 5.13.

Figure 5.3 shows the fluid–solid (bcc) and solid–solid (bcc–fcc) phase transition curves in the κ–$\mathcal{T}$ phase space for $\kappa \leq 1.5$. Alternative variable K $[= (4\pi/3)^{1/3}\kappa \approx 1.61199\kappa]$ is also listed. Here filled circles indicate the fluid–solid phase transition points given in Table 5.10 and filled triangles indicate the bcc-fcc phase transition points given in Table 5.12. The solid curve is the least-squares fit to the $\mathcal{T}_m$ values given by

$$\mathcal{T}_m = 0.002240 + 0.000181\,\kappa + 0.000209\,\kappa^2 \qquad \text{for } \kappa \leq 1.4 \tag{5.25}$$

The broken line is the fluid–solid phase boundary line estimated by Stevens and Robbins,[32]

$$\mathcal{T}_m = 0.0022 + 0.00022\,K\,, \tag{5.26}$$

which is an extrapolation of their simulation data for $K > 2.0$, matched linearly to the OCP phase-transition value obtained by Stringfellow, DeWitt, and W. L. Slattery.[28] This linear extrapolation is in reasonable agreement with our results within this domain ($\kappa \leq 1.5$). The dotted line represents the bcc–fcc phase transition curve obtained from the quasi-harmonic theory (lattice dynamic simulation),[23] which are in excellent agreement with our simulation results for $\kappa = 1.2$ and 1.4..

Figure 5.4 is the extension of Fig. 5.3, for κ up to 5.0. Here, filled circles indicate the fluid–bcc solid phase transition (from Table 5.10), filled squares identify the fluid–fcc solid phase transition (from the last two rows of Table 5.11), and filled triangles correspond to the bcc-fcc phase transition (from Table 5.12). As indicated in the earlier studies,[22,23] the fluid–solid phase transition curve $\mathcal{T}_m$ depends on κ almost linearly for larger κ. The linear

κ	Ω^2
0.0	4.18879020
0.2	4.09942706
0.4	3.87048594
0.6	3.55258586
0.8	3.18604083
1.0	2.80173848
1.2	2.42225060
1.4	2.06308014
1.6	1.73394886
1.8	1.44004234
2.0	1.18314736
2.2	0.96264058
2.4	0.77630810
2.6	0.62099345
2.8	0.49308756
3.0	0.38887907
3.2	0.30478987
3.4	0.23751987
3.6	0.18412321
3.8	0.14203782
4.0	0.10908012
4.2	0.08342179
4.4	0.06355299
4.6	0.04824326
4.8	0.03649976
5.0	0.02752873

Table 5.13: Normalized squares of Einstein frequencies defined by Eq. (5.24).

least-squares fit of the $\mathcal{T}_m$ values (given in Table 5.10 and the last two rows of Table 5.11) becomes

$$\mathcal{T}_m = 0.002491 + 0.000312\,\kappa \qquad \text{for } 1.2 \le \kappa \le 5.0\,. \tag{5.27}$$

In Fig. 5.4, the fluid-solid phase transition points $\mathcal{T}_m$ are fitted by the quadratic polynomial of Eq. (5.25) for $\kappa \le 1$ and the linear function of Eq. (5.27) for $\kappa \ge 2.6$. As a guide to the eye, these two functions are smoothly connected by a cubic spline function over $1 \le \kappa \le 2.6$:

$$\begin{aligned}\mathcal{T}_m = {} & 0.00330220 - 0.00031200 \cdot (2.6 - \kappa) \\ & -0.00002336 \cdot (2.6 - \kappa)^2 - 0.00002764 \cdot (2.6 - \kappa)^3 \\ & \text{for } 1.0 \le \kappa \le 2.6\,.\end{aligned} \tag{5.28}$$

The bcc-fcc phase transition curve is also fitted by the following functions:

$$\mathcal{T}_s = 0.00096377 \cdot (\kappa - 1.066) \qquad \text{for } 1.066 \le \kappa \le 1.2 \tag{5.29}$$

$$\begin{aligned}\mathcal{T}_s = {} & 0.00195631 - 0.00119860 \cdot (2.6 - \kappa) \\ & -0.00039599 \cdot (2.6 - \kappa)^2 + 0.00022850 \cdot (2.6 - \kappa)^3 \\ & \text{for } 1.2 \le \kappa \le 2.6\,.\end{aligned} \tag{5.30}$$

$$\mathcal{T}_s = 0.001352 \cdot (\kappa - 1.066) - 0.000050 \cdot (\kappa - 1.066)^2 \tag{5.31}$$

$$\text{for } 2.6 \le \kappa \le 4.2755\,. \tag{5.32}$$

Here Eq. (5.31) represents the quadratic least-square fit of $\mathcal{T}_s$ over $1.066 \le \kappa \le 4.0$ given in Table 5.12. Although data points near $\kappa = 1.066$ are also used to obtain Eq. (5.31), it does not reproduced the $\mathcal{T}_m$ values near $\kappa = 1.066$ very well. As mentioned earlier, our simulation results agree with the quasi-harmonic calculation, which is known to be accurate near $\kappa = 1.066$. Therefore, in Fig. 5.4, we have used Eq. (5.31) only for $\kappa \ge 2.6$ as the fitting curve. For $1.066 \le \kappa \le 1.2$, we have used a linear fit based on the quasi-harmonic theory, i.e., Eq. (5.29). The cubic spline fucntion given in Eq. (5.30) is used to smoothly connect

Eq. (5.29) and Eq. (5.31) over $1.2 \leq \kappa \leq 2.6$. The point where the three phases (fluid, bcc and fcc lattices) meet — i.e., the triple point — is the intersection of Eqs. (5.27) and (5.31), which is given as $\kappa = 4.28$ ($K = 6.90$) and $\mathcal{T} = 0.0038$.

It is not easy to accurately estimate the magnitude of errors in the phase-transition boundary curves. There may be several possible sources of uncertainties. In the case of large Γ, for example, the potential energy u is very close to the Madelung energy u_∞ and the numerical value for the difference $u_{th} = u - u_\infty$, which is used to determine the phase diagram, has fewer meaningful digits. Furthermore, if κ and Γ are large (and therefore the interparticle interaction is weak and the system has a low thermal energy), it takes longer (in terms of the time unit $\sqrt{3}\omega_p^{-1}$) for the system to attain the thermal equilibrium. Consequently, the measured energy data are prone to errors values due to numerical averaging over finite time intervals.

Therefore we now take a pragmatic approach to estimate the uncertainties associated with the phase boundaries. Assuming that the measured energy values have uniform errors of order given by the square root of the sample variance, one can estimate the uncertainties of the fitting parameters.[30,44] For example, for the bcc solid phase at $\kappa = 3.0$, we obtain $A_1 = 5.344 \pm 3.462$ and $A_2 = 99742.3 \pm 8643.8$, the numbers after $\pm$ representing the range of the uncertainties [see Fig 5.1(b)]. In the fluid phase, it follows from Eq. (5.10), that the energy value u, is most sensitive to variation in the coefficient $a(\kappa)$ for large Γ. Its uncertainty under the same assumption is $a = -1.651703 \pm 0.000037$ [see Fig 5.1(a)].

If we choose the most probable values of a, b, c, and d, as given in Table 5.8 (i.e., no variation), and varies A_1 and A_2 as indicated above, the range of uncertainties for the melting point becomes $3.468 \times 10^{-3} < \mathcal{T}_m < 3.529 \times 10^{-3}$ at $\kappa = 3.0$. On the other hand, if we use the most probable values $A_1 = 5.344$ and $A_2 = 99742.3$ (as given in Table 5.9) and vary a in the range -1.651703 ± 0.000037, the uncertainty in the melting point at $\kappa = 3.0$ becomes $3.274 \times 10^{-3} < \mathcal{T}_m < 3.719 \times 10^{-3}$. The error bar on the melting curve in Fig. 5.4 represents

the latter range of uncertainty — the larger of the two.

Similarly, for the solid phases at $\kappa = 3.0$, we obtain $A_1 = 5.344 \pm 3.462$, $A_2 = 99742.3 \pm 8643.8$ for the bcc lattice and $A_1 = 77.822 \pm 6.653$ and $A_2 = 16822.5 \pm 16374.6$ for the fcc lattice [see Fig 5.1(b)]. If we choose the most probable values of A_1 and A_2 for the bcc phase and vary A_1 and A_2 for the fcc phase, and vice versa, the range of $\mathcal{T}_s$ at $\kappa = 3.0$ is found to be $2.322 \times 10^{-3} < \mathcal{T}_s < 2.901 \times 10^{-3}$. The error bar on the bcc-fcc phase transition curve in Fig. 5.4 represents this range.

Figure 5.5 shows the same data as those in Fig. 5.4, plotted in the κ–Γ phase plane. The phase boundaries Γ_m and Γ_s are also converted from $\mathcal{T}$ to Γ, using Eq. (5.23) and the fitting curves used in Fig. 5.4. The error bars at $\kappa = 3.0$ in Fig. 5.4. are also plotted in Fig 5.5; these errors are less prominent due to the logarithmic scale for Γ. The triple point is given by $\Gamma = 5.6 \times 10^3$ at $\kappa = 4.28$ ($K = 6.90$). Both the fluid-solid and bcc-fcc phase transitions are of first order.[1,2,23,40] The entropy per particle $s = S/Nk$ (with $F = U - ST$) is related to the free energy per particle f through $u - s = f$. Therefore the entropy change per particle Δs at a phase boundary is equal to the potential energy change par particle Δu since $\Delta f = 0$. Using this relation at the phase boundaries, one can directly calculate Δs from MD simulations. For example, at $\kappa = 1.2$, we obtain $\Delta s = 0.75$ at the fluid-solid phase boundary and $\Delta s = 0.052$ at the bcc-fcc phase boundary.

5.5. Comparison with earlier work

In Fig. 5.6, we compare our MD simulation results with those from earlier MD and MC simulations, based on different methods.[22,23,31-33] These earlier MD and MC simulations do not include the infinite sum of periodic boundary conditions, i.e., the second term of Eq. (5.2), and are thus valid only in the larger κ regime (e.g., $\kappa \gtrsim 1$). In Fig. 5.6, the linear fit given by of Eq. (5.27) is extrapolated to $\kappa = 8.0$. The filled symbols and solid lines are the same as those used in Fig. 5.4. The crosses ($\times$), together with the error bars,

are the fluid–solid phase boundary points obtained by Meijer and Frenkel.[31] These values were obtained from a modified Frenkel–Ladd lattice coupling method[46] and MC simulation for systems of 256 or fewer particles. The error bars show the statistical errors. The open rectangles (□), triangles (△) and diamonds (◇) indicate stable fluid, bcc, and fcc states, respectively, obtained by Stevens and Robbins.[32] These authors used MD simulations and observed the time evolution of the state, starting from fluid–solid coexistent initial conditions (phenomenological melting tests) — the number of particles used in their simulation are 432 for bcc lattices and 500 for fcc lattices.

The bcc–fcc phase boundary obtained from the lattice dynamic calculations (quasi-harmonic theory) by Robbins, Kremer and Grest[23] is plotted as the dashed line in Fig. 5.6. As we noted earlier, this becomes exact in the low temperature limit. The dotted line is the bcc–fcc phase boundary, also obtained by Robbins, Kremer and Grest,[23] based on MD simulations and the energy-distribution function method[23,43]:

$$\mathcal{T}_s = 0.0006 \cdot (K - 1.72) + 0.00018 \cdot (K - 1.72)^2 . \tag{5.33}$$

The linear term of this equation is directly taken from the lattice dynamic calculations. The second term is determined by a quadratic fit to their bcc–fcc phase transition data. Using this bcc–fcc phase boundary, Stevens and Robbins estimated[32] the triple point — i.e., the boundary point of fluid, bcc and fcc phases, which is given as the intersection of the melting phase boundary of Eq. (5.26) and the bcc-fcc phase boundary of Eq. (5.33) — as $\kappa = 2.85$ ($K = 4.59$) and $\mathcal{T} = 0.0032$ ($\Gamma = 1.0 \times 10^4$). This triple point is located at much smaller κ than that obtained in this study.

DuPont, Moulinasse, Ryckaert, and Baus[33] used MC simulation and Frenkel–Ladd lattice coupling method[45] to evaluate the solid free energies. Using the free energies of the fluid phase obtained by Meijer and Frenkel,[31] DuPont *et al.* obtained a fluid–bcc boundary point, a bcc–fcc phase boundary point, and the triple point, denoted respectively by the open circle

(○), plus (+), and nabla (▽) in Fig. 5.6. This triple point — at $\kappa = 4.19$ ($K = 6.75$) and $\mathcal{T} = 0.0034$ ($\Gamma = 5.6 \times 10^3$) — is close to the one obtained in this study, i.e., $\kappa = 4.28$ ($K = 6.90$) and $\mathcal{T} = 0.0038$ ($\Gamma = 5.6 \times 10^3$).

It is interesting to note that the triple-point κ and Γ values obtained by DuPont *et al.* and in the present study are very close (within 2%), although the $\mathcal{T}$ values differ by over 10%. This is because $\mathcal{T}$ is a sensitive function of κ when $\kappa \gtrsim 1.0$, as shown below. From Eq. (5.23), one can write

$$\frac{d\mathcal{T}}{\mathcal{T}} = -\frac{d\Gamma}{\Gamma} + \frac{\kappa}{\mathcal{T}}\frac{\partial \mathcal{T}}{\partial \kappa}\frac{d\kappa}{\kappa} .$$

It follows from Eq. (5.23) that the coefficient of the second term $(\kappa/\mathcal{T})(\partial\mathcal{T}/\partial\kappa)$ above is a function of only κ, independent of Γ. The values of this coefficient are 2.02, 5.32, 8.88 and 12.5 for $\kappa = 2.0$, 4.0, 6.0 and 8.0, respectively. For example, if $\kappa = 4.0$, a 2% error in the κ value results in more than 10% error in the corresponding $\mathcal{T}$ value for a given Γ.

The fluid–solid phase transition temperatures obtained in this study are systematically higher (by about 5% in $\mathcal{T}$) than those obtained by Meijer and Frenkel. With their modified Frenkel–Ladd lattice coupling method,[46] Meijer and Frenkel obtained the Gibbs free energy by integrating a polynomial fit to the density–pressure data obtained from MC simulations. In addition to this different methodology, other factors may have contributed to the systematic discrepancy. First, the MC simulations by Meijer and Frenkel employed relatively small numbers of particles ($N \leq 256$). Second, Meijer and Frenkel assumed that the solid phase at their data points of $\kappa = 3.30$ ($K = 5.33$) and $\kappa = 4.20$ ($K = 6.77$) is fcc. However, our simulations, as well as those by DuPont *et al.*,[33] indicate that this phase is actually bcc.

The stable fluid phase data presented by Stevens and Robbins, which are considered to give an upper bound of the fluid–solid transition phase, lie more or less on or above our fitted fluid–solid phase boundary, suggesting good agreement with our data. Only two data points given by Stevens and Robbins — those at $\kappa = 2.067$ and 2.597 ($K = 3.332$ and 4.186) —

are slightly lower than our fitted phase-transition curve. These two data are obtained from MD simulations of a system of 432 particles, with the potential truncation at a radius equal to 3ρ, whereas we have used MD simulations of 686-particle systems for bcc lattices and 500-particle systems for fluid phases with no potential truncation. To determine the stable phase, Stevens and Robbins ran MD simulations starting from two-phase states (equally divided fluid and solid phases) and observed their time evolutions. If the difference between the free energies of the two phases is very small, which is the case near the transition point, the evolution of MD simulation may be sensitively dependent on the shape of the simulation box, number of particles, initial perturbations, and the potential truncation radius.

The two fluid-solid boundary points obtained by DuPont, Moulinasse, Ryckaert, and Baus[33] [denoted by the open circle (○) and nabla (▽) in Fig. 5.6; the latter is also the triple point] seem rather scattered if one believes that the melting temperature $\mathcal{T}_m$ increases linearly with κ. In the lattice-coupling calculations by DuPont *et al.*, the free energy is obtained by integrating the energy along an isotherm. Hence, the actual temperature (or equivalently Γ) is fixed, and κ is computed for each phase boundary point [which is opposite to our method: we fix κ values and determine corresponding phase-transition temperature (or Γ) values.] As discussed above, however, small errors in κ can result in $\mathcal{T}$ large errors. Indeed DuPont *et al.* have obtained $\Gamma = 1.7 \times 10^3$ and 5.6×10^3 at $\kappa = 3.38$ and 4.19 as fluid-solid boundary points. Our κ estimates on the fluid-solid boundary [from Eq. (5.27) converted to Γ] for $\Gamma = 1.7 \times 10^3$ and 5.6×10^3 are $\kappa = 3.30$ and $\kappa = 4.28$, which are within 2.5% of the κ values estimated by DuPont *et al.* This small difference in κ incurs a discrepancy of about 10% in $\mathcal{T}_m$ at the triple point.

The bcc-fcc phase boundary point obtained by DuPont *et al.*[33] [denoted by a plus (+) in Fig. 5.6] is in excellent agreement with the bcc-fcc phase boundary curve estimated in this study, while the bcc-fcc phase transition temperatures obtained by Robbins, Kremer and Grest[43] are much higher (the dotted line in Fig. 5.6). Consequently, the triple point

suggested by Stevens and Robbins[32] is located at much smaller κ than that obtained in this study, as previously noted. Robbins, Kremer and Grest used the energy-distribution-function method[23,43] to obtain the free energy difference between fcc and bcc phases for given κ and $\mathcal{T}$. To determine small differences between the free energies near the bcc-fcc boundary, one needs accurate statistics for a sampling of the energy histogram in this method. It is not clear from Ref. 23 that the statistics were adequate for an accurate estimation of these values. One example given in Ref. 23 shows that the difference in the free energies at $\kappa = 3.05$ ($K = 4.92$) and $\mathcal{T} = 2.24 \times 10^{-3}$ ($\Gamma = 1.97 \times 10^3$) is $0.03 k_B T$. Our MD calculations show, however, that the difference is $0.014 k_B T$ at $\kappa = 3.00$ (note the slight difference in κ) and $\mathcal{T} = 2.24 \times 10^{-3}$, which is different by a factor of about 2. Since the measured potential energies for $\Gamma \gtrsim 2000$ give an excellent fit to the quadratic form in Eq. (5.18), the error in our free-energy estimate due to the extrapolation form of Eq. (5.18) at this position in the phase space (i.e., $\kappa = 3.00$ and $\mathcal{T} = 2.24 \times 10^{-3}$) is expected to be very small.

Stevens and Robbins[32] showed that their MD simulation starting from a mixed state of fluid and fcc phases evolved to the fcc phase at $\kappa = 3.604$ ($K = 5.809$) and $\mathcal{T} = 3.429 \times 10^{-3}$, which is indicated as an open diamond in Fig. 5.6. However, they do not seem to claim that the bcc phase is actually more unstable than the fcc phase at this data point. [At $\kappa = 2.779$ ($K = 4.479$) and $\mathcal{T} = 3.198 \times 10^{-3}$, the authors of Ref. 32 show that two runs converge to different lattices, suggesting that both the bcc and fcc phases are stable.] It is not clear from Ref. 32 that their phenomenological melting test can distinguish such small differences in the free energy near the phase boundary.

To summarize, we believe that the triple point obtained in this study — which is very close to the one obtained by DuPont *et al.* — is more accurate than that suggested by Stevens and Robbins. It may be of interest to compare the different methods mentioned above, using data from the same MD or MC simulations. In this manner, one could ascertain whether the discrepancy arises from differences in the methodologies of evaluating free energies or from

the intrinsic accuracy of the simulation data. Figure 5.7 plot the same data as for Fig. 5.6, in the κ–Γ plane. The error bars are omitted in Fig. 5.7 for simplicity. With this logarithmic scale for Γ, the differences among the data of the various authors are hardly discernible.

5.6. Summary

We have obtained the fluid–solid phase boundary of the Yukawa system for $\kappa \leq 5$, including the weakly screened regime ($0 \leq \kappa \leq 1.0$). This phase transition is of first order. Unlike earlier MD or Monte Carlo (MC) simulations, in which interparticle forces were computed by pairwise summation over particles within some cut-off radius, our MD simulations use interparticle potentials summed over all particle pairs, including periodic images of particles residing in the cubical simulation box. Thus long-range particle interactions are accurately accounted for over the entire range of κ, including the unscreened (i.e., OCP) limit of $\kappa = 0$. Our MD simulation method thus fills the gap between earlier extensive studies of the OCP system and strongly-screened Yukawa systems. For strongly-screened Yukawa systems ($\kappa \gtrsim 1$), the fluid–solid phase transition curve obtained here is in good agreement with those of the earlier studies.

We have also estimated the bcc–fcc phase boundary by the MD simulation method. This phase transition is also of first order. The transition temperatures $\mathcal{T}_s$ obtained are in excellent agreement with the results of quasi-harmonic theory[23] near $\kappa = 1.066$, the zero-temperature bcc–fcc phase transition point. The bcc–fcc phase transition point for a larger κ obtained in the recent study by DuPont, Moulinasse, Ryckaert, and Baus[33] is also in excellent agreement with our present results. The triple point (i.e., fluid–bcc–fcc phase boundary) is estimated to be $\kappa = 4.28$ ($K = 6.90$) and $\mathcal{T} = 0.0038$ ($\Gamma = 5.6 \times 10^3$), close to the one obtained by DuPont *et al.* We believe that the phase diagram presented here is the most accurate version currently available.

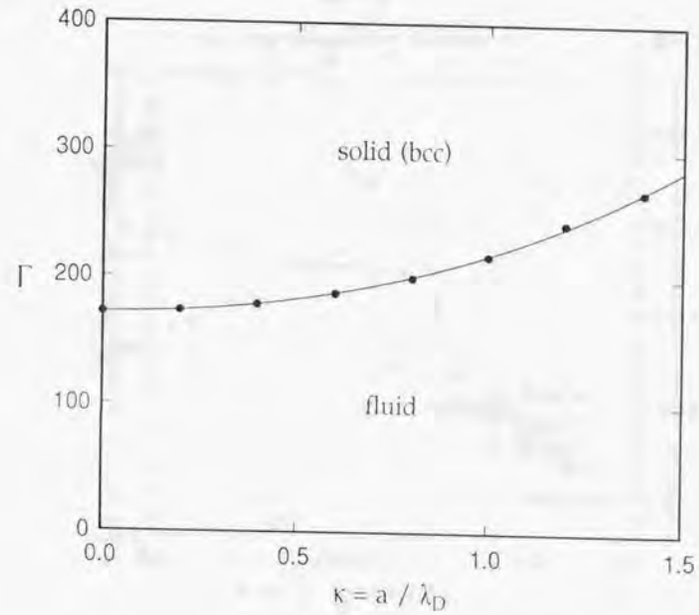

Figure 5.2: Phase diagram of Yukawa systems as a function of the dimensionless inverse screening length κ and the dimensionless inverse temperature Γ defined in Eq. (5.1). The solid circles are fluid–solid phase boundary points obtained from MD simulations (see Table 5.10) and the solid curve is their least-squares fit. Note that the fcc solid phase is off-scale in this figure.

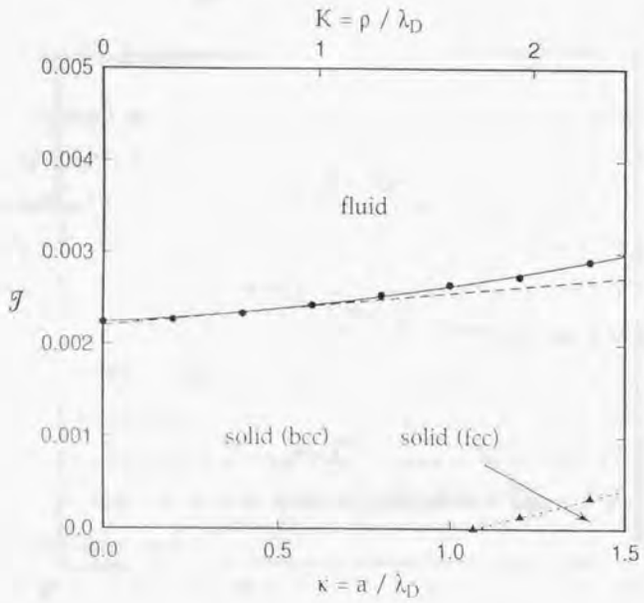

Figure 5.3: Phase diagram of Yukawa systems as a function of the dimensionless inverse screening length κ and the temperature $\mathcal{T}$ normalized by the Einstein phonon energy, defined by Eq. (5.21). $\mathcal{T}$ is related to Γ through Eq. (5.23). The filled circles are fluid–solid phase boundary points obtained from MD simulations (see Table 5.10) and the solid line represents their quadratic least-squares fit. The broken line is the phase boundary suggested by Stevens and Robbins in Ref. 32. The dotted line is the bcc–fcc phase boundary obtained by Robbins, Kremer, and Grest,[23] based on the quasi-harmonic theory. The filled triangles on the dotted line are bcc–fcc phase boundary points obtained from MD simulations (see Table 5.12).

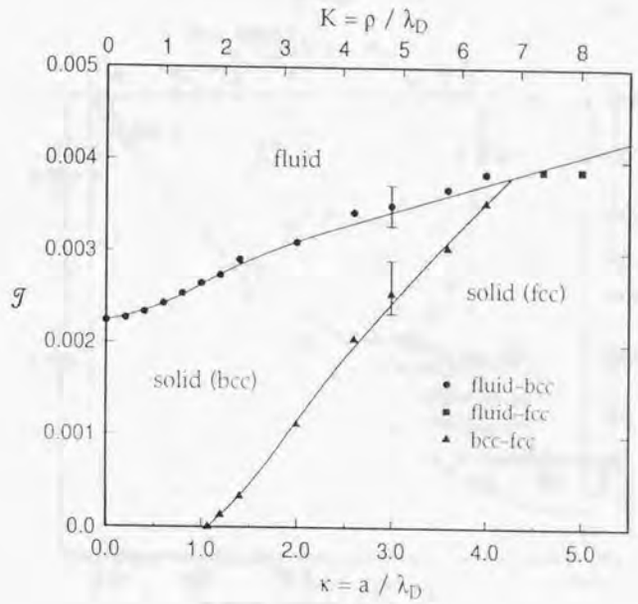

Figure 5.4: Phase diagram of Yukawa systems in the κ–$\mathcal{T}$ plane, including larger κ values. The filled circles are fluid–bcc phase boundary points ($\kappa < 4.3$), the filled squares are fluid–fcc phase boundary points ($\kappa > 4.3$), and the filled triangles are bcc–fcc phase boundary points (see Table 5.10, 5.11 and 5.12). The solid lines represent curves fitted to these data points.

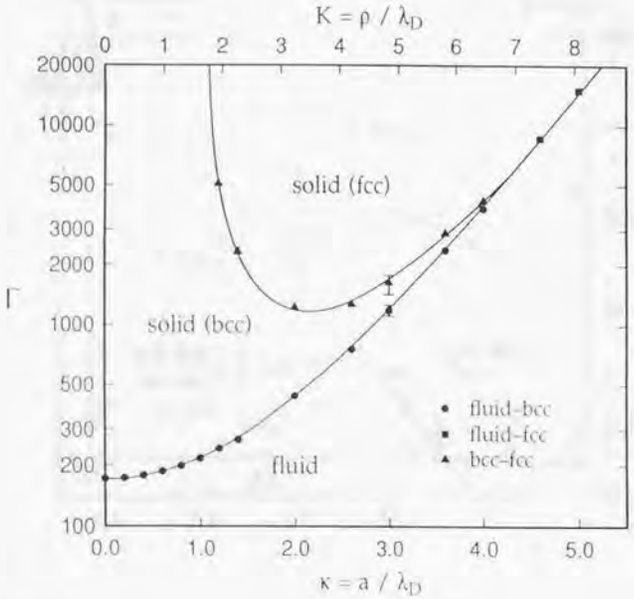

Figure 5.5: Phase diagram of Yukawa systems in the κ-Γ plane, including larger κ values. The filled circles and solid lines are the same as those used in Fig. 5.4, converted to Γ from $\mathcal{T}$ through Eq. (5.23).

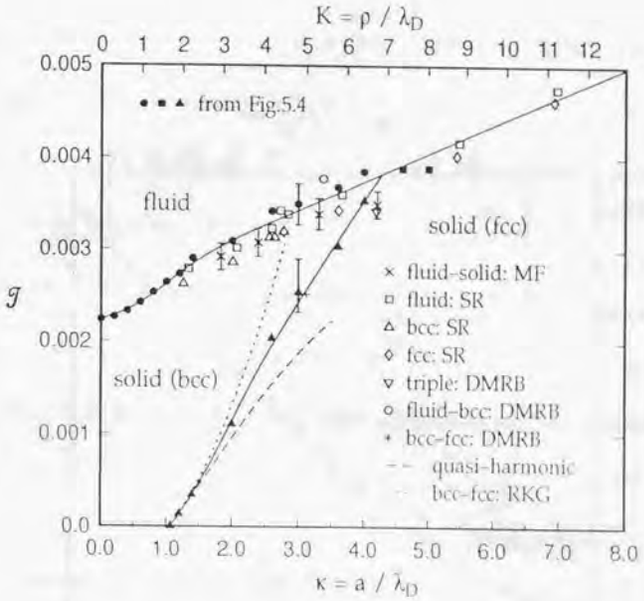

Figure 5.6: Phase diagram of Yukawa systems in the κ-$\mathcal{T}$ plane. The filled symbols and solid lines are from Fig. 5.4. The crosses ($\times$) with the error bars are fluid–solid phase boundary points obtained by Meijer and Frenkel.[31] The open rectangles ($\square$), triangles ($\triangle$) and diamonds ($\diamond$) indicate fluid, bcc, and fcc states, respectively, obtained by Stevens and Robbins.[32] The open circle ($\bigcirc$), plus ($+$), and nabla ($\bigtriangledown$) are a fluid–bcc boundary point, a bcc–fcc phase boundary point and the triple point, respectively, obtained by DuPont *et al.*[33] The dashed line is the bcc–fcc phase boundary obtained by Robbins *et al.*,[23] based on the quasi-harmonic theory (lattice dynamic calculations). The dotted line is also a bcc–fcc phase boundary obtained by these authors,[23] based on MD simulations and the energy-distribution function method.[23,43]

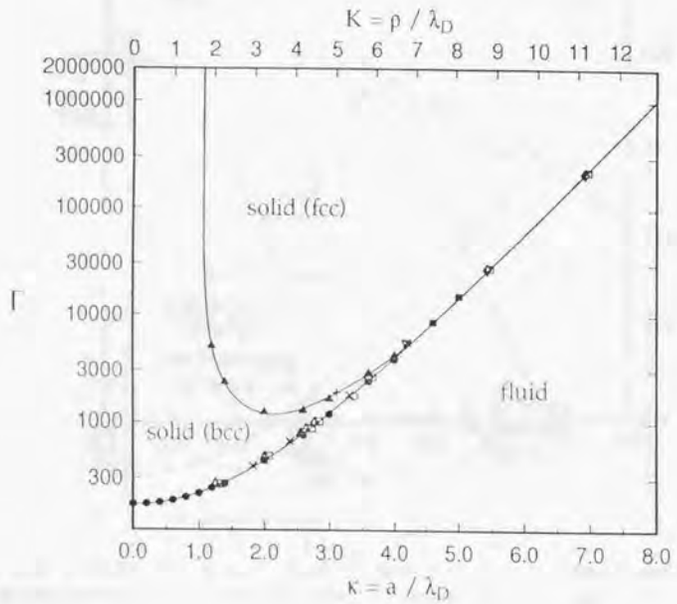

Figure 5.7: Phase diagram of Yukawa systems in the κ-Γ plane. All the symbols and lines are the same as in Fig. 5.4, converted from T to Γ through Eq. (5.23).

References

[1]S. Hamaguchi, R. T. Farouki, and D. H. E. Dubin, Phys. Rev. E (1997) (in press).

[2]S. Hamaguchi, R. T. Farouki, and D. H. E. Dubin, J. Chem. Phys. **105**, 7641 (1996).

[3]R. T. Farouki and S. Hamaguchi, J. Chem. Phys. **101**, 9885 (1994).

[4]H. Ikezi, Phys. Fluids **29**, 1764 (1986).

[5]R. T. Farouki and S. Hamaguchi, Appl. Phys. Lett. **61**, 2973 (1992).

[6]Y. Hayashi and K. Tachibana, Jpn. J. App. Phys. **33**, L804 (1994).

[7]H. Thomas, G. E. Morfill, V. Demmel, J. Goree, B. Feuerbacher, and D. Möhlmann, Phys. Rev. Lett. **73**, 652 (1994).

[8]J. H. Chu and I. Lin, Physica A **205**, 183 (1994).

[9]J. H. Chu and I. Lin, Phys. Rev. Lett. **72**, 4009 (1994).

[10]Th. Trottenberg, A. Melzer, A. Piel, Plasma Sources Sci. Technol. **4**, 450 (1995).

[11]B. Derjaguin, Trans. Faraday Soc. **36**, 203 (1940).

[12]E. J. Verwey and J. Th. G. Overbeek, Discuss. Faraday Soc. B **42**, 117 (1946).

[13]E. J. Verwey and J. Th. G. Overbeek, *Theory of the stability of lyophobic colloids*, Elsevier, Amsterdam (1948).

[14]W. Luck, M. Klier, and H. Wesslau, Ber Bunseges. Phys. Chem. **67**, 75 (1963).

[15]S. Hachisu, Y. Kobayashi, and A. Kose, J. Colloid and Interface Sci. **42**, 342 (1972).

[16]A. Kose, H. Ozaki, K. Takano, Y. Kobayashi, and S. Hachisu, J. Colloid and Interface Sci. **44**, 330 (1973).

[17]R. Williams and R. S. Crandall, Phys. Lett. **48A**, 225 (1974).

[18]J. M. Silva and B. J. Mokross, Phys. Rev. **B21**, 2972 (1980).

[19]M. Inoue and M. Wadati, J. Phys. Soc. Japan**50**, 1027 (1981).

[20]D. Hone, S. Alexander, P. M. Chaikin, and P. Pincus, J. Chem. Phys. **79**, 1471 (1983).

[21]W. H. Shih and D. Stroud, J. Chem. Phys. **79**, 6254 (1983).

[22]K. Kremer, M. O. Robbins, and G. S. Grest, Phys. Rev. Lett. **57**, 2694 (1986).

[23]M. O. Robbins, K. Kremer, and G. S. Grest, J. Chem. Phys. **88**, 3286 (1988).

[24]S. G. Brush, H. L. Sahlin, and E. Teller, J. Chem. Phys. **45**, 2102 (1966).

[25]J.-P. Hansen, Phys. Rev. A **8**, 3096 (1973).

[26]H. E. DeWitt, Phys. Rev. A **14**, 1290 (1976).

[27]M. Baus and J.-P. Hansen, Phys. Rep. **59**, 1 (1980).

[28]G. S. Stringfellow, H. E. DeWitt, and W. L. Slattery, Phys. Rev. A **41**, 1105 (1990).

[29]*Strongly Coupled Plasma Physics*, (F. J. Rogers and H. E. DeWitt, eds.), Plenum Press, New York (1986).

[30]R. T. Farouki and S. Hamaguchi, Phys. Rev. E **47**, 4330 (1993).

[31]E. J. Meijer and D. Frenkel, J. Chem. Phys. **94**, 2269 (1991).

[32]M. J. Stevens and M. O. Robbins, J. Chem. Phys. **98**, 2319 (1993).

[33]G. DuPont, S. Moulinasse, J. P. Ryckaert and M. Baus, Mol. Phys. **79**, 453 (1993).

[34]R. T. Farouki and S. Hamaguchi, J. Comp. Phys. **115**, 276 (1994).

[35]S. Hamaguchi and R. T. Farouki, J. Chem. Phys. **101**, 9876 (1994).

[36]A. A. Maradudin, E. W. Montroll, G. H. Weiss, and I. P. Ipatova, *Theory of Lattice Dynamics in the Harmonic Approximation*, 2nd Edition (Academic Press, New York, 1971).

[37]D. H. E. Dubin, private communication.

[38]D. H. E. Dubin and H. E. DeWitt, Phys. Rev. B **49**, 3043 (1994)

[39]S. Hamaguchi and R. T. Farouki, Phys. Rev. E**49**, 4430 (1994).

[40]Y. Rosenfeld, J. Chem. Phys. **103**, 9800 (1995).

[41]D. H. E. Dubin, Phys. Rev. A **42**, 4972 (1990).

[42]H. Nagara, Y. Nagata, and T. Nakamura, Phys. Rev. A **36**, 1859 (1987).

[43]A. Rahman and G. Jacucci, Nuovo Cimento D**4**, 357 (1984).

[44]P. R. Bevington, *Data Reduction and Error Analysis for the Physical Sciences* (McGraw-Hill, New York, 1969)

[45]D. Frenkel and A. J. C. Ladd, J. Chem. Phys. **81**, 3188 (1984).

[46]E. J. Meijer, D. Frenkel, R. LaSar, and A. J. C. Ladd, J. Chem. Phys. **92**, 7570 (1990).

Chapter 6

Summary

We have discussed some fundamental properties of charged grains (dust particles) immersed in plasmas. Such particles are typically "mesoscopic" — small on the macroscopic scale (e.g., the dimensions of the plasma) but significantly larger than molecular sizes. Since electrons have much higher mobility than ions in plasmas, particulates in plasmas are typically negatively charged due to the attachment of the electrons. Once negatively charged, such a particulate starts to attract ions and repel electrons, forming a Debye sheath around it in equilibrium. A Debye sheath thus shields the long-range Coulomb field of the charged particle at the center. The amount of charges on particulate surfaces are strongly influenced by relative distances among particles. The charging mechanism is summarized in in Chap. 1.

If a charged particle in a plasma is isolated from other particles, its dynamics is determined by the interaction between the particle and ambient plasma. Chapter 1 summerizes the most dominant collisional forces — the ion drag force, neutral drag force, and thermophoresis — exerted on such a particle. In a uniform plasma (with some nonuniformity of the background neutral gas that causes the net collisional forces), the transport of an isolated dust particle is thus determined by those collisional forces as well as the electrostatic force and gravitational force exerted on it.

If the plasma is not uniform, an additional force needs to be taken into account. Since the Debye length is a function of the plasma density and temperature, a plasma nonuniformity

results in nonuniform Debye sheaths (sheath polarization). The electric field induced by such a polarized Debye sheath exerts a force on the particle at its center. This force — polarization force – is discussed in detail in Chap. 2. The magnitude of the polarization force is also estimated under typical glow discharge conditions. Since a particulate has a lower free energy when it has a thinner Debye sheath (i.e., smaller Debye length), the polarization force is always in the direction of decreasing Debye length regardless of the sign of the particulate charge. The magnitude of the polarization force is also estimated under typical glow discharge conditions.

A plasma flow can also cause sheath polarization. The effect of plasma flows on the polarization force is analyzed in Chap. 3. It is found that the magnitude of the plasma-flow induced polarization force is typically small for a small flow, being of the second order of the ratio of the ion flow velocity to ion thermal velocity. On the other hand, if the ion flow velocity is large compared to the ion thermal velocity, the ions are unable to form a sheath around the particulate and consequently the Debye sheath consists only of a deficiency of electrons (the ion sheath is "blown away" by the strong ion flow). In this case, although the polarization force due to the Debye-length gradients can still exist, one needs to use the electron Debye length λ_e, instead of the characteristic Debye length λ_D.

In Chaps 4 and 5, systems of the interacting charged particles in plasmas are discussed. Of particular interest is the thermodynamical properties and formation of Coulomb crystals (fluid-solid phase transition) of such systems. To simplify the problem, we assumed that the background plasma is in thermal equilibrium. Under this condition, the interparticle potential is given by the screened Coulomb potential (i.e., Yukawa potential). In the limit of infinite Debye lengths, such systems become the well-known classical one-component plasma (OCP).

The earlier studies of Yukawa systems are limited to the regime of strong screening, i.e., small Debye lengths. In the strong screening regime, the average number of particles with

which each particle interacts is small and therefore their MD and/or MC simulation are relatively easy and less time-consuming. In this study, however, we calculate the Ewald potentials of all interacting particles in our MD simulation and therefore the method is applicable to Yukawa systems of arbitrary Debye lengths, including the OCP limit. The MD simulation method used in this study thus fills the gap between the earlier extensive studies of the OCP system and strongly-screened Yukawa systems.

To obtain the thermodynamical properties — especially the phase diagram – of Yukawa systems, we have first formulated the method of evaluating the total free energy of particles confined in a cubical simulation box with periodic boundary conditions. The method we have employed is the extension of the method which has been extensively used for OCP systems. In the case of OCP, the background medium is completely uniform due to its infinite background temperature. In the case of Yukawa systems, however, one needs to take into account the free energy contribution from the nonuniformity of the background plasma, i.e., Debye sheaths. In Chap. 4, the free energy of Yukawa systems with periodic boundary conditions is derived and compared with that of OCP systems.

In an OCP system, each particle interacts with infinitely many particles through its *unscreened* Coulomb potential. However, the imposed periodic boundary conditions somewhat cancel the contributions from particles located far from the origin (i.e., the location of the particle that we are concerned with), so the effective interparticle potential among all OCP particles is finite (Ewald potential). For a Yukawa system with a finite Debye length, the average number of particles that each particle interact with is finite, but can be very large if the Debye length is sufficiently large. Since the number of simulation particles that can be realistically employed in MD simulation is limited by the computational efficiency, we also calculate the effective interparticle potential (Ewald potential) among all Yukawa particles for arbitrary Debye lengths. To this end, we have used a highly-accurate spline approximation to describe the energy contributions from particles outside the cubical simulation box

and far from the origin. In this way, we can increase the Debye length up to infinity without changing the number of simulation particles in our MD simulation.

We have described the methods and results of our MD simulation in Chap 5. We are especially interested in the regime of weak Debye screening (i.e., large Debye lengths), which connects the previously well-studied regimes of no screening (i.e., OCP: infinite Debye length) and strong screening (i.e., small Debye lengths). The regime of weak Debye screening is also relevant to experimental observations of strongly-coupled particulate systems in plasmas. Our simulation results for the no screening limit are in excellent agreement with those of the earlier OCP studies. It is found that the Γ value for the fluid-solid phase transition weakly increases as the screening parameter κ (which is inversely proportional to the Debye length) increases from 0 (the OCP value). Thus the Yukawa system does not exhibit a qualitative departure from the OCP system for small increase in the screening parameter κ.

We have also obtained the phase diagram for larger κ. Both the fluid-solid and bcc-fcc phase transitions of Yukawa systems are of first order. These results are also compared with those of the earlier studies of Yukawa systems. The overall agreement between the results of this study and those of the previous studies is good although there are some minor discrepancies among them in this regime. Since we have typically employed more simulation particles than those used in the earlier studies and have a better understanding of the size of uncertainties associated with the MD method, the results obtained in this study is likely to be more accurate than those previously published. Including the weak screening regime, we believe that the phase diagram of Yukawa systems presented in this work provides the most accurate and extensive version currently available.

Appendix A

The ion density distribution

In this appendix we further discuss why the Boltzmann ion distribution in Eq. (1.5) may be used even in regimes beyond its nominal physical validity. We also derive the appropriate "ion Debye length" from a more general ion distribution. To this end, it suffices to assume spherical symmetry around the particulate and a uniform plasma (i.e., Ψ_0, n_{i0}, and n_{e0} are constant), as in Chap. 1.

As the most general case, we assume that the ion density distribution is given by the form

$$n_i(r) = N_i(r, \varphi(r)),$$

where $r = |\mathbf{r}|$ is the radial distance from the particulate, located at $\mathbf{r} = 0$, and φ is the potential generated by the particulate. Since $\varphi \to 0$ as $r \to \infty$, for large r we may write

$$n_i \simeq \left.\frac{\partial N_i}{\partial \varphi}\right|_{r=\infty} \varphi,$$

which, together with the linearized electron Boltzmann distribution given by Eq. (1.6), leads to the linearized Possion's equation

$$\Delta\varphi^{(\mathrm{lin})}(r) = \frac{Q}{\varepsilon_0}\delta(\mathbf{r}) + \frac{1}{\lambda_D^2}\varphi^{(\mathrm{lin})}(r), \tag{A.1}$$

with

$$\frac{1}{\lambda_D^2} = -\frac{q}{\varepsilon_0}\left.\frac{\partial N_i}{\partial \varphi}\right|_{r=\infty} + \frac{e^2 n_{e0}}{k_B T_e} \tag{A.2}$$

Since the ion density should decrease monotonically to 0 as $r \to \infty$, we may assume $\partial N_i/\partial\varphi < 0$ (since $\varphi < 0$) and define the ion Debye length λ_i as

$$\frac{1}{\lambda_i^2} = -\frac{q}{\varepsilon_0}\left.\frac{\partial N_i}{\partial r}\right|_{r=\infty}.$$

Poisson's equation (A.1) gives the approximate solution $\varphi^{(\mathrm{lin})}$ for the profile of the potential φ appropriate to large r. As in the case of Eq. (1.7), the solution to Eq. (A.1) is given by the screened Coulomb potential

$$\varphi^{(\mathrm{lin})}(r) = \frac{Q\exp(-r/\lambda_D)}{4\pi\varepsilon_0 r}.$$

To obtain the solution for small r, we must solve the full Poisson equation

$$-\varepsilon_0\Delta\varphi(r) = -Q\delta(\mathbf{r}) + qn_i(r) - en_e(r). \tag{A.3}$$

Suppose the asymptotic form of the solution near $r = 0$ is given by $\varphi \sim r^\alpha$ ($\alpha < 0$). Noting that $n_e \to 0$ exponentially as $r \to 0$ and $\Delta = \partial^2/\partial r^2 + (2/r)\partial/\partial r$, Eq. (A.3) becomes, near $r = 0$,

$$\alpha(\alpha+1)r^{\alpha-2} \sim qn_i(r).$$

Thus, if $r^{2-\alpha}n_i(r) \to 0$ as $r \to 0$, the only possible singularity under these assumptions is $\alpha = -1$, i.e., $\varphi \sim 1/r$. This choice of α satisfies the condition $r^{2-\alpha}n_i(r) = r^3 n_i(r) \to 0$: the ion density should not increase any faster than $1/r^3$ near $r = 0$.

Therefore, the physical solution φ that we are concerned with — the magnitude of which increases monotonically as r decreases from ∞ to 0 — is given by $\varphi \simeq \varphi^{(\mathrm{lin})}$ for large r and $\varphi \sim 1/r$ for small r. For intermediate r, the monotonicity requirement is likely to determine the overall functional dependence of φ on r. Hence, it is natural to assume that the qualitative behavior of the full solution φ is described reasonably well by its linearized form $\varphi^{(\mathrm{lin})}$, and is relatively insensitive to the exact form of the ion density distribution $n_i(r)$.

It is interesting to also note that, as mentioned above, the ion density $n_i(r)$ should not increase any faster than $1/r^3$ around $r = 0$ in order for the solution $\varphi(r)$ to have a

"reasonable" singularity of the form r^α ($\alpha < 0$). This implies that the ion Boltzmann distribution given by Eq. (1.5) may be invalid near $r = 0$ not only physically but also mathematically, and should only be used in its linearized form (or, more precisely, including terms to order φ^2 in its Taylor expansion), as was done in Sec. 2.

By way of example, consider the collisionless ion density distribution given by Bernstein and Rabinowitz[1]:

$$n_i(r) = \frac{n_{i0}}{2}\left(\sqrt{1-\frac{q\varphi}{E_0}} \pm \sqrt{1-\frac{q\varphi}{E_0}-\frac{C}{r^2}}\right) \quad \text{for} \quad r \gtrless r_0\,, \tag{A.4}$$

where C is a constant proportional to the total ion flow to the particulate, and the positive and negative signs should be taken for $r > r_0$ and $r < r_0$, respectively. Here r_0 is defined as the self-consistent solution to the equations

$$1 - \frac{q\varphi(r_0)}{E_0} - \frac{C}{r_0^2} = 0\,,$$
$$r_0^3 \left.\frac{d\varphi}{dr}\right|_{r=r_0} = \frac{CE_0}{q}\,,$$

which must be solved simultaneously with Poisson's equation to determine φ. The ion distribution (A.4) represents the solution to the collisionless ion Vlasov equation, whose boundary condition is a mono-energetic ion distribution (of energy E_0) outside the sheath. This ion distribution may be regarded as another extreme of simplification — the opposite limit of the collisional case given by the ion Boltzmann distribution (1.5).

For large r, the ion density distribution (A.4) may be linearized as

$$n_i(r) \simeq n_{i0}\left(1 - \frac{q\varphi}{2E_0} - \frac{C}{2r^2}\right) \tag{A.5}$$

In the region where $C/2r^2 \ll q\varphi(r)/E_0 \ll 1$, therefore, we obtain Poisson's equation (A.1) with

$$\frac{1}{\lambda_D^2} = \frac{q^2 n_{i0}}{2E_0} + \frac{e^2 n_{e0}}{k_B T_e}\,, \tag{A.6}$$

and the ion Debye length may be defined as $\lambda_i = \sqrt{2E_0/q^2 n_{i0}}$. By setting $E_0 = \frac{1}{2}k_B T_i$, the characteristic Debye length λ_D becomes λ_0 used in Sec. 3. (Note that, as discussed in,[1] the asymptotic form of the potential φ for the ion distribution (A.4) at large r is given by $\varphi \sim 1/r^2$, rather than the screened Coulomb potential, since the term $C/2r^2$ in Eq. (A.5) may not be ignored for $r \to \infty$.) Recent numerical calculations[2-4] also indicate that the screened Coulomb potential with the Debye length (A.6) is an excellent approximation of the potential $\varphi(r)$ obtained from the ion distribution (A.4).

References

[1] I. Bernstein and I. Rabinowitz, Phys. Fluids **2**, 112 (1959).

[2] J. P. Boeuf, Phys. Rev. A**46**, 7910 (1992).

[3] J. E. Daugherty, R. K. Porteous, M. D. Kilgore, and D. B. Graves, J. Appl. Phys. **72**, 3934 (1992).

[4] S. J. Choi and M. J. Kushner, Appl. Phys. Lett. **62**, 2197 (1993).

Appendix B

Derivation of Eq. (2.22)

Here we elaborate on the derivation of the first-order potential $\varphi^{(1)}(\mathbf{r})$, given by Eq. (2.24), from Possion's equation (2.10) for a finite-size particle. A similar approach may be used to derive the corresponding expression, Eq. (2.12), for an infinitesimal particle. In order to make the method applicable to higher-order corrections (i.e., contributions from $\mathcal{O}(z^2)$ or higher-order terms in $\Psi_0(z)$ and $k_D(z)$), we shall generalize the method of derivation and discuss it in the context of a general harmonic expansion of the potential $\varphi(\mathbf{r})$.

Assuming the particle is located at the origin, we take polar coordinates about the z-axis. In dimensionless form, Eq. (2.10) may be written as

$$(\Delta_\xi - 1)\phi_1(\boldsymbol{\xi}) = \mu\phi_0(\xi)\xi\cos\theta\,, \tag{B.1}$$

where $\boldsymbol{\xi} = k_0\mathbf{r}$, $\xi = |\boldsymbol{\xi}|$, and μ is the parameter σ/k_0^3. The potentials are defined by $\phi_1(\boldsymbol{\xi}) = \varphi^{(1)}(\mathbf{r})$, $\phi_0(\xi) = \varphi^{(0)}(r)$ [see Eq. (2.21)], and Δ_ξ denotes the Laplacian in $\boldsymbol{\xi}$.

Suppose $\phi_1(\boldsymbol{\xi})$ has the form

$$\phi_1(\boldsymbol{\xi}) = g_l(\xi)P_l(\cos\theta)\,, \tag{B.2}$$

where $P_l(\zeta)$ is the l-th order Legendre polynomial in ζ. This form comes from the spherical harmonic expansion of the potential $\varphi(\mathbf{r})$. Writing

$$g_l(\xi) = w_l(\xi)\xi^{-\frac{1}{2}}\,,$$

the left-hand side of Eq. (B.1) becomes

$$\frac{1}{\xi^{3/2}}\left\{\frac{d}{d\xi}\left(\xi\frac{dw_l}{d\xi}\right)-\xi\left[1+\frac{(l+\frac{1}{2})^2}{\xi^2}\right]w_l\right\}P_l(\cos\theta)\,.$$

Since the right-hand side of Eq. (B.1) may be written as $\mu\phi_0(\xi)\xi P_1(\cos\theta)$, we choose $l=1$ for Eq. (B.2). Note that for higher-order calculations, where the left-hand side is proportional to a general $P_l(\cos\theta)$, the corresponding index l has to be chosen for Eq. (B.2).

To solve the resulting equation, we use the Green's function $G_\nu(x,y)$ for the modified Bessel's differential equation, defined by

$$\frac{d}{dx}\left(x\frac{dG_\nu}{dx}\right)-x\left(1+\frac{\nu^2}{x}\right)G_\nu=-\delta(x-y)\,,$$

where $x>0$. This Green's function can be easily constructed as

$$G_\nu(x,y)=\begin{cases}K_\nu(y)I_\nu(x) & \text{for } x<y\,,\\ K_\nu(x)I_\nu(y) & \text{for } x>y\,,\end{cases}$$

where K_ν and I_ν are the ν-th order modified Bessel functions. In our case, we choose $\nu=\frac{3}{2}$, i.e.,

$$K_{\frac{3}{2}}(z)=\sqrt{\frac{\pi}{2z}}\left(1+\frac{1}{z}\right)\exp(-z)\,,$$

$$I_{\frac{3}{2}}(z)=\sqrt{\frac{2}{\pi z}}\left(\cosh z-\frac{1}{z}\sinh z\right)\,.$$

Then a special solution $\phi_1^*(x)=g_1^*(\xi)\cos\theta$ to Eq. (B.1) may be obtained as

$$\begin{aligned}g_1^*(\xi)&=w_1(\xi)\xi^{-\frac{1}{2}}\\&=-\frac{\mu}{\sqrt{\xi}}\int_0^\infty\xi^{\frac{5}{2}}\phi_0(\xi)G_{\frac{3}{2}}(\xi,y)\,dy\\&=-\frac{1}{4}\mu C\exp(-\xi)\xi\,,\end{aligned}$$

where we set $\phi_0(\xi)=C\exp(-\xi)/\xi$ with $C=k_0aV_s\exp k_0a$. Using arbitrary constants C_1, C_2 and the special solution g_1^* above, we obtain the general solution to Eq. (B.1) as $\phi_1(x)=g_1(\xi)\cos\theta$, where

$$g_1(\xi)=C_1I_{\frac{3}{2}}(\xi)\xi^{-\frac{1}{2}}+C_2K_{\frac{3}{2}}\xi^{-\frac{1}{2}}+g_1^*(\xi)\,. \tag{B.3}$$

From the boundary condition (2.17), we have $g_1(\xi)\to 0$ as $\xi\to\infty$, which leads to $C_1=0$. Applying the boundary condition (2.18) to the mean field $\Psi_0(z)=\Psi_0(0)-E_0r\cos\theta$ and the perturbed field $\varphi(\mathbf{r})=\varphi^{(0)}(r)+g_1(k_0r)\cos\theta$, we obtain

$$-aE_0+g_1(k_0a)=0\,.$$

This boundary condition determines the constant C_2 and thus yields Eq. (2.24).

Appendix C

On Eqs. (3.27), (3.36) and (3.37)

In this appendix, we deive Eqs. (3.27), (3.36) and (3.37). If $u_0 \ll 1$, Eq. (3.25) may be written as

$$\tilde{\psi}^{(0)}(\mathbf{k}) = Q^{\bullet}\left[\frac{1}{k^2+1+\alpha} - \frac{\alpha u_0^2 \cos^2\theta}{(k^2+1+\alpha)^2}\right].$$

The first term represents the screened Coulomb potential (i.e., the first term of Eq. (3.27)), so we are now only concerned with the inverse Fourier transform of the second term, i.e.,

$$\delta\phi^{(0)}(\mathbf{r}) = \frac{-\alpha u_0^2 Q^{\bullet}}{q\beta_i(2\pi)^3}\int \frac{\cos^2\theta}{(k^2+c^2)^2}\exp(-i\mathbf{k}\cdot\mathbf{r}/\lambda_c)\,d\mathbf{k}\,, \tag{C.1}$$

where $c^2 = \alpha + 1$.

To perform the integration of Eq. (C.1), we choose the direction of the position vector $\mathbf{r}$ as the polar direction, rather than that of $\mathbf{v}_{i,0}$. Denoting the angle between $\mathbf{r}$ and $\mathbf{v}_{i,0}$ by Θ, and that between $\mathbf{r}$ and $\mathbf{k}$ by $\tilde{\theta}$, we may write

$$\cos\theta = \sin\Theta\sin\tilde{\theta}\cos\tilde{\phi} + \cos\Theta\cos\tilde{\theta}$$

$$\mathbf{k}\cdot\mathbf{r} = kr\cos\tilde{\theta}\,,$$

where the azimuthal angle $\tilde{\phi}$ of $\mathbf{k}$ around $\mathbf{r}$ is chosen appropriately.

After integrating over the angles $\tilde{\theta}$ and $\tilde{\phi}$, the following formulae may be used to perform the integration over k in Eq. (C.1):

$$\int_0^\infty \frac{x\sin ax}{(x^2+b^2)^2}\,dx = \frac{\pi a}{4b}\exp(-ab)\,, \tag{C.2}$$

$$\int_0^\infty \frac{\cos ax}{(x^2+b^2)^2}\,dx = \frac{\pi(1+ab)}{4b^3}\exp(-ab)\,,$$

$$\int_0^\infty \frac{\sin ax}{x(x^2+b^2)^2}\,dx = \frac{\pi}{2b^4}\left[1-\left(1+\frac{ab}{2}\right)\exp(-ab)\right],$$

where a, $b > 0$.

To obtain Eq. (3.36) by the inverse Fourier transform, one needs to evaluate the integrals

$$J_1 = \frac{1}{(2\pi)^3}\int \frac{k_z}{(k^2+c^2)^3}\exp(-i\mathbf{k}\cdot\boldsymbol{\rho})\,d\mathbf{k}\,,$$

$$J_2 = \frac{1}{(2\pi)^3}\int \frac{k_z}{k^2(k^2+c^2)^2}\exp(-i\mathbf{k}\cdot\boldsymbol{\rho})\,d\mathbf{k}\,,$$

where $k^2 = k_\perp^2 + k_z^2$ and $c^2 = \alpha + 1$ ($c > 0$). Unlike the calculation of Eq. (C.1) above, we here choose the z axis (i.e., the direction of the ion flow $\mathbf{v}_{i,0}$) as the polar direction.

To perform the intergration of J_1, we first write

$$g_1(k) = \frac{-1}{4(k^2+c^2)^2}.$$

Then, using spherical polar coordinates in $\mathbf{k}$ space, we have

$$\begin{aligned} J_1 &= \frac{1}{(2\pi)^3}\int \frac{dg_1(k)}{dk_z}\exp(-i\mathbf{k}\cdot\boldsymbol{\rho})\,d\mathbf{k} \\ &= \frac{i\zeta}{(2\pi)^3}\int g_1(k)\exp(-i\mathbf{k}\cdot\boldsymbol{\rho})\,d\mathbf{k} \\ &= -\frac{i\zeta}{8\pi^2\rho}\int_0^\infty \frac{k}{(k^2+c^2)^2}\sin k\rho\,dk \\ &= -\frac{i\zeta}{32\pi c}\exp(-c\rho)\,, \end{aligned}$$

where ζ is the z component of $\boldsymbol{\rho}$. Here we have used Eq. (C.2).

Similarly, to evaluate J_2, we use

$$g_2(k) = -\frac{1}{2c^4}\left(\log\frac{k^2+c^2}{k^2} - \frac{c^2}{k^2+c^2}\right),$$

where

$$\frac{dg_2(k)}{dk_z} = \frac{k_z}{(k^2+c^2)^3}$$

Then we have

$$
\begin{aligned}
J_2 &= \frac{1}{(2\pi)^3}\int \frac{dg_2(k)}{dk_z}\exp(-i\mathbf{k}\cdot\boldsymbol{\rho})\,d\mathbf{k} \\
&= \frac{i\zeta}{(2\pi)^3}\frac{4\pi}{\rho}\int_0^\infty g_2(k)k\sin k\rho\,dk \\
&= \frac{-i\zeta}{4\pi c^4\rho^3}\left[1-\exp(-c\rho)\left(1+c\rho+\frac{1}{2}c^2\rho^2\right)\right].
\end{aligned}
$$

Here we have used the formulae

$$
\int_0^\infty \frac{x\sin ax}{x^2+b^2}\,dx = \frac{\pi}{2}\exp(-ab), \tag{C.3}
$$

$$
\begin{aligned}
\int_0^\infty \log\left(\frac{x^2+a^2}{x^2+b^2}\right)x\sin xy\,dx = \frac{\pi}{y^2}&\left[\exp(-by)(1+by)\right. \\
&\left.-\exp(-ay)(1+ay)\right],
\end{aligned} \tag{C.4}
$$

where $a, b \geq 0$ and $y > 0$. Note that Eq. (C.2) may be obtained by differentiating Eq. (C.3) with respect to b. Similarly Eq. (C.4) may be derived by differentiating the following identity with respect to y:

$$
\int_0^\infty \log\left(\frac{x^2+a^2}{x^2+b^2}\right)\cos xy\,dx = \frac{\pi}{y}\left[\exp(-by)-\exp(-ay)\right], \tag{C.5}
$$

where again $a, b \geq 0$ and $y > 0$. In deriving Eq. (3.36) from J_1 and J_2, we have also used $c\rho = \kappa_D r$, $\kappa_e c = \kappa_D$, and $(\alpha\mu + \mu_e) = \sigma\lambda_e^3$.

To obtain Eq. (3.37) directly from Eq. (3.29), we evaluate the integrals

$$
\begin{aligned}
J_3 &= \frac{1}{(2\pi)^3}\int \frac{k_z^2}{(k^2+c^2)^3}d\mathbf{k}, \\
J_4 &= \frac{1}{(2\pi)^3}\int \frac{k_z^2}{k^2(k^2+c^2)^2}d\mathbf{k}.
\end{aligned}
$$

Again, using spherical polar coordinates in the k space and writing $\eta = k/c$, we may write

$$
J_3 = \frac{1}{6\pi^2 c}\int_0^\infty \frac{\eta^4}{(\eta^2+1)^3}\,d\eta,
$$

and

$$
J_4 = \frac{1}{6\pi^2 c}\int_0^\infty \frac{\eta^2}{(\eta^2+1)^2}\,d\eta
$$

Using the formula

$$
\int_0^\infty \frac{dx}{x^\alpha(1+x^\lambda)^\beta} = \frac{1}{\lambda}B\left(\beta-\frac{1-\alpha}{\lambda},\frac{1-\alpha}{\lambda}\right) \tag{C.6}
$$

$$
\text{if} \qquad \alpha < 1, \quad \lambda, \beta > 0, \quad \text{and} \quad \lambda\beta > 1-\alpha,
$$

we obtain $J_1 = 1/32\pi$ and $J_4 = 1/24\pi$. In Eq. (C.6), B is the beta function, related to the Gamma function Γ by

$$
B(p,q) = B(q,p) = \frac{\Gamma(p)\Gamma(q)}{\Gamma(p+q)}.
$$

Appendix D

Intermediate–scale Hamiltonian

In this Appendix, we show under what conditions the Hamiltonian (4.16) adequately describes the motion of charged mesoscopic particles immersed in a charge–neutralizing background. In such systems there are three distinct length scales: the microscopic scale, in which particulates and background charges are all regarded as individual particles; the intermediate scale, in which the particulates act as individual particles whereas the background species are statistically averaged and treated as a smooth field; and the macroscopic scale, in which all particles — the particulates and background species — may be statistically averaged.

The Hamiltonian relevant to the intermediate length scale may therefore be obtained from a statistical average over a more detailed microscopic Hamiltonian. In the averaging process, however, we assume that the background species are in contact with a large heat bath, so that the background temperatures (T_i and T_e in the plasma–dust system) remain uniform in space and constant in time. The microscopic Hamiltonian — i.e., the sum of the total kinetic energy and electrostatic potential energy for all the particles — is therefore not a constant of motion on the microscopic scale. The heat exchanged by the system and the heat bath during the particulate motion must be taken into account in the averaging process.

On the intermediate scale, therefore, the work done by the system to displace particulates through the electrostatic interactions is given by the change of its Helmholtz free energy F,

rather than its electrostatic potential energy. If the motions of heavy particulates and light background charges may be separated (i.e., the adiabatic approximation), then the change of the free energy is all used for the change of particulates' kinetic energies. Therefore the intermediate–scale Hamiltonian H for particulates may be written as the sum of the particulate kinetic energy and the Helmholtz free energy F, as Eq. (4.16), where $U_{ex} = F$. The Hamiltonian H is a constant of motion if the background temperatures, particle numbers and volume are held constant.

As in Sec. 4.2, we again consider a system of N identical negatively–charged dust grains of charge $-Q$ and mass m, and a neutralizing background of N_b charged particles. The background is assumed to consist of N_i ions of a single species with charge q and mass m_i, and N_e electrons with charge $-e$ and mass m_e ($N_i + N_e = N_b$), which are confined in volume V. The extension to systems with multiple ion species is straightforward.

On the microscopic scale, the state of the j–th particulate may be represented by a point $(\mathbf{p}_j, \mathbf{r}_j)$ $(1 \le j \le N)$ in phase space, where $\mathbf{p}_j$ and $\mathbf{r}_j$ denote its momentum and position. Likewise, the microscopic state of the j–th background particle of species α ($\alpha = i$ and e for ions and electrons), whose mass and charge are m_α and q_α ($q_i = q$ and $q_e = -e$) is defined by the phase–space point $(\mathbf{p}_j^{(\alpha)}, \mathbf{r}_j^{(\alpha)})$ $(1 \le j \le N_\alpha)$.

The N_α–particle joint–probability distribution function of the background species α may be written as

$$f_\alpha^{(N_\alpha)}(\mathbf{p}_\alpha^{N_b}, \mathbf{r}_\alpha^{N_b}; \mathbf{r}^N), \tag{D.1}$$

where $\mathbf{p}_\alpha^{N_\alpha}$ and $\mathbf{r}_\alpha^{N_\alpha}$ denote the sets of momenta and positions of all background particles, i.e., $\mathbf{p}_\alpha^{N_\alpha} = (\mathbf{p}_1^{(\alpha)}, \mathbf{p}_2^{(\alpha)}, \cdots, \mathbf{p}_{N_b}^{(\alpha)})$, etc. In writing Eq. (D.1), we have assumed that motions of dust grains are sufficiently slow compared to the motion of background species, and therefore the probability function $f_\alpha^{(N_\alpha)}$ explicitly depends on the instantaneous dust–grain positions $\mathbf{r}^N$, but not their momenta $\mathbf{p}^N$. Note that the N_b–particle joint–probability distribution function

for all the background particles $f^{(N_b)}(\mathbf{X}_i^{N_i}, \mathbf{X}_e^{N_e}; \mathbf{r}^N)$ is related to $f_\alpha^{(N_\alpha)}$ as, e.g.,

$$f_i^{(N_i)}(\mathbf{X}_i^{N_i}; \mathbf{r}^N) = \int \cdots \int f^{(N_b)}(\mathbf{X}_i^{N_i}, \mathbf{X}_e^{N_e}; \mathbf{r}^N) d\mathbf{X}_e^{N_e},$$

where we have used the abbreviated notations $\mathbf{X}^N = (\mathbf{p}^N, \mathbf{r}^N)$ and $\mathbf{X}_\alpha^{(N_\alpha)} = (\mathbf{p}_\alpha^{N_\alpha}, \mathbf{r}_\alpha^{N_\alpha})$.

The 2-ion joint-probability distribution function is also defined in the usual manner by

$$f^{(i,i)}(\mathbf{X}_1^{(i)}, \mathbf{X}_2^{(i)}; \mathbf{r}^N) = \int \cdots \int f_i^{(N_i)}(\mathbf{X}_i^{N_i}; \mathbf{r}^N) d\mathbf{X}_3^{(i)} d\mathbf{X}_4^{(i)} \cdots d\mathbf{X}_{N_i}^{(i)}$$

Here $\mathbf{X}_j^{(i)} = (\mathbf{p}_j^{(i)}, \mathbf{r}_j^{(i)})$. The ion-electron and 2-electron joint-probability distribution functions $f^{(i,e)}$ and $f^{(e,e)}$ are defined similarly.

On the microscopic scale, the Hamiltonian for the background ions and electrons is given by

$$H_{\text{micro}} = \sum_\alpha \sum_{j=1}^{N_\alpha} \frac{|\mathbf{p}_j^{(\alpha)}|^2}{2m_j} + U_{\text{micro}},$$

where $\sum_\alpha$ denotes the sum over all the species α (i.e., $\alpha = i$ and e) and U_{micro} is the potential energy

$$\begin{aligned} U_{\text{micro}} = & \frac{1}{2} \int_V \rho_{\text{micro}}(\mathbf{r}) \Psi_{\text{micro}}(\mathbf{r}) \, d\mathbf{r} \\ & - \frac{Q^2}{8\pi\varepsilon_0} \sum_{j=1}^{N} \int_V \frac{\delta(\mathbf{r} - \mathbf{r}_j)}{|\mathbf{r} - \mathbf{r}_j|} d\mathbf{r} - \frac{1}{8\pi\varepsilon_0} \sum_\alpha \sum_{j=1}^{N_\alpha} \int_V \frac{q_\alpha^2 \delta(\mathbf{r} - \mathbf{r}_j^{(\alpha)})}{|\mathbf{r} - \mathbf{r}_j^{(\alpha)}|} d\mathbf{r}. \end{aligned} \tag{D.2}$$

Here

$$\rho_{\text{micro}}(\mathbf{r}) = -Q \sum_{j=1}^{N} \delta(\mathbf{r} - \mathbf{r}_j) + \sum_\alpha \sum_{j=1}^{N_\alpha} q_\alpha \delta(\mathbf{r} - \mathbf{r}_j^{(\alpha)})$$

and

$$\Psi_{\text{micro}}(\mathbf{r}) = \frac{1}{4\pi\varepsilon_0} \int_V \frac{\rho_{\text{micro}}(\mathbf{r}')}{|\mathbf{r} - \mathbf{r}'|} d\mathbf{r}'$$

denote the charge distribution and its electrostatic potential. The last two terms on the right-hand side of Eq. (D.2) subtract the infinite self-energies of particulates and background charges, which are formally included in the first term.

The statistical average $\langle \cdot \rangle$ of the Hamiltonian H_{micro} over the probability distribution function yields the the internal energy of the background plasma:

$$\langle H_{\text{micro}} \rangle = \int \cdots \int H_{\text{micro}}(\mathbf{X}^{N_b}; \mathbf{r}^N) f^{(N_b)}(\mathbf{X}^{N_b}; \mathbf{r}^N) \, d\mathbf{X}^{N_b}. \tag{D.3}$$

If the correlation between ions and electrons is assumed negligible, we have $f^{(N_b)} = f_i^{(N_i)} f_e^{(N_e)}$. The Helmholtz free energy is then given by

$$F = \langle H_{\text{micro}} \rangle + \sum_\alpha T_\alpha S_\alpha^{\text{bg}}, \tag{D.4}$$

where

$$S_\alpha^{\text{bg}} = -k_B \langle \ln f_\alpha^{(N_\alpha)}(\mathbf{X}_\alpha^{N_\alpha}; \mathbf{r}^N) \rangle$$

denotes the entropy of the background species α.

We now further assume that (i) each of the background species is in local thermal equilibrium, and (ii) pair correlations of the background species are negligible. Then the 2-particle joint probability function $f^{(\alpha,\alpha)}$ becomes

$$f^{(\alpha,\alpha)}(\mathbf{X}_1^{(\alpha)}, \mathbf{X}_2^{(\alpha)}; \mathbf{r}^N) = \frac{n_\alpha(\mathbf{r}_1) n_\alpha(\mathbf{r}_2)}{N_\alpha(N_\alpha - 1)} \left[\frac{\beta_\alpha}{2m_\alpha \pi} \right]^{\frac{3}{2}} \exp\left(-\frac{\beta_\alpha}{2m_\alpha} p^2 \right), \tag{D.5}$$

where $n_\alpha(\mathbf{r})$ denotes the density of background species α at position $\mathbf{r}$ and $\beta_\alpha = 1/k_B T_\alpha$, as before. Here the dependence of $n_\alpha(\mathbf{r})$ on the particulate positions $\mathbf{r}^N$ is suppressed for brevity.

Carrying out the integral (D.3) using Eq. (D.5), we obtain the expressions for the internal energy as

$$\langle H_{\text{micro}} \rangle = \sum_\alpha K_\alpha + \frac{1}{2} \int_V \rho(\mathbf{r}) \Psi(\mathbf{r}) \, d\mathbf{r} - \frac{Q^2}{8\pi\varepsilon_0} \sum_{j=1}^{N} \int_V \frac{\delta(\mathbf{r} - \mathbf{r}_j)}{|\mathbf{r} - \mathbf{r}_j|} d\mathbf{r}, \tag{D.6}$$

where

$$\rho(\mathbf{r}) = -Q \sum_{j=1}^{N} \delta(\mathbf{r} - \mathbf{r}_j) + q n_i(\mathbf{r}) - e n_e(\mathbf{r}), \tag{D.7}$$

$$\Psi(\mathbf{r}) = \frac{1}{4\pi\varepsilon_0} \int_V \frac{\rho(\mathbf{r}')}{|\mathbf{r} - \mathbf{r}'|} d\mathbf{r}'. \tag{D.8}$$

and the entropy of the background species α is given by

$$S_\alpha^{\rm bg} = -\frac{1}{T_\alpha} K_\alpha - k_B \int_V n_\alpha(\mathbf{r})[\ln n_\alpha(\mathbf{r})\Lambda_{T\alpha} - 1]\, d\mathbf{r}\,. \tag{D.9}$$

In the equations above, $K_\alpha = \frac{3}{2} N_\alpha k_B T_\alpha$ denotes the kinetic energy for the species α.

From Eqs. (D.4), (D.6)–(D.9), we obtain Eq. (4.17). (Recall that the free energy F is denoted by U_{ex} in the main text.) Thus the intermediate-scale Hamiltonian H is given by Eq. (4.16) with Eq. (4.23) if correlations among background charges are negligible. Note that the entropy of the background plasma is approximated by the local entropy (the Thomas–Fermi approximation), as shown in the second term of Eq. (D.9).

Appendix E

The OCP limit of the ideal–gas free energy

In this appendix, we show that the ideal–gas contribution to the free energy $F_{\rm id}^{\rm bg}$ of Eq. (4.22) vanishes in the limit $k_D \to 0$. As is readily seen from Eqs. (4.10) and (4.15), $\delta\rho^{\rm bg} \to 0$ and $\Psi(\mathbf{r}) \to \infty$ in this limit. Therefore it is not immediately evident from Eq. (4.22) that $F_{\rm id}^{\rm bg} \to 0$ in the OCP limit.

It is straightforward to rewrite Eq. (4.22) as

$$F_{\rm id}^{\rm bg} = \frac{1}{2}\sum_{i\neq j}\sum \psi_3(\mathbf{r}_i - \mathbf{r}_j) + \frac{1}{2} N \lim_{|\mathbf{R}|\to 0} \psi_3(\mathbf{R}) \tag{E.1}$$

Here the pair potential $\psi_3(\mathbf{R})$ is given by

$$\psi_3(\mathbf{R}) = \frac{Q^2}{4\pi\varepsilon_0}\int_{V_\infty} w_2(\boldsymbol{\rho})\frac{\exp(-k_D|\boldsymbol{\rho}-\mathbf{R}|}{|\boldsymbol{\rho}-\mathbf{R}|}\, d\boldsymbol{\rho}\,, \tag{E.2}$$

with

$$w_2(\boldsymbol{\rho}) = \frac{k_D^2}{4\pi}\sum_{\mathbf{n}} \frac{exp(-k_D|\boldsymbol{\rho}-\mathbf{n}L|)}{|\boldsymbol{\rho}-\mathbf{n}L|} - \frac{1}{L^3}$$

To evaluate $\psi_3(\mathbf{R})$, we again appeal to Parseval's identity. The Fourier transform of $w_2(\boldsymbol{\rho})$ may be calculated in a manner similar to that used to obtain Eq. (4.37):

$$\begin{aligned}\tilde{w}_2(\mathbf{k}) &= \frac{1}{L^3}\left[\frac{k_D^2}{k_D^2 + 4\pi k^2}\sum_{\mathbf{n}} \delta\left(\mathbf{k} - \frac{\mathbf{n}}{L}\right) - \delta(\mathbf{k})\right] \\ &= \frac{k_D^2}{L^3(k_D^2 + 4\pi^2 k^2)}\sum_{\mathbf{n}\neq 0} \delta\left(\mathbf{k} - \frac{\mathbf{n}}{L}\right)\end{aligned} \tag{E.3}$$

Similarly the Fourier transform of

$$\frac{\exp(-k_D|\mathbf{r}-\mathbf{a}|)}{|\mathbf{r}-\mathbf{a}|}$$

is given by

$$\frac{4\pi\exp(2\pi i\mathbf{k}\cdot\mathbf{r})}{4\pi^2k^2+k_D^2}. \tag{E.4}$$

Using Eqs. (E.3) and (E.4), we obtain

$$\begin{aligned}\psi_3(\mathbf{R}) &= \frac{Q^2}{4\pi\varepsilon_0}\frac{1}{L^3}\int\sum_{\mathbf{n}\neq 0}\delta\left(\mathbf{k}-\frac{\mathbf{n}}{L}\right)\exp(2\pi i\mathbf{k}\cdot\mathbf{R})\frac{4\pi k_D^2}{(k_D^2+4\pi k^2)^2}\,d\mathbf{k}\\ &= \frac{Q^2}{4\pi\varepsilon_0}\frac{4\pi k_D^2}{L^3}\sum_{\mathbf{n}\neq 0}\frac{\exp(2\pi i\mathbf{n}\cdot\mathbf{R}/L)}{(k_D^2+4\pi^2|\mathbf{n}|^2/L^2)^2}.\end{aligned} \tag{E.5}$$

From the following inequality, it is easy to see that the sum in Eq. (E.5) converges even in the case $k_D = 0$:

$$\sum_{\mathbf{n}\neq 0}\left|\frac{\exp(2\pi i\mathbf{n}\cdot\mathbf{R}/L)}{(k_D^2+4\pi^2|\mathbf{n}|^2/L^2)^2}\right| \leq \frac{L^4}{16\pi^4}\sum_{\mathbf{n}\neq 0}\frac{1}{|\mathbf{n}|^4},$$

where the sum $\sum_{\mathbf{n}\neq 0}|\mathbf{n}|^{-4}$ is clearly convergent. Therefore, we have

$$\lim_{k_D\to 0}\psi_3(\mathbf{R}) = 0. \tag{E.6}$$

From Eqs. (E.1) and (E.6), we thus readily obtain

$$F_{\rm id}^{\rm bg}\to 0 \quad \text{as} \quad k_D\to 0.$$

We now evaluate $\langle H_{\rm micro}\rangle$ by subtracting $F_{\rm id}^{\rm bg}$ from the excess energy of the Yukawa system $U_{\rm ex}$ given by Eq. 4.24. First we derive a different expression of $F_{\rm id}^{\rm bg}$ from Eq. (E.1). Using the identity

$$\int_{V_\infty}\frac{\exp(-k_D|\mathbf{r}-\mathbf{a}|-k_D|\mathbf{r}-\mathbf{b}|)}{|\mathbf{r}-\mathbf{a}||\mathbf{r}-\mathbf{b}|}\,d\mathbf{r} = \frac{2\pi}{k_D}\exp(-k_D|\mathbf{a}-\mathbf{b}|),$$

we perform the integration of Eq. (E.2) to obtain $\psi_3(\mathbf{r})$ as

$$\psi_3(\mathbf{R}) = \frac{Q^2k_D}{8\pi\varepsilon_0}\sum_{\mathbf{n}}\exp(-k_D|\mathbf{R}-\mathbf{n}L|) - \frac{Q^2}{\varepsilon_0k_D^2L^3}.$$

It then follows from Eq. (E.1) that

$$\begin{aligned}F_{\rm id}^{\rm bg} &= \frac{Q^2k_D}{16\pi\varepsilon_0}\sum_{i\neq j}\sum\sum_{\mathbf{n}}\exp(-k_D|\mathbf{R})_{ij}-\mathbf{n}L|)\\ &\quad -\frac{NQ^2n}{2\varepsilon_0k_D^2}+\frac{NQ^2k_D}{8\pi\varepsilon_0}\sum_{\mathbf{n}}\exp(-k_D|\mathbf{n}|L),\end{aligned}$$

where $\mathbf{R}_{ij} = \mathbf{r}_i - \mathbf{r}_j$. Since $\langle H_{\rm micro}\rangle = U_{\rm ex} - F_{\rm id}^{\rm bg}$, the "pair-potential" form of the internal energy $\langle H_{\rm micro}\rangle$ becomes

$$\begin{aligned}\langle H_{\rm micro}\rangle &= \frac{1}{2}\sum_{i\neq j}\sum\left(\frac{1}{|\mathbf{R}_{ij}-\mathbf{n}L|}-\frac{k_D}{2}\right)\exp(-k_D|\mathbf{n}|L)\\ &\quad -\frac{3NQ^2k_D}{16\pi\varepsilon_0}+\frac{Q^2N}{8\pi\varepsilon_0}\sum_{\mathbf{n}\neq 0}\left(\frac{1}{|\mathbf{n}|L}-\frac{k_D}{2}\right)\exp(-k_DL|\mathbf{n}|).\end{aligned} \tag{E.7}$$